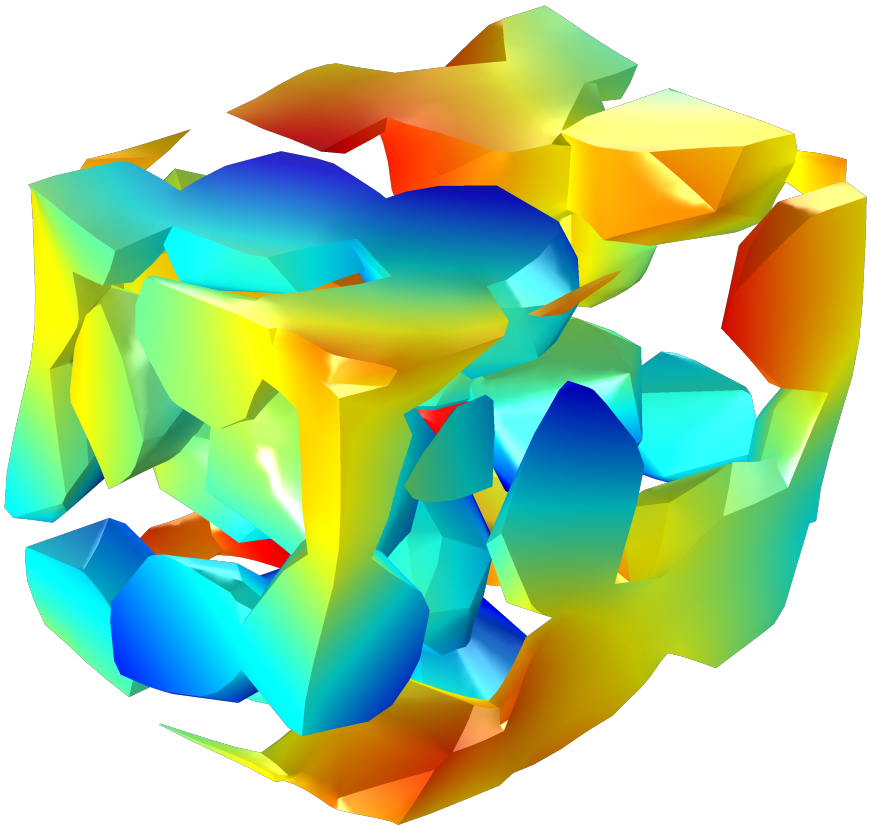

Generation and Finite Element Analysis of Synthetic Microstructures for Structural Battery Electrolytes

Master's thesis in Applied Mechanics

PER BOEKHOUT
DANIEL FREDRIKSSON

Department of Industrial and Materials Science
CHALMERS UNIVERSITY OF TECHNOLOGY
Gothenburg, Sweden 2020

Master's thesis 2020:NN

Generation and Finite Element Analysis of Synthetic Microstructures for Structural Battery Electrolytes

PER BOEKHOUT
DANIEL FREDRIKSSON

CHALMERS
UNIVERSITY OF TECHNOLOGY

Department of Industrial and Materials Science
Division of Material and Computational Mechanics
Chalmers University of Technology
Gothenburg, Sweden 2020

Generation and Finite Element Analysis of Synthetic Microstructures for Structural Battery Electrolytes

Per Boekhout
Daniel Fredriksson

Supervisor: Associate Professor Ralf Jänicke, Industrial and Materials Science
Examiner: Associate Professor Ralf Jänicke, Industrial and Materials Science

Master's Thesis 2020
Department of Industrial and Materials Science
Division of Material and Computational Mechanics
Chalmers University of Technology
SE-412 96 Gothenburg
Telephone +46 31 772 1000

Cover: Deformed synthetic microstructure for driving macroscopic strain $\bar{\epsilon}_{11} = 1$ plotted for fluctuation field u^{μ}.

Typeset in LaTeX
Printed by Chalmers Reproservice
Gothenburg, Sweden 2020

Generation and Finite Element Analysis of Synthetic Microstructures for Structural Battery Electrolytes
PER BOEKHOUT
DANIEL FREDRIKSSON

Department of Industrial and Materials Science
Chalmers University of Technology

Abstract

The structural battery composite is a new multifunctional material that combines the mechanical features of a carbon fiber composite with the energy storing capabilities of a lithium-ion battery by exploiting the electrochemical properties of the carbon fiber. Further development of this technology can lead to significant improvement of efficiency in a variety of applications, with vehicular applications being the most immediate and promising.

The aim of the project is to model the porous electrolyte polymer matrix inside the structural battery composite by generating synthetic microstructure, serving as statistical volume elements, and applying first order homogenization. The evaluation is made by solving boundary problems for the generated structures with the finite element method where strong periodic boundary conditions are used for the modeling. Using this numerical evaluation as a basis, the effective diffusive and elastic properties are estimated for the generated microstructures such that the overall performance of the battery is derived.

Four types of fully periodic synthetic electrolyte microstructures are presented. The Cahn-Hilliard structure based on solving the Cahn-Hilliard phase separation equation. A dense sphere packing structure made from a swelled distribution of spheres generated with the Lubachevsky-Stillinger algorithm. The Voronoi structure where a damage phase field is solved with essential boundary conditions on the cell edges of a Voronoi tessellation. A novel convex hull structure created through a Voronoi tessellation around a sparse sphere packing where random points are generated within the cells to create convex hull particles, with particle connectivity enforced through a connectivity algorithm. A modification to the convex hull microstructure allows the implementation of a three-phase structure where some of the connections were redefined as binder material as an attempt to create a synthetic positive structural battery electrode microstructure. Furthermore, the passivation layer that forms along the negative fiber electrode is also modeled and evaluated in terms of delamination.

Comparison with previous research into synthetic electrolyte microstructures finds a good match between the presented results and those from previous work, which validates the methodology of both studies. Furthermore the convex hull microstructure manages to emulate the effective properties of certain experimental values better than microstructures in previous research. Overall both the effective stiffness and diffusivity were found to correlate linearly with the porosity, but the different topologies had a clear effect on the performance. Investigating the mechanical performance of the electrode structure found that the stiffness of the binder material has a significant impact on the effective stiffness of the electrode, but the volume fraction of the binder within the domain did not seem to have any effect on the stiffness. A toolbox is developed for modeling the interface between the polymer matrix and the passivation layer in 2D, and a study with arbitrarily material parameters is conducted. From this study it is shown that the passivation layer may have major influence on the mechanical properties of the generated microstructure if the porosity is high and that the delamination is highly dependent on assigned material parameters.

The final result is a fully automated process where statistical volume elements are generated for a type of microstructure and analyzed through computational homogenization. The automation is achieved through interfacing external open-source software packages and the commercial finite element software `COMSOL` with `MATLAB`.

Keywords: Synthetic microstructures, computational homogenization, structural battery electrolyte, structural battery electrode, passivation layer, convex hull, Cahn-Hilliard, Voronoi tessellation, Lubachevsky-Stillinger

Acknowledgements

First and foremost we want to thank our examiner and supervisor and Ralf Jänicke for outstanding support and encouragement throughout our master's thesis project. We would also like to thank Peter Gudmundson and Johanna Xu for showing interest in the results of our work during the project. Our appreciation also goes out to Vinh Tu for his precursory work and providing advice with the structure generation.

Per Boekhout & Daniel Fredriksson, Gothenburg, June 2020

Contents

1 Introduction

The structural battery composite is an new type of multifunctional material that combines the load bearing capacity of a carbon fiber composite and the ability to store electrical energy of a battery [1]. By exploiting the electrochemical properties of carbon as a negative lithium-ion electrode, the composite can be used as a lithium battery [2]. The possibility for a structural component to carry mechanical loads while simultaneously storing energy has many potential applications. Its uses in vehicle systems, particularly in the automotive and aerospace industries, are very promising [3]. In particular, the most immediate benefit of applying such a technology is a significant improvement in efficiency as a result of weight reductions from the multifunctional structural battery composite contributing to both mechanical and electrical design parameters. As more research and development is done on this technology, it paves the way for an essentially "mass-less" energy system. Ultimately, structural batteries could provide numerous industrial, societal, and environmental benefits.

1.1 Structural battery composite design

Two types of designs have been proposed for the structural battery composite, a laminated battery and a 3D battery [4]. The laminated battery consists of half cell composite lamina that fulfill separate functions. The negative electrode lamina consists of carbon fiber reinforced polymer, where the polymer matrix is a Li-ion conductive electrolyte, and the carbon fibers function as negative electrodes. The positive electrode lamina differs from the negative in that the carbon fibers are coated with a lithium-metal-oxide which functions as the positive electrode. Between the laminae a separator layer is placed to prevent short circuiting. Each pair of lamina are connected to a set of current collectors. Initial concepts for the laminated battery used a solid polymer matrix electrolyte, but due to poor ionic mobility the porous structural battery electrolyte (SBE) was proposed instead [5]. The porous SBE is a bicontinuous porous polymer matrix filled with a liquid electrolyte, meaning that both the solid phase and pore/liquid phase are continuous. In the 3D battery each individual composite lamina is a functional battery cell. The carbon fibers are coated with a polymer coating that function as both a solid electrolyte and a separator layer. The composite matrix is a lithium-metal-oxide doped polymer that serves as the positive electrode.

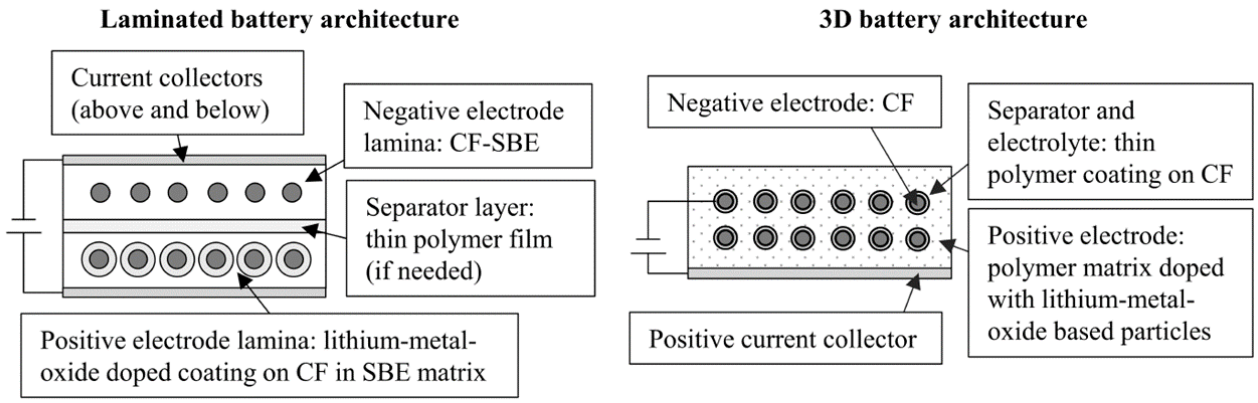

Figure 1.1: Schematic illustration of the two designs. Image reproduced with the permission of David Carlstedt [4].

The laminated design is currently the most developed concept. It is this design that this project will concern itself with. Specifically, the focus will be on the porous polymer electrolyte as this is a crucial component that affects the structural integrity of the battery as well as its performance as a battery.

1.2 The need for synthetic microstructures

Classical applications of solid mechanics theory model physical systems on a macroscopic dimensional scale, which is non-formally defined as the length scale which is perceivable by the naked human eye. However, the heterogeneities of a material at the microscale will have a major influence on the material's macroscopic

behavior. A spatial discretization which captures the microscale for a macroscale problem would have unfeasible computational costs. To capture the effects of the microstructure in an efficient manner, the theory of multiscale modeling has been developed [6]. While there are technologies available to reconstruct X-ray [7] or FIB/SEM [8] scans these typically contain very fine details that can be expensive or unfeasible to solve numerically. For this reason the capability of generating synthetic microstructures as a substitute is very appealing. With such synthetic microstructures available, one can evaluate the macroscopic properties of a material through virtual material testing, and in the context of non-linear problems, solve for the microscale effects in a nested solution scheme.

1.3 Project specification

The focus in this project will be on implementing different types of techniques for generating microstructures. A sufficiently large sample of realizations for each type of structure will be generated for suitable porosities. The effective macroscopic properties relating to mechanical and electrochemical performance of each realization will be computed using computational homogenization with the finite element method. The simulation software `COMSOL Multiphysics` will be used to solve the finite element problem. Because the intent is to study the microstructures on a statistical level, which will require a large number of samples, it is considered a requirement for the workflow to be fully automated. For that purpose, the microstructure generation, the finite element analysis (FEA), and the interface between these must be must be automated. To enable this, the `MATLAB` application programming interface (API) for `COMSOL`, called the `LiveLink` module, will be used. An additional study will also be conducted to investigate the effective mechanical properties of a synthetic electrode microstructure. Furthermore, this project will simulate the damage evolution along the interface of the passivation layer which is formed at the surface of the carbon fiber.

1.4 Delimitations

Delimitations for the projected are presented. Mainly, these are related to the microstructure generation and numerical evaluation.

- The study in this project will not account for any fluid-structure interaction within the electrolyte. It is recognized that the mechanical performance of the SBE would be influenced by the liquid in the pores. In the mechanical simulations the pores will be treated as voids.

- The solid and liquid phases are both assumed to have isotropic material properties at the microscale. Linear elasticity will be used to model the mechanical response. The electrochemical performance of the microstructure will be modeled using stationary Fickian diffusion. No coupling will be implemented between the mechanical and electrical problems.

- No physical experiments will be conducted. The only form of verification of results will be a comparison to previous research on the topic of microstructure generation in the context of SBE.

- Ideally the microstructures will be generated in such a way that they contain enough heterogeneities that the effective properties for each realization have minimal variation from one another. This trait would indicate that the structures are representative. This cannot necessarily be guaranteed, and is not considered a requirement.

- No parametric study is to be carried out. Each microstructure generation technique will posses a variety of generation parameters whose influence on the effective properties is difficult to anticipate without a rigorous parametric study. Such a study is not included in this project due to time constraints. The generation parameters will be chosen based on generation speed and meshing simplicity.

2 Numerical modeling

The need for effective material models that captures material behavior at different scales has led to rise of multiscale modeling which allows for the bridging between models at different scales [9]. Computational homogenization is an efficient method to facilitate multiscale modeling where integration methods are used over short length scales to estimate material behavior at the macroscale. In this thesis computational homogenization is used to estimate the macroscopic diffusive and mechanical properties of generated microstructures. As a basis for computing the effective material properties, FEA is employed to solve boundary value problems of generated finite sized microstructures while employing microscopic linear material models. Then, by the use of homogenization the effective material properties are estimated for the generated structures.

2.1 The statistical volume element (SVE)

Often the properties of a particle at the subscale are isotropic; however, depending on the morphology the macroscopic properties may very well be anisotropic. A way of estimating the effect of the heterogeneous properties on the macroscale is via homogenization, or more concretely, upon volume averaging the properties of a representative volume element (RVE) [10]. An RVE can be defined as a volume element occupying a sufficiently large part of a domain such that it yields representative properties of the whole structure. Although the use of an RVE is a powerful tool for constitutive modeling, it fails to capture the intrinsic variations of the material [11]. A different approach is to use a statistical volume element (SVE), a partition of the RVE, that statistically takes into account the local variability of the material. In contrary to the RVE which assumes the same averaged value for all realizations, the SVE allows for statistical scatter for different realizations.

In this project multiple microstructures are generated to determine macroscopic material behavior while allowing for a spread in the computed effective parameters, meaning that the SVE approach is used for constitutive modeling. An SVE can take on any arbitrary shape but is for simplicity implemented as cubic unit cells. Figure 2.1 illustrates a cubic SVE with domain $\Omega_\square$, boundary $\Gamma_\square$, boundary normals $\boldsymbol{n}$, and side length $L_\square$.

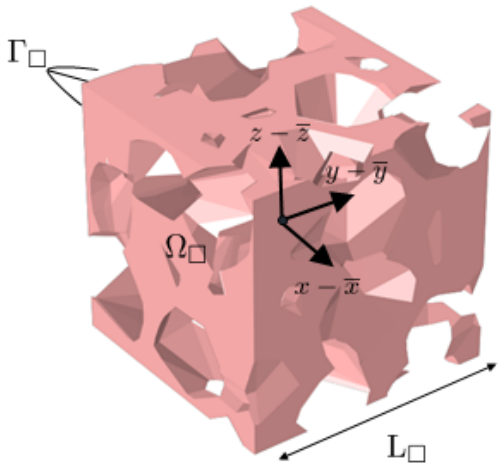

Figure 2.1: Illustration of the solid phase occupying the cubic SVE.

2.2 First order homogenization

In order to establish properties of the SVE, a first order homogenization process is used. This is an effective approach for upscaling from micro to macro when the material exhibits stable behavior. The first step in the procedure is downscaling the macrostructure such that any field variable is transferred to the microscale by applying sufficient boundary conditions. Then, the microscale problem is solved through numerical modeling and subsequently upscaled via volume averaging. Here, FEA is used to solve the microscale problem and to handle the upscaling. Since the upscaling is made by volume averaging the subscale variables, the volume average

operator is introduced:

$$\langle \bullet \rangle_{\square} \triangleq \frac{1}{|\Omega_{\square}|} \int_{\Omega_{\square}} \bullet \, \mathrm{d}\Omega. \tag{2.1}$$

In classic homogenization it is assumed that a microscopic variable $\bullet$ can additively be split into a finescale fluctuation contribution $\bullet^{\mu}$ and a macroscale linear contribution $\bullet^{\mathrm{M}}$ according to:

$$\bullet\,(\boldsymbol{x}) = \bullet^{\mathrm{M}}(\boldsymbol{x}) + \bullet^{\mu}(\boldsymbol{x}) \quad \boldsymbol{x} \in \Omega_{\square}, \tag{2.2}$$

which can be used to specify proper boundary conditions for the SVE. A schematic that illustrates the process of homogenization is shown for the linear elastic problem in Figure 2.2, where Ω defines the macroscale domain and $\Omega_{\square}$ the SVE domain.

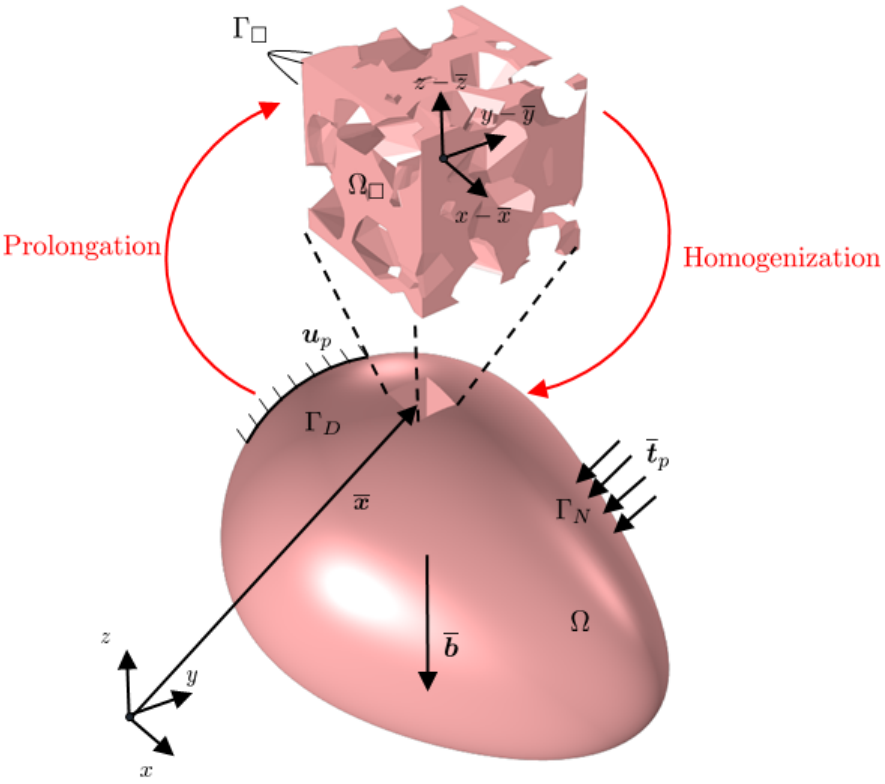

Figure 2.2: Illustration of upscaling via homogenization.

2.3 Strong and weak formats

Based on the preliminaries of first order computational homogenization, the microscopic models of linear elasticity and diffusion are introduced for the SVE. More specifically, weak formats for the elasticity problem and diffusion problem are derived with their related constitutive models.

2.3.1 Linear elasticity at the microscale

In order to establish the weak format of microscopic linear elasticity, the strong format of subscale linear elasticity is formulated. The strong elastic format is defined by the quasi-static balance of linear momentum [12] together with essential and natural boundary conditions for the SVE in Figure 2.1:

$$\begin{aligned} -\boldsymbol{\sigma} \cdot \boldsymbol{\nabla} &= \boldsymbol{b} \quad \text{in} \quad \Omega_{\square}, \\ \boldsymbol{u} &= \boldsymbol{u}_p \quad \text{on} \quad \Gamma_{\square,D}, \\ \boldsymbol{t} \triangleq \boldsymbol{\sigma} \cdot \boldsymbol{n} &= \boldsymbol{t}_p \quad \text{on} \quad \Gamma_{\square,N}, \end{aligned} \tag{2.3}$$

where $\boldsymbol{\sigma}$ denotes the Cauchy stress tensor, $\boldsymbol{b}$ the body force, $\boldsymbol{u}$ the prescribed displacement on the essential boundaries, and $\boldsymbol{t}$ the traction acting along the natural boundaries. Moreover, the constitutive relations for Hooke's linear law of elasticity are introduced:

$$\begin{aligned} \boldsymbol{\sigma} &= \boldsymbol{E} : \boldsymbol{\epsilon}, \\ \boldsymbol{\epsilon} &= \boldsymbol{\epsilon}[\boldsymbol{u}] \triangleq (\boldsymbol{u} \otimes \boldsymbol{\nabla})^{\mathrm{sym}}, \end{aligned} \tag{2.4}$$

where $\boldsymbol{u}$ indicates the displacement of a point $\boldsymbol{x} \in \Omega_{\square}$, $\boldsymbol{\epsilon}$ the strain tensor, and $\boldsymbol{E}$ the stiffness tensor given by Hooke's model of isotropic linear elasticity in terms of the shear modulus G and bulk modulus K:

$$\boldsymbol{E} = 2G\boldsymbol{I}_{\mathrm{dev}}^{\mathrm{sym}} + K\boldsymbol{I} \otimes \boldsymbol{I}, \tag{2.5}$$

where the different identity tensors $\boldsymbol{I}$ and the operator $\underline{\otimes}$ are defined accordingly:

$$\begin{aligned} \boldsymbol{I}_{\mathrm{dev}}^{\mathrm{sym}} &= \boldsymbol{I}^{\mathrm{sym}} - \frac{1}{3}\boldsymbol{I} \otimes \boldsymbol{I}, \\ \boldsymbol{I}^{\mathrm{sym}} &= \frac{1}{2}\big(\boldsymbol{I} \otimes \boldsymbol{I} + \boldsymbol{I} \underline{\otimes} \boldsymbol{I}\big), \\ \boldsymbol{A} \underline{\otimes} \boldsymbol{B} &= A_{il}B_{jk}\boldsymbol{e}_i \otimes \boldsymbol{e}_i \otimes \boldsymbol{e}_l \otimes \boldsymbol{e}_k. \end{aligned} \tag{2.6}$$

Before presenting the weak format, the Sobolev space is introduced in order to establish a foundation for the pertinent solution spaces:

$$\mathbb{H}^1(\Omega) \triangleq \left\{ \int_{\Omega} |\bullet|^2 + |\bullet \otimes \nabla|^2 \, \mathrm{d}\Omega < \infty \right\}. \tag{2.7}$$

The Sobolev space is used to define necessary regularity requirements for the studied field variables up to their first derivatives. The weak format can now be defined by multiplying Equation 2.3 with an arbitrary test function $\delta\boldsymbol{u}$ and integrating over the domain $\Omega_{\square}$, followed by partial integration and Gauss's divergence theorem while also inserting pertinent boundary conditions and the constitutive model:

Find $\boldsymbol{u} \in \mathbb{U}$ such that:

$$a^{(u)}(\boldsymbol{u}, \delta\boldsymbol{u}) = l(\delta\boldsymbol{u}) \quad \forall \delta\boldsymbol{u} \in \mathbb{U}^0, \tag{2.8}$$

where the variational forms were introduced:

$$\begin{aligned} a^{(u)}(\bullet, \bullet) &\triangleq \int_{\Omega_{\square}} \boldsymbol{\epsilon}[\bullet] : \boldsymbol{E} : \boldsymbol{\epsilon}[\bullet] \, \mathrm{d}\Omega, \\ l^{(u)}(\bullet) &\triangleq \int_{\Omega_{\square}} \boldsymbol{b} \cdot \bullet \, \mathrm{d}\Omega \int_{\Gamma_{\square,N}} \boldsymbol{t}_p \cdot \bullet \, \mathrm{d}\Gamma, \end{aligned} \tag{2.9}$$

together with the trial and test spaces:

$$\begin{aligned} \mathbb{U} &\triangleq \left\{ \boldsymbol{u} \in \mathbb{H}^1(\Omega_{\square}) |\ \ \boldsymbol{u} = \boldsymbol{u}_p \text{ on } \Gamma_{\square,D} \right\}, \\ \mathbb{U}^0 &\triangleq \left\{ \boldsymbol{u} \in \mathbb{H}^1(\Omega_{\square}) |\ \ \boldsymbol{u} = \boldsymbol{0} \text{ on } \Gamma_{\square,D} \right\}. \end{aligned} \tag{2.10}$$

Remark: The boundary integral related to the essential boundary $\Gamma_{\square,D}$ vanishes due to the choice of test space $\mathbb{U}^0$.

2.3.2 Diffusion at the microscale

The strong format of diffusivity is derived by considering a continuity equation where concentration fluxes move from regions of high concentration to regions of low concentration. It should be mentioned that diffusion takes place in the pores of the SVE meaning that the inverted phase of Figure 2.1 which is shown in Figure 2.3 is considered.

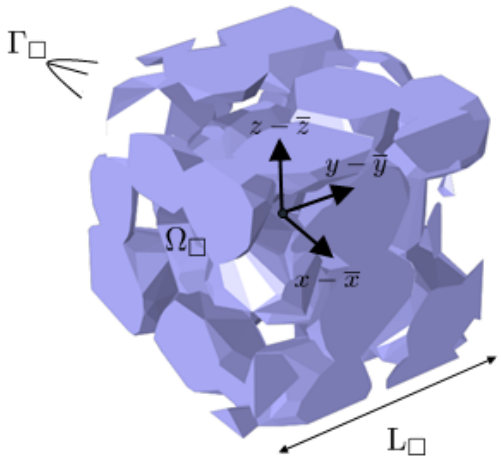

Figure 2.3: Illustration of the porous phase occupying the cubic SVE.

Similar to the elastic problem the strong format for subscale diffusion is presented for the SVE with essential and natural boundary conditions:

$$\begin{aligned} \boldsymbol{j}\cdot\boldsymbol{\nabla} &= R \quad \text{in} \quad \Omega_\square, \\ c &= c_p \quad \text{on} \quad \Gamma_{\square,D}, \\ j \triangleq \boldsymbol{j}\cdot\boldsymbol{n} &= j_p \quad \text{on} \quad \Gamma_{\square,N}, \end{aligned} \tag{2.11}$$

where $\boldsymbol{j}$ is the diffusive flux of the concentration, R is the net volumetric source of concentration c, c_p is the value of concentration on the essential part of the boundaries $\Gamma_{\square,D}$, and j is the flux along the normal directions of the natural part of the boundaries $\Gamma_{\square,N}$. The constitutive relation for the diffusion flux is specified as a linear isotropic law, more specifically Fick's law of diffusion [13] is used:

$$\boldsymbol{j} = -\boldsymbol{D}\cdot\boldsymbol{\nabla}c, \tag{2.12}$$

in which $\boldsymbol{D}$ denotes the diffusivity tensor. The weak format of microscale diffusivity can now be derived from strong format in Equation 2.3. An analogous procedure to that of the elastic problem is utilized but with test function δc, Fick's constitutive model, and boundary conditions pertaining to the diffusion problem. It follows, that the weak format for the diffusivity problem is governed by:

Find $c \in \mathbb{C}$ such that:

$$a^{(c)}(c,\delta c) = l^{(c)}(\delta c) \quad \forall \delta c \in \mathbb{C}^0, \tag{2.13}$$

where the variational forms were introduced:

$$\begin{aligned} a^{(c)}(\bullet,\bullet) &\triangleq \int_{\Omega_\square} \nabla\bullet\cdot\boldsymbol{D}\cdot\nabla\bullet \ \mathrm{d}\Omega, \\ l^{(c)}(\bullet) &\triangleq \int_{\Omega_\square} R\bullet \ \mathrm{d}\Omega + \int_{\Gamma_{\square,N}} j_p\bullet \ \mathrm{d}\Gamma, \end{aligned} \tag{2.14}$$

together with the trial and test spaces:

$$\begin{aligned} \mathbb{C} &\triangleq \left\{ c \in \mathbb{H}^1(\Omega_\square) |\ \ c = c_p \text{ on } \Gamma_{\square,D} \right\}, \\ \mathbb{C}^0 &\triangleq \left\{ c \in \mathbb{H}^1(\Omega_\square) |\ \ c = 0 \text{ on } \Gamma_{\square,D} \right\}. \end{aligned} \tag{2.15}$$

Remark: The boundary integral related to the essential boundary $\Gamma_{\square,D}$ vanishes due to the choice of test space $\mathbb{C}^0$.

2.4 Scale bridging

To establish the effective material properties the macroscale, the weak formats at the macroscale are defined [10]. Furthermore, boundary conditions are defined for the SVE to enable the macro-micro transition.

2.4.1 Linear elasticity at the macroscale

The elastic macroscale problem is defined for a domain Ω with natural and essential boundary conditions according to Figure 2.4. Analogously to that of the fine scale, the strong format for the elastic macroscale

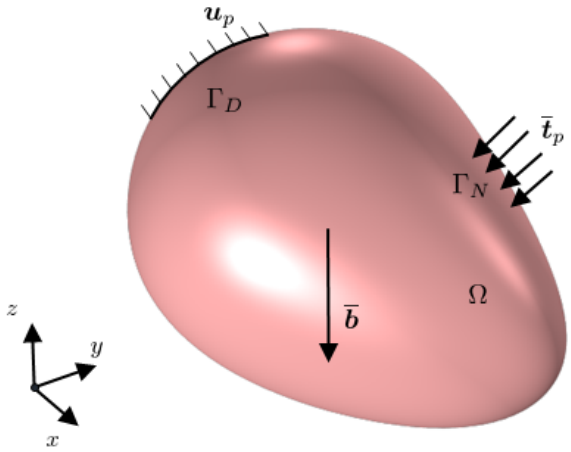

Figure 2.4: Illustration of a macro domain.

problem can be established according to:

$$\begin{aligned} -\overline{\boldsymbol{\sigma}} \cdot \boldsymbol{\nabla} &= \bar{\boldsymbol{b}} \quad \text{in} \quad \Omega, \\ \overline{\boldsymbol{u}} &= \overline{\boldsymbol{u}}_p \quad \text{on} \quad \Gamma_D, \\ \bar{\boldsymbol{t}} \triangleq \overline{\boldsymbol{\sigma}} \cdot \boldsymbol{n} &= \bar{\boldsymbol{t}}_p \quad \text{on} \quad \Gamma_N, \end{aligned} \tag{2.16}$$

where the constitutive equations are governed by:

$$\begin{aligned} \overline{\boldsymbol{\sigma}} &= \overline{\boldsymbol{E}} : \bar{\boldsymbol{\epsilon}}, \\ \bar{\boldsymbol{\epsilon}} = \boldsymbol{\epsilon}[\overline{\boldsymbol{u}}] &\triangleq (\overline{\boldsymbol{u}} \otimes \boldsymbol{\nabla})^{\text{sym}}. \end{aligned} \tag{2.17}$$

Now the weak format can derived by introducing the test function $\delta\overline{\boldsymbol{u}}$:

Find $\overline{\boldsymbol{u}} \in \mathbb{U}$ such that:

$$\overline{a}^{(u)}(\boldsymbol{u}, \delta\boldsymbol{u}) = \bar{l}(\delta\boldsymbol{u}) \quad \forall \delta\boldsymbol{u} \in \mathbb{U}^0, \tag{2.18}$$

where the variational forms were introduced:

$$\begin{aligned} \overline{a}^{(u)}(\bullet, \bullet) &\triangleq \int_\Omega \bar{\boldsymbol{\epsilon}}[\bullet] : \overline{\boldsymbol{E}} : \bar{\boldsymbol{\epsilon}}[\bullet] \, \mathrm{d}\Omega, \\ \bar{l}^{(u)}(\bullet) &\triangleq \int_\Omega \bar{\boldsymbol{b}} \cdot \bullet \, \mathrm{d}\Omega \int_{\Gamma_N} \bar{\boldsymbol{t}}_p \cdot \bullet \, \mathrm{d}\Gamma, \end{aligned} \tag{2.19}$$

together with the trial and test spaces:

$$\begin{aligned} \overline{\mathbb{U}} &\triangleq \left\{ \overline{\boldsymbol{u}} \in \mathbb{H}^1(\Omega) |\ \ \overline{\boldsymbol{u}} = \overline{\boldsymbol{u}}_p \text{ on } \Gamma_D \right\}, \\ \overline{\mathbb{U}}^0 &\triangleq \left\{ \boldsymbol{u} \in \mathbb{H}^1(\Omega) |\ \ \overline{\boldsymbol{u}} = \boldsymbol{0} \text{ on } \Gamma_D \right\}. \end{aligned} \tag{2.20}$$

The main issue with the macro scale problem is that the effective stiffness $\overline{\boldsymbol{E}}(\overline{\boldsymbol{x}})$ needs to be derived for any macro point $\overline{\boldsymbol{x}} \in \Omega$ in terms of the subscale variation of $\boldsymbol{E}(\boldsymbol{x})$ in a neighborhood of the macro point. It is here that the role of homogenization becomes crucial since it allows for the transition between the two scales.

2.4.2 Effective stiffness

It is noted that the effective stiffness tensor can be derived from Equation 2.17 if the macroscopic strains and stresses are known. Therefore, the strain and stress need to be evaluated by means of first order homogenization. The strain can be obtained by introducing a prolongation rule for the displacement field of the SVE according to Equation 2.2:

$$\boldsymbol{u}(\boldsymbol{x}) = \boldsymbol{u}^{\mathrm{M}}(\boldsymbol{x}) + \boldsymbol{u}^{\mu}(\boldsymbol{x}), \quad \boldsymbol{x} \in \Omega_{\square}, \tag{2.21}$$

such that the strain is given by:

$$\boldsymbol{\epsilon}(\boldsymbol{x}) = \overline{\boldsymbol{\epsilon}} + \boldsymbol{\epsilon}^{\mu}(\boldsymbol{x}), \quad \boldsymbol{\epsilon}^{\mu} = \boldsymbol{\epsilon}[\boldsymbol{u}^{\mu}], \quad \boldsymbol{x} \in \Omega_{\square}, \tag{2.22}$$

where the smooth strain $\overline{\boldsymbol{\epsilon}}$ is truly constant within $\Omega_{\square}$. It follows that the macroscopic displacement field can be defined according to:

$$\boldsymbol{u}^{\mathrm{M}}(\boldsymbol{x}) = \overline{\boldsymbol{u}} + \overline{\boldsymbol{\epsilon}} \cdot (\boldsymbol{x} - \overline{\boldsymbol{x}}), \tag{2.23}$$

in which $\overline{\boldsymbol{x}}$ denotes an arbitrary reference point in the SVE and $\overline{\boldsymbol{u}}$ the macroscale displacement field which can be chosen as zero since the solution is invariant with respect to rigid body modes. Now, the relation for the macroscopic strain needs to be defined. To this purpose strain control is used to solve the boundary value problem, meaning that the smooth strain field $\overline{\boldsymbol{\epsilon}}$ is prescribed. A direct consequence of strain control is that the strain identity:

$$\langle \boldsymbol{\epsilon} \rangle_{\square} = \overline{\boldsymbol{\epsilon}}, \tag{2.24}$$

must hold prior to solving. Upon specifying boundary conditions for the strain control while also choosing material parameters, the volume averaged stress $\overline{\boldsymbol{\sigma}}$ can be obtained for the the SVE as a post process step:

$$\overline{\boldsymbol{\sigma}} = \langle \boldsymbol{\sigma} \rangle_{\square}. \tag{2.25}$$

Now, when both quantities in Equation 2.17 are known, the effective stiffness can be evaluated accordingly. However, it still remains to define the proper boundary conditions for the homogenization process.

2.4.3 Strongly periodic boundary conditions for the elastic problem

One assumption for computational homogenization is that the fluctuating displacement field $u^{\mu}(x)$ in Equation 2.21 is periodic over the boundaries of the SVE, which stems from the assumption that the structure can be modeled by repetitive SVEs as shown in Figure 2.5. It can be noted that this requires the SVEs to be periodic such that each opposing side of the SVE is compatible. Furthermore, it should be clarified that periodicity only holds for the fluctuating field and not the macroscopic one.

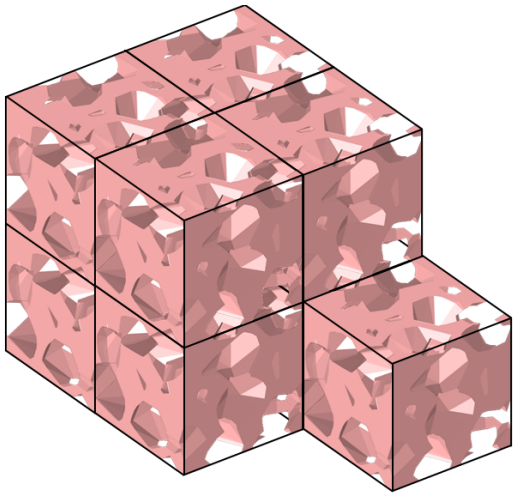

Figure 2.5: Macroscopic domain modeled as multiple periodic cells.

In this project strong periodic boundary conditions (SPBCs) are considered for the SVE. In order to explain the SPBCs the cubic unit cell with domain $\Omega_\square$ in Figure 2.6 is considered. Here, the boundaries of the domain $\Omega_\square$ have been split into two parts according to:

$$\Gamma_\square = \Gamma_\square^+ \cup \Gamma_\square^-, \tag{2.26}$$

where $\Gamma_\square^+$ is denoted the image boundary and $\Gamma_\square^-$ the mirror boundary. From the division, it is observed that each point on the image boundary has a corresponding point on the mirror boundary. Furthermore, the corner points of the domain are defined by:

$$\boldsymbol{x}_{\mathrm{c}}^{(i,j,k)} \triangleq \frac{L_\square}{2}\left(i\boldsymbol{e}_1 + j\boldsymbol{e}_2 + k\boldsymbol{e}_3\right), \tag{2.27}$$

where $L_\square$ is the side length and $i, j, k = -1$ or 1 for the origin placed in the center of the domain.

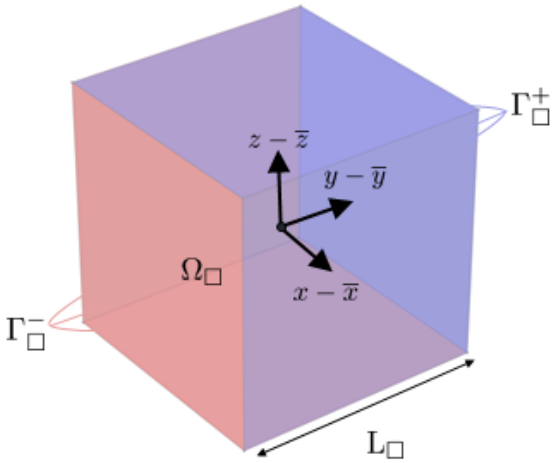

Figure 2.6: A cubic unit cell with mirror and image boundaries.

Now, periodicity can be imposed for the SVE by defining a mapping operator from the image to the mirror boundary:

$$\boldsymbol{\varphi}_{\mathrm{per}} : \Gamma_\square^+ \mapsto \Gamma_\square^-, \tag{2.28}$$

such that that each point $\boldsymbol{x}^+ \in \Gamma_\square^+$ can be mapped onto the mirror boundary:

$$\boldsymbol{x}^- = \boldsymbol{\varphi}_{\mathrm{per}}(\boldsymbol{x}^+). \tag{2.29}$$

It is observed that the mapping can be applied for each boundary point except for the corner points since these have three mirror pairs. Hence, the corner points are dealt with separately as an auxiliary constraint. The periodicity of the fluctuation field can now be stated as:

$$\boldsymbol{u}(\boldsymbol{x})^\mu = \boldsymbol{u}^\mu(\boldsymbol{\varphi}_{\mathrm{per}}(\boldsymbol{x})) \quad \forall \boldsymbol{x} \in \Gamma_\square^+, \tag{2.30}$$

or equivalently as:

$$[\![\boldsymbol{u}^\mu]\!]_\square = 0 \quad \forall \boldsymbol{x} \in \Gamma_\square^+, \tag{2.31}$$

where the jump operator $[\![\bullet]\!]_\square$ is defined according to:

$$[\![\bullet]\!]_\square = 0, \quad [\![\bullet]\!]_\square \triangleq \bullet(\boldsymbol{x}) - \bullet(\boldsymbol{\varphi}(\boldsymbol{x})) \quad \forall \boldsymbol{x} \in \Gamma_\square^+. \tag{2.32}$$

Additionally, it follows from the antiperiodicity of the boundary normals $\boldsymbol{n}$, that the tractions $\boldsymbol{t}$ becomes antiperiodic:

$$\boldsymbol{t}(\boldsymbol{x}) = -\boldsymbol{t}\left(\boldsymbol{\varphi}_{\mathrm{per}}\left(\boldsymbol{x}\right)\right) \quad \forall \boldsymbol{x} \in \Gamma_\square^+. \tag{2.33}$$

To satisfy periodicity for the corners, it is noted that each corner point must contain the same solution for the fluctuating displacement such that:

$$\boldsymbol{u}^\mu(\boldsymbol{x}_c^{i,j,k}) = \boldsymbol{u}_c^\mu. \tag{2.34}$$

Consequently, the SPBC requires that the fluctuating displacement is periodic over the external boundaries for the unit cell while the tractions are antiperiodic. Moreover, the mapping for SPBCs requires that these two constraints must hold pointwise on the boundaries. From an FEA point of view this enforces the use of a strictly periodic mesh along $\Gamma_\square^+$ and $\Gamma_\square^-$. By using the prolongation rule it can be shown that the strain identity in Equation 2.24 is satisfied for the choice of SPBCs:

$$\begin{aligned}
\langle \boldsymbol{\epsilon} \rangle_\square &\triangleq \frac{1}{|\Omega_\square|} \left(\int_{\Omega_\square} (\boldsymbol{u}(\boldsymbol{x})) \otimes \boldsymbol{\nabla} \, \mathrm{d}\Omega \right)^{\mathrm{sym}} \\
&= \frac{1}{|\Omega_\square|} \left(\int_{\Omega_\square} (\overline{\boldsymbol{\epsilon}} \cdot [\boldsymbol{x} - \overline{\boldsymbol{x}}] + \boldsymbol{u}^\mu(\boldsymbol{x})) \otimes \boldsymbol{\nabla} \, \mathrm{d}\Omega \right)^{\mathrm{sym}} \\
&= \frac{1}{|\Omega_\square|} \left(\int_{\Omega_\square} (\overline{\boldsymbol{\epsilon}} \cdot [\boldsymbol{x} - \overline{\boldsymbol{x}}]) \otimes \boldsymbol{\nabla} \, \mathrm{d}\Omega + \int_{\Gamma_\square} \boldsymbol{u}^\mu(\boldsymbol{x}) \otimes \boldsymbol{n}(\boldsymbol{x}) \, \mathrm{d}\Gamma \right)^{\mathrm{sym}} \\
&= \frac{1}{|\Omega_\square|} \left(\overline{\boldsymbol{\epsilon}} \cdot \int_{\Omega_\square} \underbrace{([\boldsymbol{x} - \overline{\boldsymbol{x}}]) \otimes \boldsymbol{\nabla}}_{\boldsymbol{I}} \, \mathrm{d}\Omega + \int_{\Gamma_\square^+} \boldsymbol{u}^\mu(\boldsymbol{x}^+) \otimes \boldsymbol{n}(\boldsymbol{x}^+) \, \mathrm{d}\Gamma + \int_{\Gamma_\square^-} \boldsymbol{u}^\mu(\boldsymbol{x}^-) \otimes \boldsymbol{n}(\boldsymbol{x}^-) \, \mathrm{d}\Gamma \right)^{\mathrm{sym}} \\
&= \overline{\boldsymbol{\epsilon}} + \frac{1}{|\Omega_\square|} \left(\int_{\Gamma_\square^+} \boldsymbol{u}^\mu(\boldsymbol{x}^+) \otimes \boldsymbol{n}(\boldsymbol{x}^+) \, \mathrm{d}\Gamma + \int_{\Gamma_\square^+} \boldsymbol{u}^\mu(\boldsymbol{\varphi}_{\mathrm{per}}(\boldsymbol{x}^+)) \otimes \boldsymbol{n}(\boldsymbol{\varphi}_{\mathrm{per}}(\boldsymbol{x}^+)) \, \mathrm{d}\Gamma \right)^{\mathrm{sym}} \\
&= \overline{\boldsymbol{\epsilon}} + \frac{1}{|\Omega_\square|} \left(\int_{\Gamma_\square^+} \boldsymbol{u}^\mu(\boldsymbol{x}^+) \otimes \left(\boldsymbol{n}(\boldsymbol{x}^+) - \boldsymbol{n}(\boldsymbol{x}^+) \right) \, \mathrm{d}\Gamma \right)^{\mathrm{sym}} = \overline{\boldsymbol{\epsilon}},
\end{aligned} \tag{2.35}$$

where the antiperiodicity of the boundary normals was used to end up with the last expression, and the identity:

$$\int_\Omega \bullet \otimes \boldsymbol{\nabla} \, \mathrm{d}\Omega = \int_\Gamma \bullet \otimes \boldsymbol{n} \, \mathrm{d}\Gamma, \tag{2.36}$$

which can be derived through Gauss's divergence theorem, was used to rewrite the volume integral as a boundary integral. The macroscale problem is defined with the constraint of SPBCs by considering a homogenized version of Equation 2.9:

$$\frac{1}{|\Omega_\square|} \int_{\Omega_\square} \boldsymbol{\epsilon}[\boldsymbol{u}] : \mathbf{E} : \boldsymbol{\epsilon}[\delta \boldsymbol{u}] \, \mathrm{d}\Omega - \frac{1}{|\Omega_\square|} \int_{\Gamma_\square} \boldsymbol{t} \cdot \delta \boldsymbol{u} \, \mathrm{d}\Gamma = 0, \tag{2.37}$$

where the body force is neglected in this project, and the boundary integral is modified to correspond to the boundaries in Figure 2.6. By utilizing the properties of SPBC it is shown that the boundary integral in Equation 2.57 vanishes:

$$\begin{aligned}
\frac{1}{|\Omega_\square|} \int_{\Gamma_\square} \boldsymbol{t}(\boldsymbol{x}) \cdot \delta \boldsymbol{u}(\boldsymbol{x}) \, \mathrm{d}\Gamma &= \frac{1}{|\Omega_\square|} \left(\int_{\Gamma_\square^+} \boldsymbol{t}(\boldsymbol{x}^+) \cdot \delta \boldsymbol{u}(\boldsymbol{x}^+) \, \mathrm{d}\Gamma + \int_{\Gamma_\square^-} \boldsymbol{t}(\boldsymbol{x}^-) \cdot \delta \boldsymbol{u}(\boldsymbol{x}^-) \, \mathrm{d}\Gamma \right) \\
&= \frac{1}{|\Omega_\square|} \left(\int_{\Gamma_\square^+} \boldsymbol{t}(\boldsymbol{x}^+) \cdot \delta \boldsymbol{u}(\boldsymbol{x}^+) \, \mathrm{d}\Gamma + \int_{\Gamma_\square^+} \boldsymbol{t}(\boldsymbol{\varphi}_{\mathrm{per}}(\boldsymbol{x}^+)) \cdot \delta \boldsymbol{u}(\boldsymbol{\varphi}_{\mathrm{per}}(\boldsymbol{x}^+)) \, \mathrm{d}\Gamma \right) \\
&= \frac{1}{|\Omega_\square|} \int_{\Gamma_\square^+} \left[\boldsymbol{t}(\boldsymbol{x}^+) - \boldsymbol{t}(\boldsymbol{x}^+) \right] \cdot \delta \boldsymbol{u}(\boldsymbol{x}^+) \, \mathrm{d}\Gamma = 0.
\end{aligned} \tag{2.38}$$

Finally, the weak format for an SVE under strain control with SPBC can be defined by making use of the prolongation rule in Equation 2.21:

For a given value of the macroscale $\overline{\boldsymbol{\epsilon}}$, find the displacement field $\boldsymbol{u}^{\mu} \in \mathbb{U}_{\square}^{P,0}$ such that:

$$a_{\square}^{(u)}(\boldsymbol{u}^{\mu}, \delta\boldsymbol{u}) = l_{\square}^{(u)}(\delta\boldsymbol{u}) \quad \forall \delta\boldsymbol{u} \in \mathbb{U}_{\square}^{P,0}, \tag{2.39}$$

where the variational forms were introduced:

$$\begin{aligned} a_{\square}^{(u)}(\bullet, \bullet) &= \langle \boldsymbol{\epsilon}\left[\bullet\right] : \boldsymbol{E} : \epsilon[\bullet] \rangle_{\square}\,, \\ l_{\square}^{(u)}(\bullet) &= -\overline{\boldsymbol{\epsilon}} : \langle \boldsymbol{E} : \boldsymbol{\epsilon}\left[\bullet\right] \rangle_{\square}, \end{aligned} \tag{2.40}$$

together with the function spaces:

$$\begin{aligned} \mathbb{U}_{\square}^{P,0} &\triangleq \left\{ \boldsymbol{u} \in \mathbb{U}_{\square} |\ \ [\![\boldsymbol{u}]\!]_{\square} = \boldsymbol{0} \text{ on } \Gamma_{\square}^{+} \right\} \\ \mathbb{U}_{\square} &\triangleq \left\{ \boldsymbol{u} \in \mathbb{H}^1(\Omega_{\square}) |\ \ \int_{\Omega_{\square}} \boldsymbol{u}\, \mathrm{d}\Omega = \boldsymbol{0} |\ \ \int_{\Gamma_{\square}} (\boldsymbol{u} \otimes \boldsymbol{n})^{\mathrm{skw}}\, \mathrm{d}\Gamma = \boldsymbol{0} \right\}. \end{aligned} \tag{2.41}$$

Remark: $\int_{\Omega_{\square}} \boldsymbol{u}\, \mathrm{d}\Omega = \boldsymbol{0}$ and $\int_{\Gamma_{\square}} (\boldsymbol{u} \otimes \boldsymbol{n})^{\mathrm{skw}}\, \mathrm{d}\Gamma = \boldsymbol{0}$ prevent rigid body modes in translation and rotation respectively to ensure that the solution is unique.

2.4.4 Diffusion at the macroscale

Analogously to the macro-elasticity problem the diffusion problem is derived for the coarse domain in Figure 2.4 where the SVE in Figure 2.3 represents the subscale problem:

$$\begin{aligned} \overline{\boldsymbol{j}} \cdot \boldsymbol{\nabla} &= \overline{R} \quad \text{in} \quad \Omega, \\ \overline{c} &= \overline{c}_p \quad \text{on} \quad \Gamma_D, \\ \overline{j} \triangleq \overline{\boldsymbol{j}} \cdot \boldsymbol{n} &= \overline{j}_p \quad \text{on} \quad \Gamma_N, \end{aligned} \tag{2.42}$$

in which the macroscopic flux is defined as:

$$\overline{\boldsymbol{j}} = -\overline{\boldsymbol{D}} \cdot \boldsymbol{\nabla} \overline{c}. \tag{2.43}$$

It thus follows that the weak format of macroscale diffusivity becomes:

Find $\overline{c} \in \mathbb{C}$ such that:

$$\overline{a}^{(c)}(\overline{c}, \delta\overline{c}) = \overline{l}^{(c)}(\delta\overline{c}) \quad \forall \delta\overline{c} \in \mathbb{C}^0, \tag{2.44}$$

where the variational forms were introduced:

$$\begin{aligned} \overline{a}^{(c)}(\bullet, \bullet) &\triangleq \int_{\Omega} \nabla \bullet \cdot \overline{\boldsymbol{D}} \cdot \nabla \bullet\ \mathrm{d}\Omega, \\ \overline{l}^{(c)}(\bullet) &\triangleq \int_{\Omega} \overline{R} \bullet\ \mathrm{d}\Omega + \int_{\Gamma_N} \overline{j}_p \bullet\ \mathrm{d}\Gamma, \end{aligned} \tag{2.45}$$

together with the trial and test spaces:

$$\begin{aligned} \overline{\mathbb{C}} &\triangleq \left\{ \overline{c} \in \mathbb{H}^1(\Omega) |\ \ \overline{c} = \overline{c}_p \text{ on } \Gamma_D \right\}, \\ \overline{\mathbb{C}}^0 &\triangleq \left\{ \overline{c} \in \mathbb{H}^1(\Omega) |\ \ \overline{c} = 0 \text{ on } \Gamma_D \right\}. \end{aligned} \tag{2.46}$$

Again, the key issue is to derive an expression for the constitutive tensor since the macroscale diffusion tensor $\overline{\boldsymbol{D}}(\overline{\boldsymbol{x}})$ is unknown for any $\overline{\boldsymbol{x}} \in \Omega$. Thus, computational homogenization is once again required to derive a macroscale expression.

2.4.5 Effective diffusivity

Using first order homogenization the diffusion stiffness tensor can be derived from Equation 2.12 given the values of the macroscopic concentration gradients $\boldsymbol{\nabla}\overline{c}$ and the fluxes $\overline{\boldsymbol{j}}$. Consequently, the concentrations are split into a fluctuating part and a smooth linear contribution according to Equation 2.2:

$$c(\boldsymbol{x}) = c^{\mathrm{M}}(\boldsymbol{x}) + c^{\mu}(\boldsymbol{x}), \quad \boldsymbol{x} \in \Omega_{\square}, \tag{2.47}$$

such that the concentration gradient becomes:

$$\boldsymbol{\nabla} c(\boldsymbol{x}) = \boldsymbol{\nabla}\overline{c} + \boldsymbol{\nabla} c^{\mu}(\boldsymbol{x}), \quad \boldsymbol{x} \in \Omega_{\square}. \tag{2.48}$$

It is realized that the macroscopic concentration can be expressed as:

$$c^{\mathrm{M}}(\boldsymbol{x}) = \boldsymbol{\nabla}\overline{c} \cdot [\boldsymbol{x} - \overline{\boldsymbol{x}}], \quad \boldsymbol{x} \in \Omega_{\square} \tag{2.49}$$

since any macroscopic contribution $\overline{c}$ can be set to zero due to the solution being invariant to the level of $\overline{c}$. By controlling the value of $\overline{c}$ it is noted that the identity:

$$\langle c \rangle_{\square} = \overline{c}, \tag{2.50}$$

must be satisfied prior to solving. After solving the subscale problem, the macroscopic flux is obtained by volume averaging the SVE:

$$\overline{\boldsymbol{j}} = \langle \boldsymbol{j} \rangle_{\square}, \tag{2.51}$$

meaning that the effective diffusivity can be evaluated after assigning sufficient boundary conditions to the SVE.

2.4.6 Strongly periodic boundary conditions for the diffusion problem

Once again, SPBCs are considered for fluctuating contribution of the SVE in Figure 2.6 where the mapping is governed by Equation 2.29. The periodicity of the concentrations can now be defined according to:

$$[\![c^{\mu}]\!]_{\square} = 0 \quad \forall \boldsymbol{x} \in \Gamma^{+}_{\square}, \tag{2.52}$$

and the antiperiodicity of the normal fluxes as:

$$j(\boldsymbol{x}) = -j\left(\boldsymbol{\varphi}_{\mathrm{per}}\left(\boldsymbol{x}\right)\right) \quad \forall \boldsymbol{x} \in \Gamma^{+}_{\square}. \tag{2.53}$$

The auxiliary condition for the corners of the SVE must also hold:

$$c^{\mu}(\boldsymbol{x}_c^{i,j,k}) = c_c^{\mu}. \tag{2.54}$$

Using the split of concentrations it is shown that the identity in Equation 2.50 is satisfied for SPBCs when $\boldsymbol{\nabla}\overline{c}$ is prescribed:

$$\begin{aligned}
\langle \boldsymbol{\nabla} c \rangle_{\square} &\triangleq \frac{1}{|\Omega_{\square}|} \int_{\Omega_{\square}} \boldsymbol{\nabla} c(\boldsymbol{x}) \, \mathrm{d}\Omega \\
&= \frac{1}{|\Omega_{\square}|} \int_{\Omega_{\square}} \boldsymbol{\nabla} \left(\boldsymbol{\nabla}\overline{c} \cdot [\boldsymbol{x} - \overline{\boldsymbol{x}}] + c^{\mu}(\boldsymbol{x}) \right) \, \mathrm{d}\Omega \\
&= \frac{1}{|\Omega_{\square}|} \left(\int_{\Omega_{\square}} \boldsymbol{\nabla} (\boldsymbol{\nabla}\overline{c} \cdot [\boldsymbol{x} - \overline{\boldsymbol{x}}]) \, \mathrm{d}\Omega + \int_{\Gamma_{\square}} c^{\mu}(\boldsymbol{x}) \boldsymbol{n}(\boldsymbol{x}) \, \mathrm{d}\Gamma \right) \\
&= \frac{1}{|\Omega_{\square}|} \left(\boldsymbol{\nabla}\overline{c} \cdot \int_{\Omega_{\square}} \underbrace{\boldsymbol{\nabla}[\boldsymbol{x} - \overline{\boldsymbol{x}}]}_{\boldsymbol{I}} \, \mathrm{d}\Omega + \int_{\Gamma^{+}_{\square}} c^{\mu}(\boldsymbol{x}^{+}) \boldsymbol{n}(\boldsymbol{x}^{+}) \, \mathrm{d}\Gamma + \int_{\Gamma^{-}_{\square}} c^{\mu}(\boldsymbol{x}^{-}) \boldsymbol{n}(\boldsymbol{x}^{-}) \, \mathrm{d}\Gamma \right) \\
&= \boldsymbol{\nabla}\overline{c} + \frac{1}{|\Omega_{\square}|} \left(\int_{\Gamma^{+}_{\square}} c^{\mu}(\boldsymbol{x}^{+}) \boldsymbol{n}(\boldsymbol{x}^{+}) \, \mathrm{d}\Gamma + \int_{\Gamma^{+}_{\square}} c^{\mu}(\boldsymbol{\varphi}_{\mathrm{per}}(\boldsymbol{x}^{+})) \boldsymbol{n}(\boldsymbol{\varphi}_{\mathrm{per}}(\boldsymbol{x}^{+})) \, \mathrm{d}\Gamma \right) \\
&= \boldsymbol{\nabla}\overline{c} + \frac{1}{|\Omega_{\square}|} \left(\int_{\Gamma^{+}_{\square}} c^{\mu}(\boldsymbol{x}^{+}) \left(\boldsymbol{n}(\boldsymbol{x}^{+}) - \boldsymbol{n}(\boldsymbol{x}^{+}) \right) \, \mathrm{d}\Gamma \right) = \boldsymbol{\nabla}\overline{c},
\end{aligned} \tag{2.55}$$

where the identity:

$$\int_{\Omega} \boldsymbol{\nabla} \bullet \, \mathrm{d}\Omega = \int_{\Gamma} \boldsymbol{n} \bullet \, \mathrm{d}\Gamma, \tag{2.56}$$

was used to rewrite the volume integral. The volume averaged version of the diffusion weak format Equation 2.13 is now introduced while omitting the volumetric source of concentration:

$$\frac{1}{|\Omega_\square|} \int_{\Omega_\square} \boldsymbol{\nabla} c \cdot \boldsymbol{D} \cdot \boldsymbol{\nabla} c \, \mathrm{d}\Omega - \frac{1}{|\Omega_\square|} \int_{\Gamma_\square} j \cdot \delta c \, \mathrm{d}\Gamma = 0, \tag{2.57}$$

Again it is shown that the boundary term vanishes for SPBCs:

$$\begin{aligned} \frac{1}{|\Omega_\square|} \int_{\Gamma_\square} j(\boldsymbol{x}) \cdot \delta c(\boldsymbol{x}) \, \mathrm{d}\Gamma &= \frac{1}{|\Omega_\square|} \left(\int_{\Gamma_\square^+} j(\boldsymbol{x}^+) \cdot \delta c(\boldsymbol{x}^+) \, \mathrm{d}\Gamma + \int_{\Gamma_\square^-} j(\boldsymbol{x}^-) \cdot \delta c(\boldsymbol{x}^-) \, \mathrm{d}\Gamma \right) \\ &= \frac{1}{|\Omega_\square|} \left(\int_{\Gamma_\square^+} j(\boldsymbol{x}^+) \cdot \delta c(\boldsymbol{x}^+) \, \mathrm{d}\Gamma + \int_{\Gamma_\square^+} j(\boldsymbol{\varphi}_{\mathrm{per}}(\boldsymbol{x}^+)) \cdot \delta c(\boldsymbol{\varphi}_{\mathrm{per}}(\boldsymbol{x}^+)) \, \mathrm{d}\Gamma \right) \\ &= \frac{1}{|\Omega_\square|} \int_{\Gamma_\square^+} \big(j(\boldsymbol{x}^+) - j(\boldsymbol{x}^+) \big) \cdot \delta c(\boldsymbol{x}^+) \, \mathrm{d}\Gamma = 0. \end{aligned} \tag{2.58}$$

Finally, the weak format of diffusivity for the SVE is stated:

For a given value of the macroscale concentration gradient $\boldsymbol{\nabla}\overline{c}$, find the concentration $c^\mu \in \mathbb{C}_\square^{P,0}$ such that:

$$a_\square^{(c)}(\boldsymbol{c}^\mu, \delta\boldsymbol{c}) = l_\square^{(c)}(\delta\boldsymbol{c}) \quad \forall \delta\boldsymbol{c} \in \mathbb{C}_\square^{P,0}, \tag{2.59}$$

where the variational forms were introduced:

$$\begin{aligned} a_\square^{(c)}(\bullet, \bullet)_\square &= \langle \bullet \cdot \boldsymbol{D} \cdot \bullet \rangle, \\ l_\square^{(c)}(\bullet) &= -\boldsymbol{\nabla}\overline{c} \cdot \langle \boldsymbol{D} \cdot \boldsymbol{\nabla} \bullet \rangle_\square, \end{aligned} \tag{2.60}$$

together with the function spaces:

$$\begin{aligned} \mathbb{C}_\square^{P,0} &\triangleq \left\{ c \in \mathbb{C}_\square | \;\; [\![c]\!]_\square = 0 \text{ on } \Gamma_\square^+ \right\} \\ \mathbb{C} &\triangleq \left\{ c \in \mathbb{H}^1(\Omega_\square) | \;\; \int_{\Omega_\square} c \, \mathrm{d}\Omega = 0 \right\}. \end{aligned} \tag{2.61}$$

Remark: The constraint $\int_{\Omega_\square} c \, \mathrm{d}\Omega = 0$ entails that the solution is unique for the SVE.

3 Synthetic microstructures

Four primary types of synthetic microstructures are presented. For the structures to be feasible to implement in COMSOL they need to be realized in a CAD representation, where the STEP format is chosen as the standard. The ideal is for the full process to be automated, such that there should be no dependency on user input after the input parameters have been given. Some of the microstructure generation techniques apply physical equations to generate a topology. It needs to be remarked that these equations are not necessarily meant to mimic the physics behind the electrolyte manufacturing process. The equations are convenient mathematics that can be exploited to obtain natural-like microstructures.

Examples of SBE samples from research into the manufacturing process are shown in Figure 3.1. Examples of the generated synthetic microstructures can be found in appendix A.

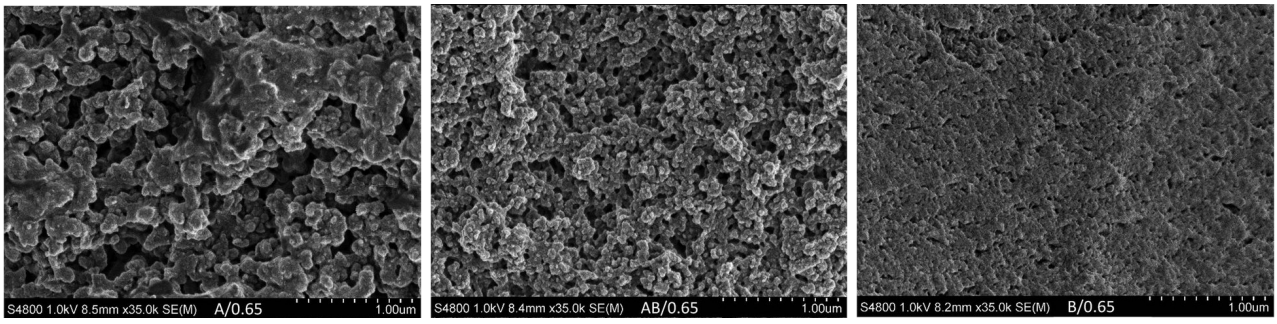

(a) Sample A/0.65. **(b)** Sample B/0.65. **(c)** Sample AB/0.65.

Figure 3.1: SEM images of SBE samples where there liquid electrolyte has been drained. All images were taken at 35k magnification. Reproduced from N.Ihrner et al [5] under CC BY 4.0 license. Original image was cropped to fit horizontally. Sample names refer to chemical compositions used in the cited paper.

3.1 Cahn-Hilliard

The Cahn-Hilliard equation models phase separation of a homogeneous mixture in which two components spontaneously separate from each other and form two distinct domains. This spinodal decomposition can be used as a mean to generate synthetic microstructures [14] [15]. In this project the Cahn-Hilliard equation is evaluated for a cubic unit domain to construct SVEs, where the morphology is obtained by filtering for field variables of phase concentrations. If c is the concentration for one of the phases in the fluid, the Cahn-Hilliard equation can be introduced according to:

$$\frac{\partial c}{\partial t} = \boldsymbol{\nabla} \cdot (M \boldsymbol{\nabla} \mu) = M \Delta \mu, \quad \boldsymbol{x}, t \in \Omega_{\square} \times \mathbb{R}^{+} \tag{3.1}$$

Here the $\Omega_{\square}$ denotes a bounded domain with smooth boundaries $\Gamma_{\square}$, $\mathbb{R}^{+}$ denotes the set of all positive real numbers, t is the evolution time, $\boldsymbol{x}$ is a material point in $\Omega_{\square}$, M is the mobility coefficient, and μ is the chemical potential defined according to:

$$\mu = \frac{\partial F[c]}{\partial c} - \gamma \delta c. \tag{3.2}$$

In Equation 3.2, γ represents the length of the transition zones between the phases, and $F[c]$ denotes the homogeneous free energy density functional. Using Landau theory, the functional of the free energy can be approximated by a power series [14], such that:

$$F[c] = \alpha (c - \beta)^2 (c - \gamma)^2, \tag{3.3}$$

where α β, and γ can be chosen appropriately. By introducing ϕ as the difference in concentrations between two phases A and B for any point in Ω as:

$$\phi = c_A - c_B \quad \text{with} \quad c_A + c_B = 1, \tag{3.4}$$

and letting $c = c_A$, it follows that $\phi = 2c - 1$. In this project periodic unit cells are used with SPBCs for the homogenization, meaning that the resulting morphology from the Cahn-Hilliard equation must be periodic. Hence, the Cahn-Hilliard equation is applied to the cubic domain while imposing a periodic concentration field along the boundaries of the computational domain. Using SPBCs and introducing the constitutive variables $\boldsymbol{q}_\mu$ and $\boldsymbol{q}_\phi$, it becomes possible to write the strong format in Equation 3.1 as two coupled differential equations such that:

$$\begin{aligned}
\dot{\phi} + \boldsymbol{q}_\mu \cdot \boldsymbol{\nabla} &= 0 && \text{in} \quad \Omega_\square \times \mathbb{R}^+, \\
\Phi + \boldsymbol{q}_\phi \cdot \boldsymbol{\nabla} &= 0 && \text{in} \quad \Omega_\square \times \mathbb{R}^+, \\
[\![\mu]\!]_\square &= 0 && \text{on} \quad \Gamma^+_\square \times \mathbb{R}^+, \\
[\![\phi]\!]_\square &= 0 && \text{on} \quad \Gamma^+_\square \times \mathbb{R}^+, \\
q_\mu(\boldsymbol{x}) &= -q_\mu(\varphi_{\text{per}}(\boldsymbol{x})) && \text{on} \quad \Gamma^+_\square \times \mathbb{R}^+, \\
q_\phi(\boldsymbol{x}) &= -q_\phi(\varphi_{\text{per}}(\boldsymbol{x})) && \text{on} \quad \Gamma^+_\square \times \mathbb{R}^+,
\end{aligned} \tag{3.5}$$

where the constitutive relations are governed by:

$$\begin{aligned}
\boldsymbol{q}_\mu &\triangleq -M\boldsymbol{\nabla}\mu, \\
\boldsymbol{q}_\phi &\triangleq -\gamma\boldsymbol{\nabla}\phi, \\
\Phi &\triangleq \phi^3 - \phi - \mu, \\
q_\mu &\triangleq \boldsymbol{q}_\mu \cdot \boldsymbol{n}, \\
q_\phi &\triangleq \boldsymbol{q}_\phi \cdot \boldsymbol{n}.
\end{aligned} \tag{3.6}$$

For clarity, it should be mentioned that periodicity is imposed without the finescale and macroscale decomposition that was considered during the homogenization process. `COMSOL's` solver requires that the differential equation is implemented in a weak format. So the pertinent weak format is derived by multiplying the rows in Equation 3.5 with the arbitrary test functions $\delta\mu$ and $\delta\phi$ while integrating over the domain $\Omega_\square$. After applying partial integration and Gauss's divergence theorem it is realized that the surface contributions vanish analogously to Equation 2.58. Thus, the following weak format is obtained:

Find μ, $\phi \in \mathbb{M}^0 \times \mathbb{\Phi}^0$ such that:

$$\begin{aligned}
a^{(\mu)}(\mu, \delta\mu) + b(\dot{\phi}, \delta\mu) = 0 \quad \forall \delta\mu \in \mathbb{M}^0, \\
a^{(\phi)}(\phi, \delta\phi) + b(\Phi, \delta\phi) = 0 \quad \forall \delta\mu \in \mathbb{\Phi}^0,
\end{aligned} \tag{3.7}$$

where the variational forms were introduced:

$$\begin{aligned}
a^{(\mu)}(\bullet, \bullet) &\triangleq \int_{\Omega_\square} M\nabla \bullet \cdot \nabla \bullet \ \mathrm{d}\Omega, \\
a^{(\phi)}(\bullet, \bullet) &\triangleq \int_{\Omega_\square} \gamma\nabla \bullet \cdot \nabla \bullet \ \mathrm{d}\Omega, \\
b(\bullet, \bullet) &\triangleq \int_{\Omega_\square} \bullet \bullet \ \mathrm{d}\Omega,
\end{aligned} \tag{3.8}$$

together with the trial and test spaces:

$$\begin{aligned}
\mathbb{M}^0 &\triangleq \left\{ \mu \in \mathbb{H}^1(\Omega_\square) |\ [\![\mu]\!]_\square = 0 \text{ on } \Gamma^+_\square \times \mathbb{R}^+ \right\}, \\
\mathbb{\Phi}^0 &\triangleq \left\{ \phi \in \mathbb{H}^1(\Omega_\square) |\ [\![\phi]\!]_\square = 0 \text{ on } \Gamma^+_\square \times \mathbb{R}^+ \right\},
\end{aligned} \tag{3.9}$$

The SVE is modeled in `COMSOL` by applying the Cahn-Hilliard equation to a solid unit cube. Since the microstructure generation is artificial, and no parameter recommendations are available for the mobility, transition length, and simulation time, these are chosen arbitrarily for the microstructure generation. By specifying initial conditions for the concentrations, enforcing periodicity, and defining a time domain for the phase evolution, the weak format in Equation 3.7 is implemented in `COMSOL's` partial differential equation (PDE)

module. Initial conditions are prescribed by giving a starting value to the concentration. By construction the value of the initial concentration equals the volume fraction occupied by one of the phases. Thus, the volume fraction of the resulting SVE domains can be determined from a preset concentration value. To make each generated sample unique, random normal distributed noise is added to the initial concentration keeping the average value fixed in the spatial domain while changing the distribution.

The morphology for both phases of the Cahn-Hilliard equation look similar, making the choice for the domains of the SVE arbitrary. For the sake of simplicity, the solid domain is chosen as the domain for which the volume fraction equals the initial concentration. By applying an element filter to the solution, the solid part of the SVE is extracted as a closed triangular surface mesh containing vertex coordinates and connectivity indices for the triangles enclosing the solid domain. Due to the periodic boundary conditions the generated SVEs are periodic. A solved sample of the Cahn-Hilliard equation and the filtered solution pertaining to the solid SVE domain are shown in Figure 3.2.

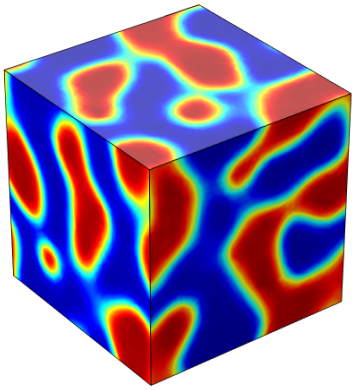

(a) Cahn-Hilliard solution for 50% volume fraction.

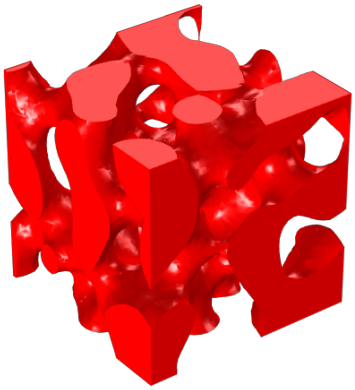

(b) Cahn-Hilliard solution after applying the element filter.

Figure 3.2: Cahn-Hilliard solution showing the two phases occupied in the cubic domain and a domain after element filtering.

To generate a solid out of the surface mesh the open source CAD software `FreeCAD` can be used together with its `Python` API. First, vertex coordinates and connectivity indices are used to construct closed shell structures. Since the generated surface mesh might contain disjoint domains, see Figure 3.3, and since the conversion in `FreeCAD` from shell to solid only works for individual shell objects, all shells must be constructed separately. It is noted, that if two faces share a vertex they must belong to the same shell, meaning that singular shells can be identified by searching for shared vertices of triangular faces. By traversing through all vertices and finding common nodes, the individual shells are constructed and converted to solids. Creating a union between all solids, the SVE pertaining to the solid phase can be exported into STEP format. Furthermore, the inverted structure can exported by computing a difference operation between a unit cube the solid domain, resulting in two objects ready for FEA.

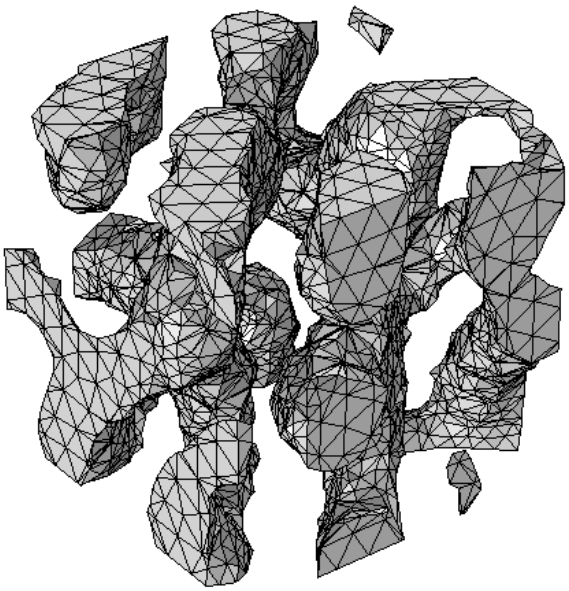

Figure 3.3: Cahn-Hilliard mesh with isolated domains at 32% solid volume fraction.

3.2 Sphere packing

A packing or distribution of spherical particles inside a unit domain can both be used for generating microstructures and as a basis for other generation techniques. The Lubachevsky-Stillinger algorithm [16] is an event driven method for generating dense packings of spheres using molecular dynamics. The algorithm is implemented using the library `PackLSD` [17]. Particles are distributed in a unit domain and assigned a radius and a random initial velocity. The particles will grow in size over time as they move inside the domain and collide. The simulation will stop once it reaches any of its stopping criteria. For a dense packing that maximizes the possible volume one would use a time or pressure criteria, see the evolution of a sphere packing in Figure 3.4. For non-dense packings the simplest criteria is a maximum volume fraction in the domain. The `PackLSD` implementation allows for bidisperse packings with two species of particles with radii and ratio that may be set by the user. It also allows different boundary conditions for the walls, with the default being periodic walls. Since the particles are allowed to collide they will never overlap. To create a continuous solid microstructure based on a sphere packing this lack of an overlap needs to adjusted as a post-processing step. A simple method is to swell all spheres by multiplying their radii by a factor.

The idea is to generate a packing of spheres and read them into `FreeCAD`. In `FreeCAD` the spheres can be swelled to a desired goal volume fraction, and melded into a single structure using a union operation. This solid structure can then be intersected with a unit cube to remove all material outside the unit domain and thus obtain a periodic SVE. When `PackLSD` generates a packing using periodic walls it will treat any sphere that intersects a wall as already existing on the opposite wall for the sake of volume calculation and collision detection. In the output file none of this periodic geometry will be directly represented and has to be realized as a post-processing step. An efficient way of doing this is to simply copy any sphere that intersects a wall to the opposite side. However, since the intent is to swell the spheres, the fact that spheres may swell across the boundary must be accounted for. To resolve this, one method is to first perform an overkill swelling of the original packing, and use that configuration to detect boundary intersection and copy spheres. A guaranteed overkill swelling is to swell the non-geometrically periodic original sphere packing until it reaches any volume fraction equal to or above goal volume fraction. Since the goal volume is reached before introducing any periodic copies, the swelling for which the truly periodic structure reaches the goal volume will be lower. Once periodic copies have been created, a bisection method can be applied to find the swelling for which the structure reaches the goal volume fraction. Because computing the volume of an overlapping sequence of spheres is a very complex problem, the volume computation is left to `FreeCAD`.

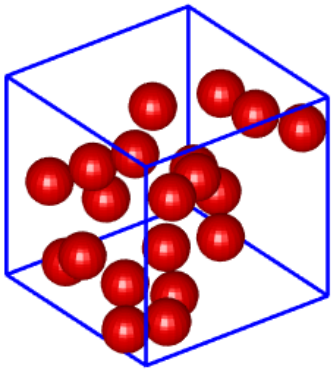

(a) 10% volume fraction.

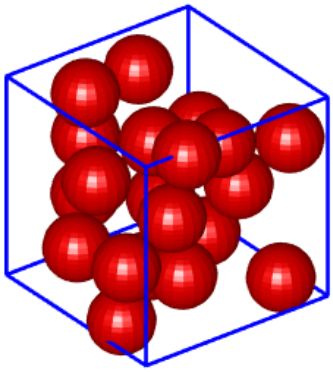

(b) 30% volume fraction.

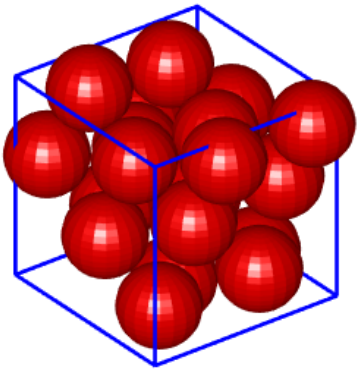

(c) 60% volume fraction.

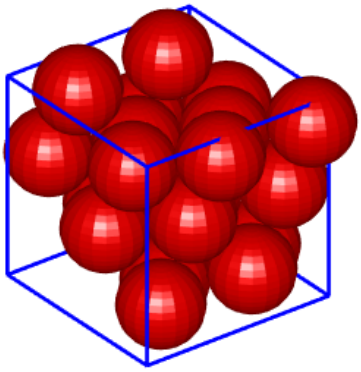

(d) 67.54% volume fraction, where the algorithm could not grow the spheres further.

Figure 3.4: Sphere packing growth over time.

Because the structure needs to be continuous, the lower bound for possible volume fractions is relatively high. Structures below 60% volume fraction tend to have poor continuity, and many spheres will be isolated in the domain. For this reason the sphere structures will not be generated for volumes lower than 60%.

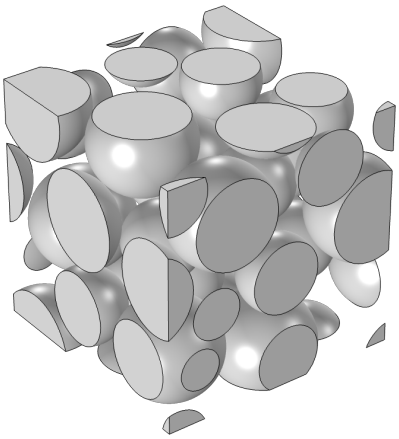

(a) Unswelled sphere packing with periodic copies realized.

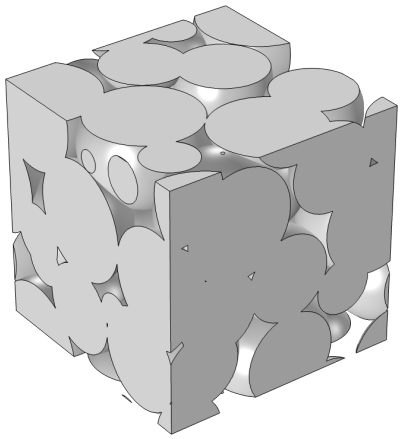

(b) Swelled sphere packing.

Figure 3.5: CAD representation of the sphere packings.

3.3 Voronoi tessellation

The Voronoi tessellation is a spatial partitioning of a domain into n cells V_j based around n spatially distributed points $\boldsymbol{p}_j$ called *seeds* [18]. The tessellation is defined such that for a given cell j, the distance between the seed j and every point in space is equidistant or less than the distance to any other seed k. Formally this may be defined as:

$$V_j = \{\boldsymbol{x} \in \Omega \mid d(\boldsymbol{x}, \boldsymbol{p}_j) \leq d(\boldsymbol{x}, \boldsymbol{p}_k) \; \forall \; j \neq k\} \tag{3.10}$$

Where the operator $d(\bullet, \bullet)$ is the euclidean distance, which in this case is limited to three dimensional space:

$$d(\boldsymbol{x}, \boldsymbol{y}) = \sqrt{(x_1 - y_1)^2 + (x_2 - y_2)^2 + (x_3 - y_3)^2} \tag{3.11}$$

Voronoi tessellations have successfully used to generate artificial microstructures in previous research [19][20], both as a structure and as a basis.

In this project, a damage phase field equation [21] is applied to the edges of the Voronoi tessellation and used to generate a structure based on the damage variable. The open source library `Voro++` [22] can used to generate Voronoi tessellations, given the seed coordinates as input data. The seed coordinates are generated as points with a random function in `MATLAB` with uniform distribution. To ensure that the points are not generated too close to each other a simple conditional statement is added that does not allow points to be generated within the distance $1/n$ of other seeds. In typical cases the Voronoi tessellations are defined within a domain with hard wall boundaries In the context of computational homogenization the microstructure needs to be periodic. `Voro++` enables the generation of periodic tessellations with a few caveats. The output cells from `Voro++` are defined per seed and do not by themselves realize the periodicity within the defined domain, this needs to be done in post-processing. Since the Voronoi cells are stored in a simple matrix data structure, it is not costly to apply a brute force periodicity method and simply repeat the tessellation 3x3x3 times. After the cells are repeated to realize the periodicity they must be truncated to be contained within the cube domain. Any Voronoi edge that intersects any of the cube planes is truncated at the point of intersection, see Figure 3.6 for an illustration the process in 2D and Figure 3.7 for 3D.

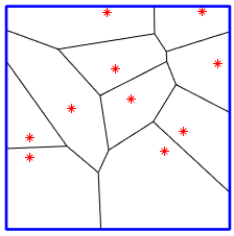

(a) Voronoi tessellation with hard wall boundaries.

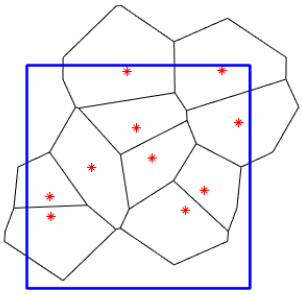

(b) Voronoi tessellation with periodic boundaries.

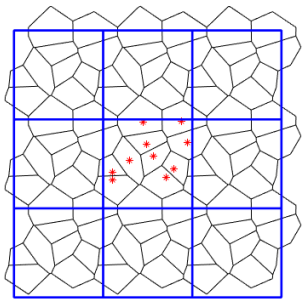

(c) Voronoi tessellation with periodic boundaries and repeated cells.

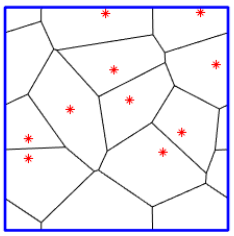

(d) Voronoi tessellation with periodic boundaries and truncated repeated cells.

Figure 3.6: Voronoi tessellations in 2D illustrating the different boundary conditions and their effects.

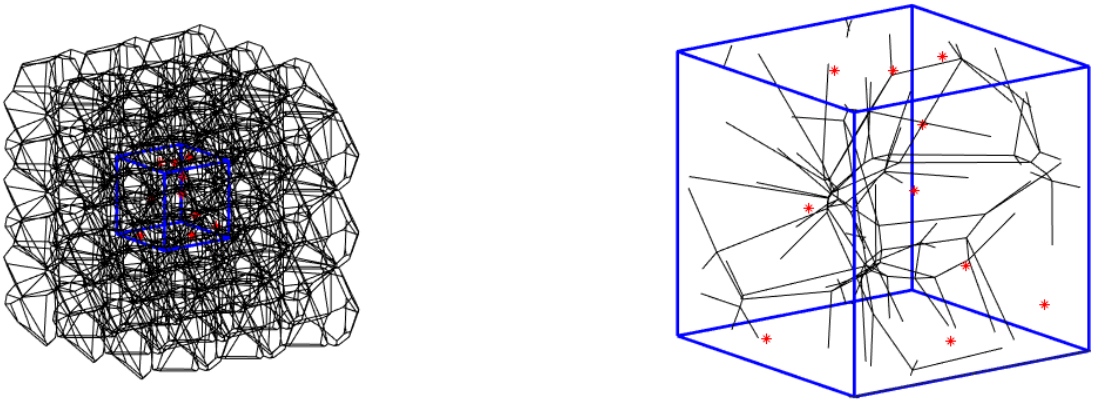

(a) Voronoi tessellation in 3D with brute periodicity.

(b) Voronoi tessellation in 3D with truncated edges.

Figure 3.7: Voronoi tessellation in 3D.

The data structure of the tessellation after truncation is simply a list of pairs of coordinates that define lines in space. A crucial stage in the post-processing is cleaning up the tessellation from coinciding edges. As a result of the brute copying, as well as the cell-wise structure of the original output format, there will always exist redundant edges. These must be removed, otherwise the extra edges will provide additional contributions to the applied equation.

The truncated Voronoi cells can then be imported into `COMSOL`. By solving a second order diffusion equation in form of the damage phase field equation with essential boundary conditions on the Voronoi edges and SPBC along the boundaries, a periodic continuous trabecular structure can be generated by applying an element filter to the dependent variable the same way as for the Cahn-Hilliard structure. Just like for the Cahn-Hilliard structures, the damage equation needs to be solved with periodic boundary conditions in order to obtain a completely periodic structure. So once again, SPBCs are considered. The damage phase variable is now introduced:

$$d \triangleq d(\boldsymbol{x}) \in [0, 1], \tag{3.12}$$

where 0 is undamaged material and 1 is fully damaged.

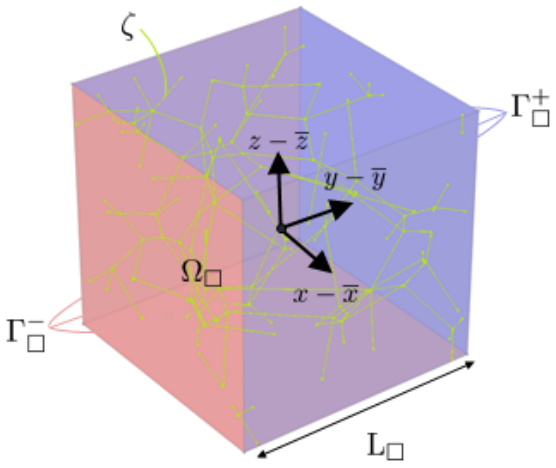

Figure 3.8: Truncated Voronoi cells embedded in a cubic domain.

Considering the cubic domain $\Omega_\square$ with boundaries $\Gamma_\square$ and Voronoi edges ζ shown in Figure 3.8, it follows that the strong format of the damage equation with SPBCs along the boundaries and essential conditions for the

Voronoi edges can be defined according to:

$$\begin{aligned} d + \mathbf{f} \cdot \boldsymbol{\nabla} = 0 \quad & \text{in} \quad \Omega_{\square}, \\ [\![d]\!]_{\square} = 0 \quad & \text{on} \quad \Gamma^{+}_{\square}, \\ f(\boldsymbol{x}) = -f(\varphi_{\text{per}}(\boldsymbol{x})) \quad & \text{on} \quad \Gamma^{+}_{\square}, \\ d = d_p \quad & \text{on} \quad \zeta, \end{aligned} \tag{3.13}$$

where the constitutive relations are governed by:

$$\begin{aligned} \mathbf{f} &= -\gamma^2 \boldsymbol{\nabla} d, \\ f &\triangleq \mathbf{f} \cdot \boldsymbol{n}, \end{aligned} \tag{3.14}$$

in which γ is a length scale parameter.

The weak format is now derived by defining an arbitrary test function δd which is multiplied with the strong format in Equation 3.13 and then integrated over the domain. Applying partial integration and subsequently Gauss's divergence theorem while noting that the boundary flux term vanishes due to the SPBCs with the same motivation as for Equation 2.58, the weak format can be obtained for the damage equation:

Find $d \in \mathbb{D}$ such that:

$$a^{(d)}(d, \delta d) + b(d, \delta d) = 0 \quad \forall \delta \mu \in \mathbb{D}^0, \tag{3.15}$$

where the variational forms were introduced:

$$\begin{aligned} a^{(d)}(\bullet, \bullet) &\triangleq \int_{\Omega_{\square}} \gamma^2 \nabla \bullet \cdot \nabla \bullet \ \mathrm{d}\Omega, \\ b(\bullet, \bullet) &\triangleq \int_{\Omega_{\square}} \bullet \bullet \ \mathrm{d}\Omega, \end{aligned} \tag{3.16}$$

together with the function space:

$$\mathbb{D} \triangleq \left\{ d \in \mathbb{H}^1(\Omega_{\square}) |\ [\![d]\!]_{\square} = 0 \text{ on } \Gamma^{+}_{\square} |\ d = d_p \text{ on } \zeta \right\}. \tag{3.17}$$

The weak format in Equation 3.17 is implemented in `COMSOL` for the cubic domain in Figure 3.8 with arbitrary values of γ and d_p. Unlike the Cahn-Hilliard equation, there does not exist any intuitive value for the phase variable threshold d which results in a specific volume fraction. Therefore, the damage value for which a specific volume fraction is obtained needs to be found iteratively. Since `COMSOL` can simply compute the volume occupied by the filtered domain through integration, this value is easily found through a bisection algorithm. There is no physical reasoning for the choice of solid domain. Hence, the solid domain is chosen as the elements with a damage value above the threshold, and porous domain as the elements with a damage value below the threshold. Figure 3.9 shows the solution of a Voronoi sample together with the filtered solid domain.

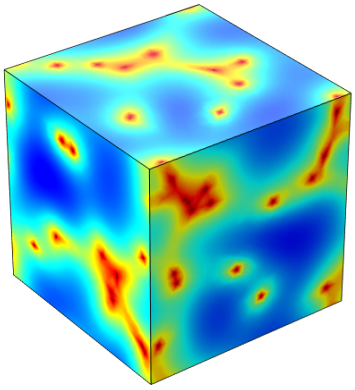

(a) Damage phase solution.

(b) Damage phase solution after applying the element filter for a 50% volume fraction.

Figure 3.9: Damage phase solution showing in the cubic domain and a domain after element filtering.

The filter is exported as a surface mesh, and then following the same methodology as for the Cahn-Hilliard structures, two STEP files are generated.

3.4 Convex Hulls

A convex hull is a polytope defined as the subset P of points in a set S that form the vertices of the convex set that contains S [23]. Which means that for a given set of points in three dimensions, the convex hull is the smallest structure that contains all the points. In 2D a convex hull is represented by vertices and edges, in 3D the edges are replaced by triangular facets, see Figure 3.10.

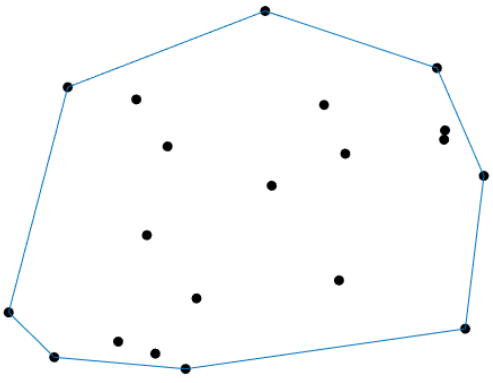

(a) A convex hull in 2D.

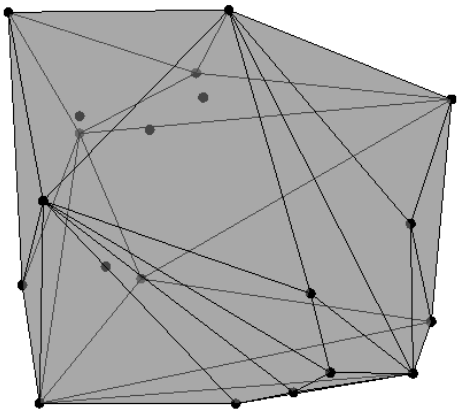

(b) A convex hull in 3D.

Figure 3.10: Convex hull illustrations.

A series of convex hulls can be computed to create a stochastically generated microstructure with simple topology. This approach is conceptually inspired by an approach to generate microstructures that uses spherical harmonics to create distorted spheres and a connectivity network to prescribe which spheres will be connected [24]. The approach used in this project is instead to generate a distribution of spheres with the Lubachevsky-Stillinger algorithm as a basis for a structure, and then generate a Voronoi tessellation with the sphere centers as seeds.

The advantage of using a sphere packing algorithm for seed distribution is that it results in a random spatial distribution of points that will indirectly enforce a minimum distance criterion as a result of the spheres being disallowed to overlap. Within each Voronoi cell one can then generate a number of points from which a convex hull can be computed. By constructing a connectivity network between the sphere centers and then inserting points that overlap the Voronoi cells of connected spheres, the convex hulls will intersect each other to represent connectivity.

To compute a convex hull, the built-in `MATLAB` function `convhull` will be used for this project. It is not documented how `MATLAB` computes a convex hull, in its stead a brief pseudocode method is presented in algorithm 1. For a more detailed explanation see [23].

Algorithm 1: Example convex hull algorithm.

Input: Set of points S;
Find four points $p_1, p_2, p_3, p_4 \in S$ that form a tetrahedron which becomes the convex hull CH;
For each facet of CH, maintain a set of points P_C that can "see" a facet;
For all remaining points, maintain a set of facets F_C seen by remaining points;
while *There are still uncontained points which can see facets of CH* **do**
  for r = *5:n, where n is the number of points in* S **do**
    Insert p_r into CH;
    if *there is an entry for* p_r *in* F_C **then**
      Remove all facets visible by p_r;
      for *Horizon edges e of removed facets* **do**
        Create new facet f_{re} from e and p_r;
        for *all points* $p_t = P_C(f_{e1}) \cup P_C(f_{e2})$ *that could see the removed facets which were connected to e* **do**
          Check if p_t can see f_{re}, if so add to F_C;
        end
      end
    end
  end
end
return CH, *a triangulation whose vertices are the subset* P

Remark: The idea of whether a facet is "seen" by a point can be determined by checking if a point lies within the open half-space formed by a facet. By convexity, the convex hull the facet belongs to must be contained within either of the half-spaces. Therefore a point that can see a facet must lie in the opposite half-space. See Figure 3.11, where the marked facets are seen by the point.

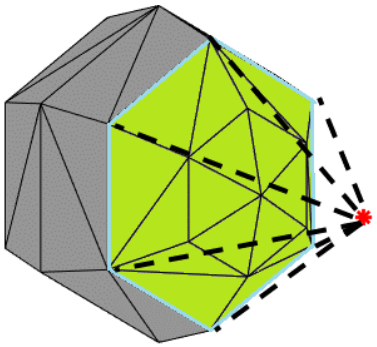

Figure 3.11: Illustration of a convex hull and a not yet contained point. Green facets are seen by the point, blue outline shows the horizon edges seen by the point.

The process begins by generating spheres in a unit cube domain using the Lubachevsky-Stillinger algorithm, where the chosen stopping criteria is a relatively small volume fraction around the range of 0.3-0.5. The volume fraction of the sphere packing will dictate how uniform the Voronoi tessellation ends up. For densely packed spheres of a higher volume fraction, the distance between neighboring spheres will be roughly the same in the entire domain, which will result in very homogeneous Voronoi cells, see Figure 3.12. This is not necessarily a negative quality, but for this project the more stochastic and non-uniform tessellation was chosen instead.

(a) Voronoi tessellation from a sphere packing volume of 70%.

(b) Voronoi tessellation from a sphere packing volume of 30%.

Figure 3.12: Examples of uniform and non-uniform tessellations.

As discussed in previous sections, the periodic crossing of the spheres and the Voronoi cells is not present in the base representation. Since the idea is to generate particles inside the cells and enforce connectivity through a predetermined network, periodicity cannot be realized through copying the convex hull particles *a posteriori*. Instead the geometric periodicity is enforced by copying any Voronoi cell which intersects the unit cube. This is necessary, since otherwise, a recursive algorithm would be required to redo the periodic copying and connectivity network if a particle happens to be generated that intersects the boundary. Copying all intersecting cells is a slight overkill method, but considerably simpler. Checking if any edge or vertex in an arbitrary polytope intersects a cube is not a completely trivial operation. A brute method is to generate a dense point cloud that forms a hollow unit cube, see Figure 3.13. By computing a temporary convex hull using the Voronoi cell vertices, one can then check if the cube points intersect the cell using a function [25]. The point cloud only needs to be generated once and can thereafter be stored and read from a file.

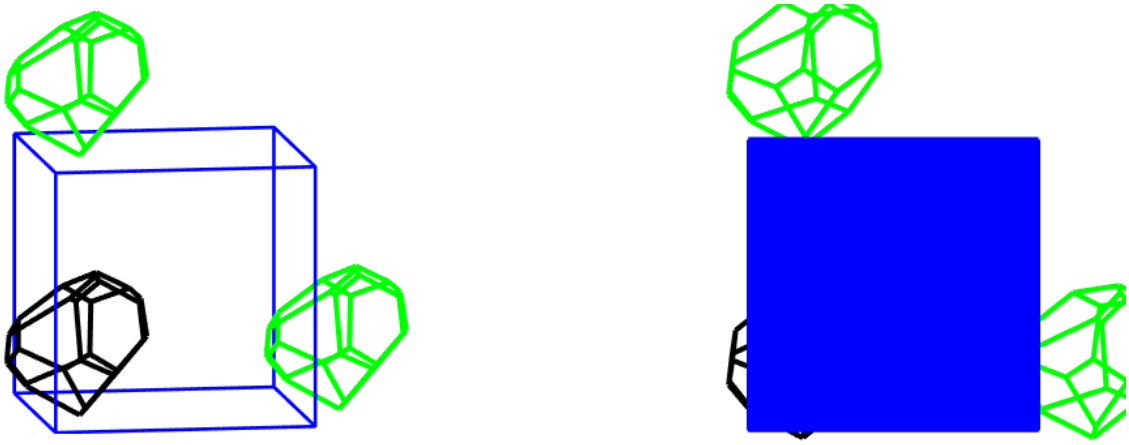

(a) Periodic cell copies.

(b) Periodic cell copies with hollow cube point cloud.

Figure 3.13: Examples of periodic copying with the point cloud method.

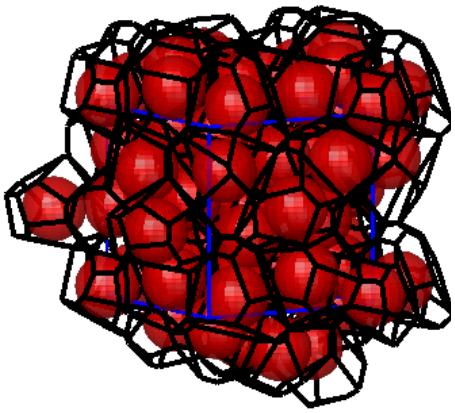

Figure 3.14: Fully realized periodic cells and spheres.

With the cell periodicity realized, the connectivity network can be constructed using graph theory. The method used in the previously cited spherical harmonics structures is to generate a graph matrix where each pair of indices i, j refers to the distance between the surfaces of spheres i and j. One algorithm to generate a network from a graph matrix is a minimum spanning tree [26], which computes the network of shortest total length that includes all nodes. To achieve a more natural looking network, the graph matrix is modified such that each sphere only retains its five closest neighbors as connections in the distance graph, all other nodes are considered disconnected and are disallowed as possible routes in the network algorithm. However, since the closest five nodes is not necessarily a symmetric quality the graph matrix is adjusted to be symmetric, which may give a node more than five potential connections. From this adjusted graph matrix the minimum spanning tree algorithm returns a list of node pair indices that are connected, see Figure 3.15 for an illustrated network. Since all Voronoi cells are included in this network, full geometric continuity is assured.

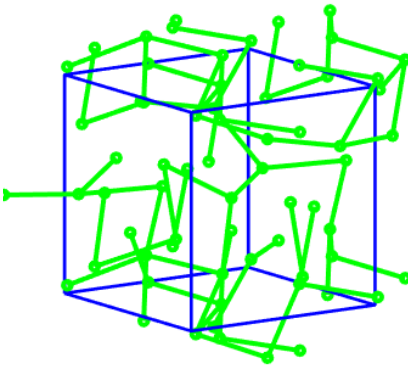

(a) Connectivity network.

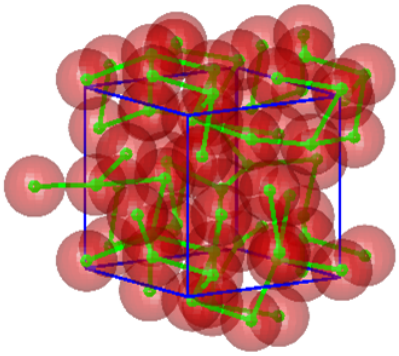

(b) Connectivity network with periodic sphere packing.

Figure 3.15: Example of the connectivity network.

With the cells finalized and connectivity computed, the convex hull particles can be constructed. Inside each Voronoi cell a number of points are generated with uniform distribution. Each coordinate is bounded by the extrema of the Voronoi cell to limit the range of possible positions to avoid generating a large number of invalid points. This means that the generation range of x-coordinates are bounded by the maximum and minimum x-coordinate values of the Voronoi cell, with similar restrictions for the y- and z-coordinates. Once this initial point cloud is generated, the connectivity is realized by inserting a point inside the cells which the currently treated cell is connected to, where the "connectivity depth" becomes a generation parameter, see Figure 3.16. To guarantee structural periodicity, the particle belonging to one Voronoi cell must be identical to that of a periodic copy of the cell. Before the particle can be copied, the connectivity of each copy needs to be mirrored onto the source. By identifying the offset of a copy from its source, the connections to that copy can be reflected onto the

source by reflecting the connection with the reverse offset, see the simple example in Figure 3.16b. After all these steps are completed, a convex hull is computed from the points, and the process is repeated for all source cells. Finally, all copied cells have the convex hull from their source copied into them. This scheme guarantees a continuous and periodic structure.

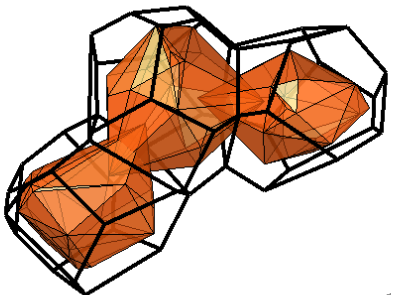

(a) Convex hull with connectivity to two convex hulls

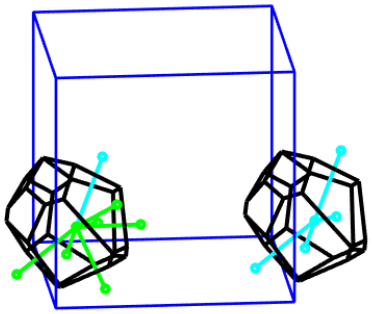

(b) Green lines illustrate connections of source particle. Cyan lines illustrate connections of the periodic copy. One cyan connection is mirrored back onto the source.

Figure 3.16: Illustration of how connectivity is built.

The volume of each particle has a strong correlation to the number of points used to generate the convex hull. In order to allow some degree of control over the final structure volume, the point cloud is further restricted to the space between two scaled copies of the Voronoi cell, see Figure 3.17. Since the periodic Voronoi tessellation will cover the entire volume of the domain, the total Voronoi cell volume will always be one. By forcing the point cloud to be generated between two scaled cells, the volume of the convex hull relative to its cell is roughly between the volumes of the two boundary cells, depending on the number of points. Additionally, the connections will contribute to the structure volume by an unpredictable amount, so while this strategy allows for some degree of control over the structure volume, it will fail at lower volumes. The scaling factors of each of these cells becomes another generation parameter.

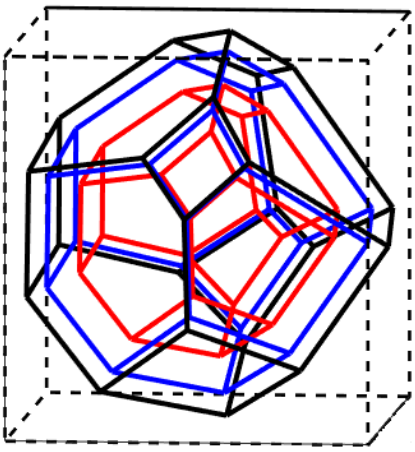

(a) Voronoi cell with bounding cells and box.

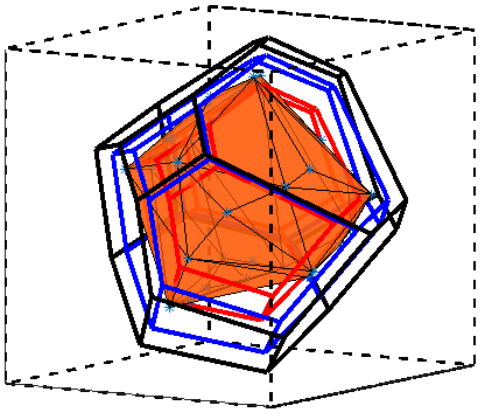

(b) Convex hull generated inside bounding cells.

Figure 3.17: Illustration of Voronoi cell and bounds.

The convex hulls are as previously touched upon stored as triangulations. The triangles define the surface of each convex hull, and they will intersect the surface of connected particles. The triangulation is exported as an

STL mesh and then imported into `FreeCAD`. In `FreeCAD` the triangulation is read and split into separate mesh objects for each convex hull. Each convex hull is converted into a solid object and a union operation is called to create one solid structure. This removes the intersecting connectivity and instead results in a continuous solid connection. To finalize the structure as a volume element, a unit cube is created and the intersection between the convex hull structure and the cube is taken and exported as a STEP file, which is shown in Figure 3.18b. The generation process is presented in algorithm 2:

Algorithm 2: Convex hull microstructure generation

```
Generate sphere packing with PackLSD;
Generate Voronoi tessellation around spheres;
Copy spheres and Voronoi cells across boundaries based on cell intersections;
for All source spheres do
    Scale Voronoi cell to create outer and inner boundaries;
    Generate points inside boundary cells;
    for All connections do
        Generate point inside cell of connected sphere;
    end
    for All copies of source sphere do
        for All connections of copied sphere do
            Mirror connection onto source sphere by generating point inside connected cell of connected
             sphere and subtracting the offset of the copied sphere
        end
    end
    Compute convex hull;
    for All copies of source sphere do
        Generate the same convex hull as for the source sphere inside the copied cell;
    end
end
Export all convex hulls as a single STL file;
Load STL file as mesh in FreeCAD;
Split intersecting mesh objects and convert them to solid parts;
Perform union operation on all solid convex hull parts;
Perform intersection operation on solid convex hull union and a unit cube;
Export STEP file;
```

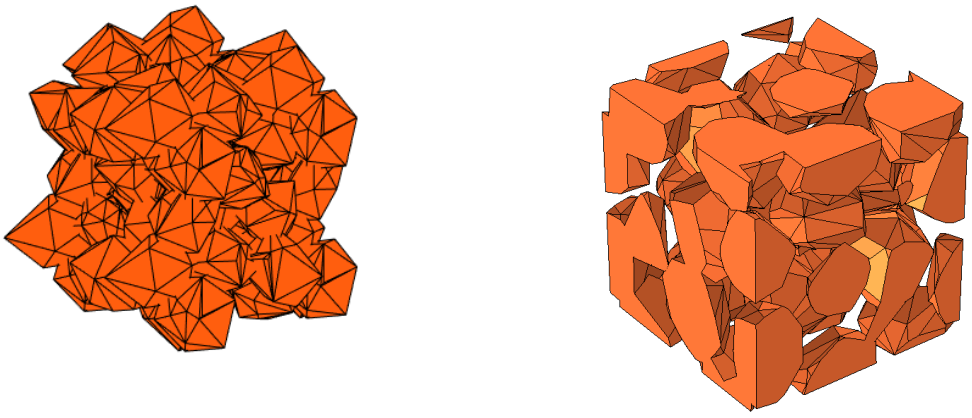

(a) Generated set of convex hulls.

(b) Convex hull structure in CAD format.

Figure 3.18: Convex hull representations.

3.4.1 Convex hull particles with binder material

Another potential use for the presented convex hull structures is to model the microstructure of the positive structural battery electrode. By coating a carbon fiber with a mixture of lithium-metal-oxide particles and a binder additive, the fiber can function as a structural positive electrode [27]. By labeling the intersecting connections of the convex hull structures "particle-to-particle" connections, one can then choose to define some of the connections as "binder" connections. The choice of method to define the connection types becomes a structure parameter. For this project, the parameter is chosen such that all connection longer than the median distance of all connections are set to binder connections.

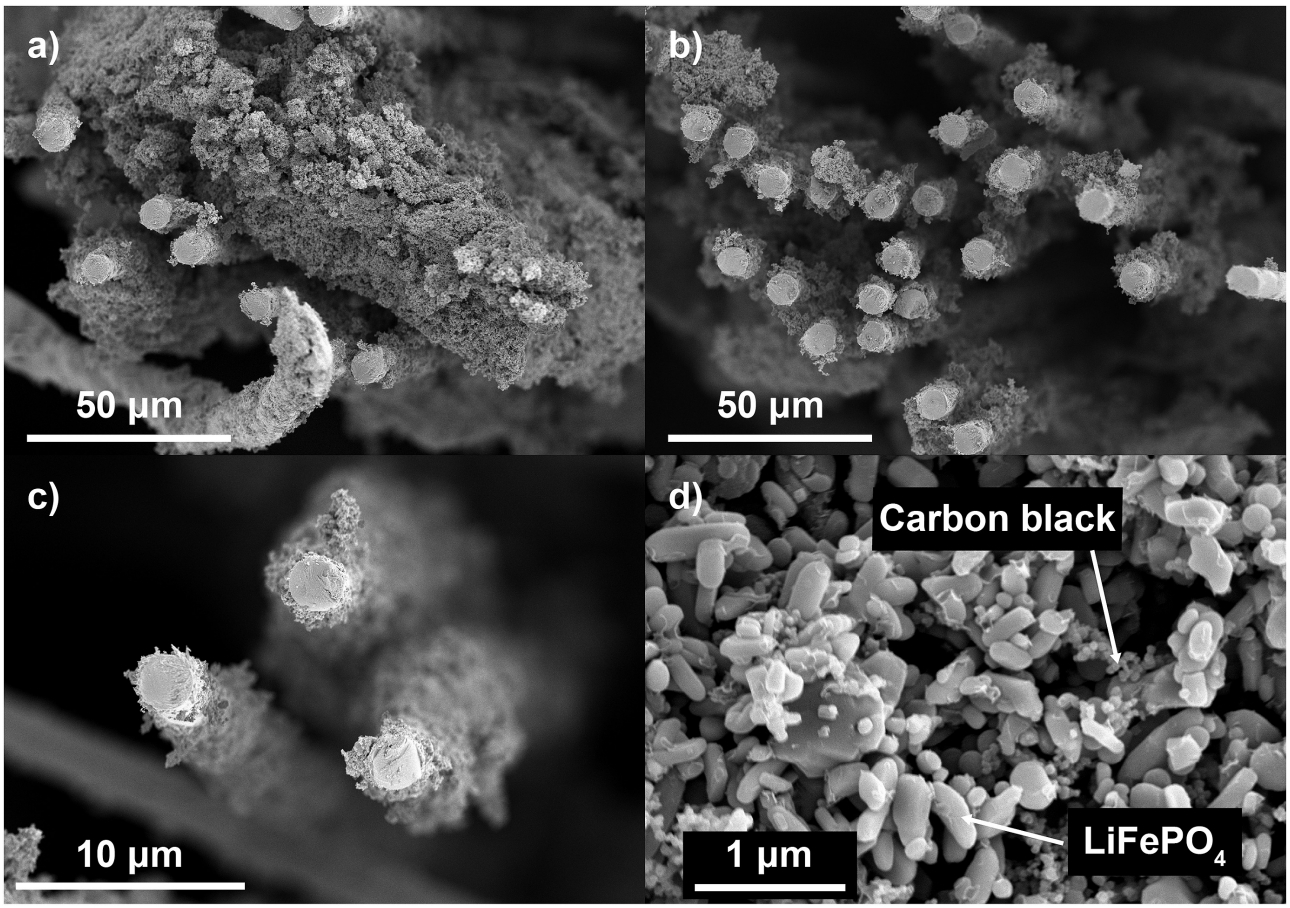

Figure 3.19: Cross-section and high magnification SEM images of coated carbon fibers. Excessive coating is seen in a) and a homogeneous coating in b) and c), d) reveals well dispersed lithium iron phosphate and carbon black particles. Images reproduced with the permission of Johanna Xu [27].

In the generation process described in the previous section, the only changes before finalization are labeling the connections, and skipping the binder connections. The incomplete convex hull structure is processed and turned into a STEP file like before. Then to generate the binders, the binder connectivity network is reformatted to describe which spatial points are connected as opposed to which sphere indices. To enforce periodicity, the same treatment of connectivity in regards to periodic copies from the previous section is necessary. Any connections from a periodic copy is mirrored onto its source. After the connectivity is rewritten and processed, the binder material is realized by using `FreeCAD` to generate cylinders, where the bases are centered on the sphere centers. The cylinders are subjected to a union operation, followed by an intersection operation with a unit cube similarly to the convex hull structure. To enable the binder structure and convex hull structures to function together, a difference operation is applied where the convex hull structure is cut away from the binder structure, see Figure 3.20. By performing this cut, the two structures can be imported into `COMSOL` where they will be perfectly connected as shown in Figure 3.21. Since the two structures are considered separate objects in `COMSOL` they can be assigned different properties, a feature that would otherwise be impossible or tricky to achieve, especially in an automated workflow.

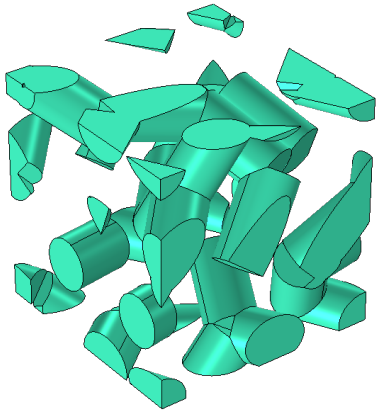

(a) Binder cylinders intersected with unit cube.

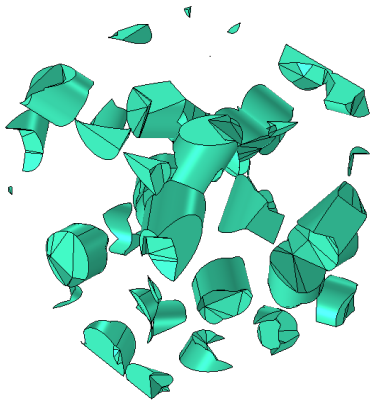

(b) Binder cylinders cut with convex hull structure.

Figure 3.20: Binders geometry.

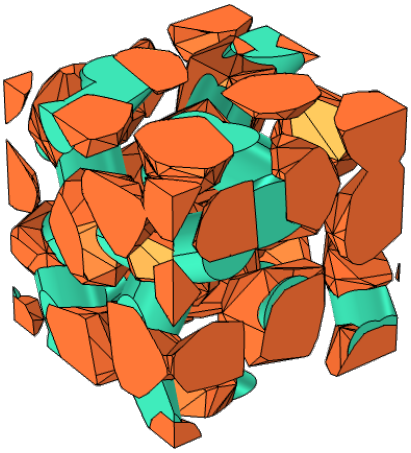

(a) Convex hull with binders structure. Particles are colored orange, binders green.

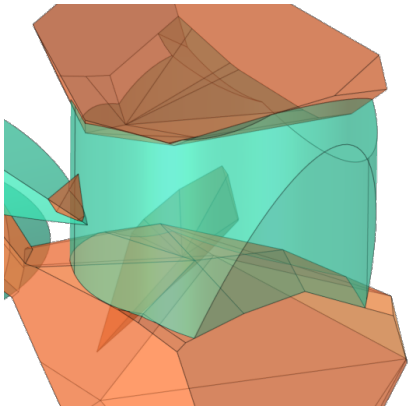

(b) Translucent image of a binder connection. Particles are connected to binder without intersection.

Figure 3.21: Convex hull with binders.

A few comments must be made on this generation scheme. The radius of the cylinder is for this project left as a generation parameter. Ideally the cylinder radius should be a property that is algorithmically determined by some other quantity. The cylinders are centered on the centers of the spheres used for the Voronoi tessellation. This decision was arbitrary, and could be changed to either the cell centers or the convex hull centers. Using the sphere centers results in the property of the binders not necessarily being centered on the convex hull particles. Additionally, the binder cylinders may very well overlap and intersect. A rare situation where a particle-to-particle and binder connection overlap may occur as a result of the periodic mirroring. Due to the difference operation applied to the binder structure this effectively results in a particle-to-particle connection with a hollow binder that covers the connection. This property was only observed only very few times, and was not deemed to be significant enough to warrant consideration.

Immediately generating a periodic mesh in `COMSOL` for the binder geometry turns out to be very unreliable, with approximately 5% of the structures being successfully meshed. One of the key factors that are causing `COMSOL's` mesh routine to fail is its inability to handle aperiodicity of the seams of the cylinders. The seams are the lines that run along the length of the cylinders, and are present on most cylindrical CAD representations, see Figures 3.20 and 3.21. The cause seems to be that `COMSOL` must include the vertices of these seams as vertices in the mesh. So if one boundary face or edge has a seam intersecting the boundary and the opposite does not, `COMSOL` cannot produce a periodic mesh. The `COMSOL` geometry module offers an "ignore edges" feature that can be

applied to ignore the seams and their vertices which raises the success rate to roughly 40-50%. Because the structures are intended to be generated and analyzed in a fully automated fashion, this process too needs to be automated. A simple but reliable routine is developed which checks all edges in the imported binder object and compares the normalized vector between the edge's vertices to those of the binder network. Any edge that has the same direction as a binder connection, and no curvature, is most likely a cylinder seam, and can be marked as an ignored edge. Because every edge is checked against every connection this seam identification routine is rather slow, and takes roughly as much time to complete as it takes to generate the STEP file from routine initiation. The significant improvement in mesh success rate effectively results in an improvement to computation times.

3.5 Passivation layer

A passivation layer known as the solid electrolyte interphaseis (SEI) is formed along the negative carbon fiber electrode from decomposition of electrolyte. This layer is electrically insulating but allows for Li-ion transport. The SEI is crucial for the battery's lifetime since it blocks electrons to prevent further electrolyte decomposition and allows the electrode to operate within its stability range [28]. Clearly, the SEI layer is fundamental for protecting the electrode during operation. However, during fiber extension, crack growth along the interface results in delamination of this protective film. The properties of the layer may also affect the mechanical behavior of the battery.

In this project the delamination of the passivation layer is studied using computational homogenization. Here, The passivation layer is modeled in `COMSOL` using the inbuilt solid mechanics module. The study is mainly conducted for a 2D subscale domain where the computational domain is denoted as a statistical area element (SAE). One 3D sample is solved but only to verify solvability. The reasoning for investigating a 2D domain instead of 3D one is mainly due to the increased computational costs arising from considering an extra dimension. The Cahn-Hilliard equation is used for modeling the SAE since the generation for 2D is similar to 3D and does not require any external tools more than the `COMSOL-MATLAB` API. Due to a lack of available parameter data, all parameters are chosen arbitrarily. It should be mentioned that the modeling presented serves as a toolbox which input parameters can be modified when adequate data becomes accessible.

An SAE is generated by applying the Cahn-Hilliard equation in Equation 3.7 for a square domain with SPBCs. Once again, after specifying parameters for the structure generation, the weak format in Equation 3.7 is solved in `COMSOL`. Similar to the 3D case, a filter is created to export two surface meshes, one for each phase. However, the 2D mesh does not require further modification and the filtered meshes can directly be used for FEA. Both exported meshes are used to model the fiber-passivation interface. The passivation layer is modeled by partitioning the porous domain to only include part of its thickness t_p, where the thickness is defined as the normal distance away from the adjacent fiber. The thickness of the passivation layer is arbitrarily set to one tenth of the SAE side length, this way the passivation layer will have a thickness similar to the diameters of the pore channels. Figure 3.22 shows a generated SAE of the Cahn-Hilliard equation with domain $\Omega_\square$, side length $L_\square$, and external boundaries $\Gamma_{\square,F} \cup \Gamma_{\square,D} \cup \Gamma_\square^- \cup \Gamma_\square^+$ where $\Gamma_{\square,F}$ corresponds to the fiber boundary. The solid domain is denoted Ω_s, the passivation layer Ω_p, and the interface boundaries Γ_{int}.

To establish the interface between the passivation layer and solid domain, an assembly is constructed between the imported geometries such that contact nodes along the interface boundaries are detected. It is required to define a contact formulation according to the penalty method to model adhesion in `COMSOL` [29]. Essentially, the penalty method splits the assembly into a source and destination part, where the source part corresponds to the solid domain and the destination part to the passivation layer, and inserts a spring between the two boundaries. This spring will make it so that only slight penetration is allowed between the two boundaries when they are in contact. The force from the spring is computed as the product of the gap between the surfaces $g(\boldsymbol{x})$ and a penalty stiffness ϵ, which is chosen automatically by `COMSOL` to be equal to the stiffness of the destination boundary. Even though this penalty stiffness may seem low, the contact formulation is not of importance for the delamination process. It should also, once again, be made clear that project models a toolbox which input can be changed and that this study does not consider physical correct material parameters.

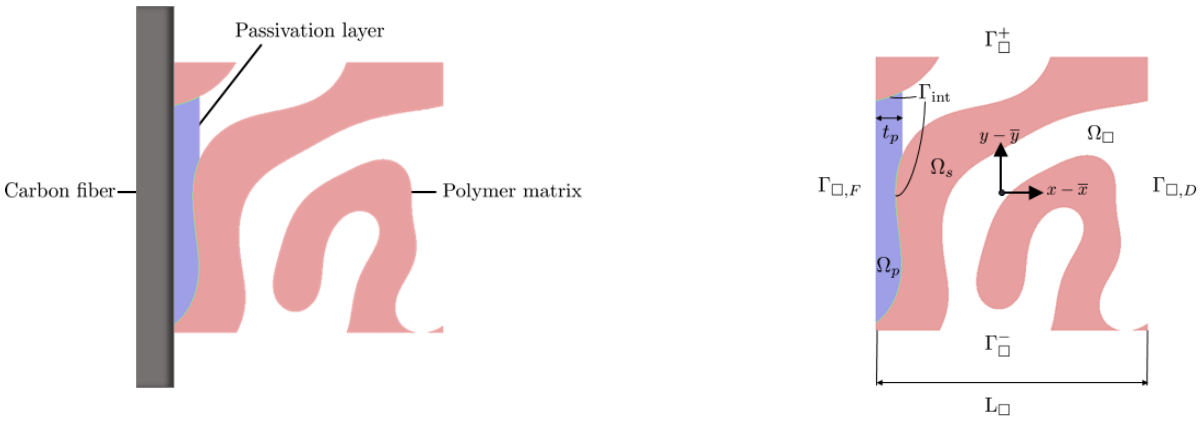

(a) Matrix attached to carbon fiber with passivation layer.

(b) SAE with passivation layer for a 50% solid phase.

Figure 3.22: Illustration of the domain pertinent to the interface problem.

For the initial configuration it is presumed that the passivation layer and solid domain are completely attached to each other. Hence, an adhesion law is used between the interface of the source and destination boundaries. Essentially, adhesion means that a thin elastic layer is placed between the two boundaries. Here, adhesion is chosen to always be active so that the boundaries are bonded unless broken by a damage criterion. `COMSOL` connects the two surfaces by defining an adhesive stress vector $\boldsymbol{f}_{\text{a}}$:

$$\boldsymbol{f}_{\text{a}} = \boldsymbol{k} \cdot \boldsymbol{u}(\boldsymbol{x}) \triangleq \boldsymbol{k} \cdot \boldsymbol{u}, \tag{3.18}$$

where $\boldsymbol{k}$ is the adhesive stiffness vector, and $\boldsymbol{u}$ the displacement jump vector which is evaluated in terms of the gap and relative slip between the two boundaries. Essentially, the jump vector can be viewed as the displacements between points located on the source and destination boundaries. The stiffness vector contains a stiffness in the tensile direction, which by default is set to the penalty stiffness ϵ, and tangential contributions computed as the product of the tensile stiffness and a coefficient η_τ. In 3D the vector is evaluated according to:

$$\boldsymbol{k} = \begin{bmatrix} \eta_\tau \epsilon & \eta_\tau \epsilon & \epsilon \end{bmatrix}^T, \tag{3.19}$$

where η_τ is a unknown material parameter which in this project is chosen arbitrarily as `COMSOL's` default value. It should be mentioned that the normal contribution in the stress vector equals zero when the gap between the boundaries is smaller than zero. As a result the constraint is then resolved by the penalty formulation.

A decohesion formulation is implemented to break the bond between the two boundaries when the structure is deformed. In `COMSOL` the decohesion criteria is based on a scalar interface damage where energy is released over a process zone resulting in progressive delamination. The adhesive stress vector in Equation 3.18 is then modified to include the interface damage d according to:

$$\boldsymbol{f}_{\text{a}} = (1-d)\boldsymbol{k} \cdot \boldsymbol{u}, \tag{3.20}$$

from which it is observed that complete decohesion corresponds to a damage value equal to unity. The standard decohesion law of displacement based damage is considered. The fracture is computed as a combination of tensile and shear mode contributions for which `COMSOL` defines a mixed mode displacement u_m, computed as the norm of the displacement jump:

$$u_{\text{m}} = ||\boldsymbol{u}(\boldsymbol{x})||. \tag{3.21}$$

Furthermore, the damage is tracked using the largest value of u_{m} during the load history:

$$u_{\text{m,max}} = \max(u_{\text{m}}(t)), \quad \forall t \in \begin{bmatrix} 0, & \tau \end{bmatrix}, \tag{3.22}$$

where t is the time variable of the evolution and τ the end time of a current load history. A simple linear separation law is considered in `COMSOL` for the decohesion problem such that the damage variables can be

evaluated according to:

$$d = \begin{cases} 0 & \text{if} \quad u_{\mathrm{m,maxm}} < u_{0\mathrm{m}} \\ \dfrac{u_{\mathrm{fm}}}{u_{\mathrm{m,max}}} \left(\dfrac{u_{\mathrm{m,max}} - u_{0\mathrm{m}}}{u_{\mathrm{fm}} - u_{0\mathrm{m}}} \right) & \text{if} \quad u_{\mathrm{m,maxm}} \geq u_{0\mathrm{m}} \end{cases} \tag{3.23}$$

where u_{0m} denotes the initiation of mixed mode damage and u_{fm} the point of complete fracture. The initiation damage u_{0m} is calculated according to:

$$u_{0m} = u_{0t} u_{0s} \sqrt{\frac{u_m^2}{\langle u_{\mathrm{I}} \rangle^2 u_{0s}^2 + u_{\mathrm{II}}^2 u_{0t}^2}}, \tag{3.24}$$

in which u_{I} corresponds to the tensile contribution in the displacement vector, u_{II} to the tangential portion in the displacement vector. Also, the Macaulay brackets were used which are defined as:

$$\langle \bullet \rangle = \begin{cases} 0 & \text{if} \quad \bullet < 0 \\ \bullet & \text{if} \quad \bullet \geq 0 \end{cases} \tag{3.25}$$

The constants u_{0t} and u_{0s} are evaluated according to:

$$\begin{aligned} u_{0\mathrm{t}} &= \frac{\sigma_{\mathrm{t}}}{k_{\mathrm{n}}}, \\ u_{0\mathrm{s}} &= \frac{\sigma_{\mathrm{s}}}{k_{\mathrm{t}}}, \end{aligned} \tag{3.26}$$

where σ_{t} is the tensile strength for the adhesion layer, σ_{t} the shear strength, k_{n} the tensile contribution of the adhesive stress vector, and k_{t} the tangential contribution of the adhesive stress vector. The point of complete fracture depends on a power law defined as:

$$\left(\frac{G_{\mathrm{I}}}{G_{\mathrm{Ic}}} \right)^{\alpha} + \left(\frac{G_{\mathrm{II}}}{G_{\mathrm{IIc}}} \right)^{\alpha} = 1, \tag{3.27}$$

where the G_{I} is the energy release rate in tension, G_{II} the energy release rate in shear, G_{Ic} the critical energy release rate in tension, G_{IIc} the critical energy release rate in shear, and α the mixed mode exponent. It follows that the point of complete fracture is computed according to:

$$u_{\mathrm{fm}} = \begin{cases} \dfrac{2\left(1+\beta^2\right)}{u_{0\mathrm{m}}} \left(\left(\dfrac{k_{\mathrm{n}}}{G_{\mathrm{Ic}}} \right)^{\alpha} + \left(\dfrac{\beta^2 k_{\mathrm{t}}}{G_{\mathrm{IIc}}} \right)^{\alpha} \right)^{\frac{-1}{\alpha}} & \text{if} \quad u_{\mathrm{I}} > 0 \\ \dfrac{2G_{\mathrm{IIc}}}{\sigma_{\mathrm{s}}} & \text{if} \quad u_{\mathrm{I}} \leq 0 \end{cases} \tag{3.28}$$

where $\beta \triangleq u_{\mathrm{II}}/u_{\mathrm{I}}$. In addition to the required parameters for the decohesion formulation, it is also necessary to define material parameters for the matrix and passivation layer. In accordance with the homogenization, only linear material models are considered on the subscale. The required material parameters are Young's modulus for the solid domain E_s, Young's modulus for the passivation domain E_p, and Poisson's ratio ν which are chosen as equal for both phases.

To model delamination it becomes necessary to define sufficient boundary conditions for the SAE. It is assumed that the fiber only extends axially during intercalation of Li-ions, where the fiber corresponds to the boundary $\Gamma_{\square,F}$ in Figure 3.22. Here, it is presumed that the vertical strain from the carbon fiber is the main cause behind interface damage evolution. Usually, this fiber extension is approximately equal to one percent [28]. The opposing fiber boundary $\Gamma_{\square,D}$ is fixed in its normal direction and can move freely vertically. To clarify, only one end of the subscale boundary is adjacent to the fiber, the rest of the matrix is assumed to follow the principal of periodicity so that an SAE without the fiber interface connects to Γ_D. The boundary conditions for the top and bottom boundaries are prescribed with SPBCs for the fluctuation field according to first order homogenization.

In summary the boundary conditions are defined according to:

$$\begin{aligned} u_x &= 0 && \text{on} \quad \Gamma_{\square,F}, \\ u_y &= \bar{\epsilon}_{yy} \cdot y && \text{on} \quad \Gamma_{\square,F}, \\ u_x &= 0 && \text{on} \quad \Gamma_{\square,D}, \\ t_y &= 0 && \text{on} \quad \Gamma_{\square,D}, \\ [\![\boldsymbol{u}^{\mu}]\!]_{\square} &= 0 && \text{on} \quad \Gamma_{\square}^{+}, \\ \boldsymbol{t}(\boldsymbol{x}) &= -\boldsymbol{t}\left(\boldsymbol{\varphi}_{\text{per}}\left(\boldsymbol{x}\right)\right) && \text{on} \quad \Gamma_{\square}^{+}. \end{aligned} \tag{3.29}$$

After applying boundary conditions to the SAE, the passivation layer problem can be solved, but first the macroscopic strain $\bar{\epsilon}_{yy}$ needs to be controlled. Here, the strain is ramped linearly until a certain percentage of average interface damage is reached:

$$\overline{d} \triangleq \frac{1}{|\Gamma_{int}|} \int_{\Gamma_{\text{int}}} d \, \mathrm{d}\Gamma. \tag{3.30}$$

This stopping criteria is chosen arbitrarily but tries to correspond to complete delamination. It is chosen so that the solver stops when 90% of the interface is fully damaged. The value of applied strain is then obtained from the stop condition. In practice `COMSOL` requires that adhesion is modeled with geometric nonlinearities, so the applied strain does not actually correspond to the small strain theory in Equation 2.4, but rather to finite strain theory. However, as will be seen later, the stopping criteria will generally activate before such geometric nonlinearities become relevant. Hence, ϵ is still used to denote the applied strain.

The stress level is considered to study the mechanical influence of the SEI layer. Here, the stress component is evaluated for the same direction as the applied strain via Equation 2.1 such that:

$$\overline{\sigma}_{yy} = \langle \sigma_{yy} \rangle_{\square}. \tag{3.31}$$

It is quickly realized that there are multiple unknown parameters affecting the delamination process. Making an extensive parameter study is unreasonable without any available parameter data. For this thesis only the stiffness of the passivation layer is varied since it directly affects the adhesive stress vector. The damage evolution, applied strain, and vertical stress are studied by varying the stiffness of the passivation layer which is chosen as factors k of the solid phase's stiffness. Table 3.1 shows all material parameters used for the modeling.

Table 3.1: Parameters for the passivation layer problem.

Parameter	Value
E_p	200 GPa
E_s	$k \cdot E_p$
k	[0.1, 0.5, 1, 2, 5, 10]
σ_s	80 MPa
σ_t	80 MPa
G_{Ic}	1000 kJ/m^2
G_{IIc}	1000 kJ/m^2
ν	0.3
η_τ	0.17
α	1

The procedure above is scripted for the 2D case using the `COMSOL-MATLAB` API, meaning that the passivation layer problem can be solved in an automated fashion. A single structure is produced and solved as a proof of concept for 3D. The 3D passivation layer is modeled analogously to 2D. All steps above are repeated for the

SVE in Figure 3.23 but by considering the boundary conditions:

$$\begin{aligned}
u_x &= 0 && \text{on} \quad \Gamma_{\square,F}, \\
u_y &= 0 && \text{on} \quad \Gamma_{\square,F}, \\
u_z &= \overline{\epsilon}_{zz} \cdot z && \text{on} \quad \Gamma_{\square,F}, \\
u_y &= 0 && \text{on} \quad \Gamma_{\square,D}, \\
t_x &= 0 && \text{on} \quad \Gamma_{\square,D}, \\
t_z &= 0 && \text{on} \quad \Gamma_{\square,D}, \\
[\![\boldsymbol{u}^{\mu}]\!]_{\square} &= 0 && \text{on} \quad \Gamma_{\square}^{+}, \\
\boldsymbol{t}(\boldsymbol{x}) &= -\boldsymbol{t}\left(\boldsymbol{\varphi}_{\text{per}}\left(\boldsymbol{x}\right)\right) && \text{on} \quad \Gamma_{\square}^{+}.
\end{aligned} \tag{3.32}$$

The same parameters are used as for 2D, but only one ratio k is studied for 3D. A parameter study for 3D was not feasible within the projects time boundaries.

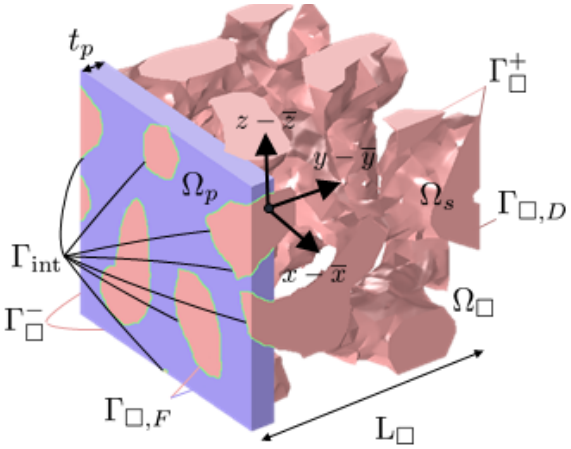

Figure 3.23: Cahn-Hilliard SVE with passivation layer formation for 70% porosity.

4 Numerical studies

Three distinct studies will be performed. The effective properties, as well as the bifunctional performance of each synthetic microstructure will be investigated by using computational homogenization as formulated in chapter 2. For the evaluation of mechanical properties the structures will be interpreted as the solid polymer in the electrolyte. To represent the fluid filled pore space of the electrolyte the structures are inverted through use of Boolean operations in `FreeCAD`. In the case of the convex hull with binder microstructures, since they are intended to represent the electrode coating, the diffusivity of the pore domain is not considered an important quantity to investigate. Only the effective mechanical performance of the binder type structures will be evaluated, and in the same methodology as the electrolyte structures.

The fiber interface passivation layer problem will be studied in 2D. This limitation is due to the heavy computational complexity of the interface problem in 3D. A proof of concept study is done in 3D, but only to illustrate its feasibility, no extensive results will be extracted. Since the interface problem is to be studied in 2D, only the Cahn-Hilliard microstructures will be used. This is primarily because generating reasonable Cahn-Hilliard structures in 2D is a minimal change to the workflow from 3D, which is not the case for the other microstructures.

4.1 Computation of effective properties

Through use of computational homogenization the effective macroscale constitutive properties of the RVEs can be computed. The `COMSOL-MATLAB` API is used to solve the elastic and diffusive homogenization problems pertaining to Equation 2.40 and Equation 2.59. Then, Voigt format is used to evaluate the macroscopic tensors in Equation 2.17 and Equation 2.43. Consider the matrix format of the relation between stress and strain in linear elasticity:

$$\begin{bmatrix}\sigma_{11}\\ \sigma_{22}\\ \sigma_{33}\\ \sigma_{23}\\ \sigma_{13}\\ \sigma_{12}\end{bmatrix} = \begin{bmatrix}E_{1111} & E_{1122} & E_{1133} & E_{1123} & E_{1131} & E_{1112}\\ E_{2211} & E_{2222} & E_{2233} & E_{2223} & E_{2231} & E_{2212}\\ E_{3311} & E_{3322} & E_{3333} & E_{3323} & E_{3331} & E_{3312}\\ E_{2311} & E_{2322} & E_{2333} & E_{2323} & E_{2331} & E_{2312}\\ E_{3111} & E_{3122} & E_{3133} & E_{3123} & E_{3131} & E_{3112}\\ E_{1211} & E_{1222} & E_{1233} & E_{1223} & E_{1231} & E_{1212}\end{bmatrix} \begin{bmatrix}\epsilon_{11}\\ \epsilon_{22}\\ \epsilon_{33}\\ 2\epsilon_{23}\\ 2\epsilon_{13}\\ 2\epsilon_{12}\end{bmatrix} \tag{4.1}$$

By solving the homogenization problem for a given macroscopic driving strain $\bar{\boldsymbol{\epsilon}}$, where all but one element are prescribed as zero, it is possible to calculate the elements of the effective macroscopic stiffness tensor $\bar{\mathbb{E}}$ row wise for each volume average stiffness solution $\bar{\boldsymbol{\sigma}}$. For a driving macroscopic strain $\bar{\boldsymbol{\epsilon}} = \begin{bmatrix}1 & 0 & 0 & 0 & 0 & 0\end{bmatrix}^T$, the first row of the effective stiffness tensor can be calculated as:

$$\begin{bmatrix}\bar{\sigma}_{11}\\ \bar{\sigma}_{22}\\ \bar{\sigma}_{33}\\ \bar{\sigma}_{23}\\ \bar{\sigma}_{13}\\ \bar{\sigma}_{12}\end{bmatrix} = \begin{bmatrix}\bar{E}_{1111}\\ \bar{E}_{2211}\\ \bar{E}_{3311}\\ \bar{E}_{2311}\\ \bar{E}_{3111}\\ \bar{E}_{1211}\end{bmatrix} \tag{4.2}$$

By looping through each driving strain element, the full macroscopic stiffness tensor can be determined.

The effective conductivity of the diffusion problem can be calculated using the same method. Consider the constitutive equation for diffusivity:

$$\begin{bmatrix}j_1\\ j_2\\ j_3\end{bmatrix} = -\begin{bmatrix}D_{11} & D_{12} & D_{13}\\ D_{21} & D_{22} & D_{23}\\ D_{31} & D_{32} & D_{33}\end{bmatrix} \begin{bmatrix}\partial c/\partial x\\ \partial c/\partial y\\ \partial c/\partial z\end{bmatrix} \tag{4.3}$$

By computing the volume averaged flux $\bar{\boldsymbol{j}}$ for a driving macroscopic concentration gradient $\boldsymbol{\nabla}\bar{c}$ in each basis direction, the rows of the effective diffusivity matrix can be calculated. For a given macroscopic concentration

gradient $\boldsymbol{\nabla}\bar{c} = \begin{bmatrix}1 & 0 & 0\end{bmatrix}^T$ the first row can be calculated as:

$$\begin{bmatrix}\bar{j}_1\\ \bar{j}_2\\ \bar{j}_3\end{bmatrix} = -\begin{bmatrix}\bar{D}_{11}\\ \bar{D}_{21}\\ \bar{D}_{31}\end{bmatrix}, \tag{4.4}$$

which allows for all elements in the effective diffusivity matrix to be calculated by solving the diffusivity problem in the microscale for each direction of the driving macroscopic concentration gradient.

4.1.1 Quantity of interest

The chosen main quantity of interest (QOI) for the effective material properties is their quasi-isotropic values, normalized with respect to the isotropic microscale properties. The chosen QOI for the elasticity problem is the quasi-isotropic Young's modulus $\bar{E}$ which is calculated from the effective stiffness matrix. The QOI for the pore structures is the quasi-isotropic ionic diffusivity $\bar{D}$. In Voigt format the effective stiffness matrix is written as:

$$\bar{\mathbb{E}} = \begin{bmatrix}\bar{E}_{1111} & \bar{E}_{1122} & \bar{E}_{1133} & \bar{E}_{1123} & \bar{E}_{1131} & \bar{E}_{1112}\\ \bar{E}_{2211} & \bar{E}_{2222} & \bar{E}_{2233} & \bar{E}_{2223} & \bar{E}_{2231} & \bar{E}_{2212}\\ \bar{E}_{3311} & \bar{E}_{3322} & \bar{E}_{3333} & \bar{E}_{3323} & \bar{E}_{3331} & \bar{E}_{3312}\\ \bar{E}_{2311} & \bar{E}_{2322} & \bar{E}_{2333} & \bar{E}_{2323} & \bar{E}_{2331} & \bar{E}_{2312}\\ \bar{E}_{3111} & \bar{E}_{3122} & \bar{E}_{3133} & \bar{E}_{3123} & \bar{E}_{3131} & \bar{E}_{3112}\\ \bar{E}_{1211} & \bar{E}_{1222} & \bar{E}_{1233} & \bar{E}_{1223} & \bar{E}_{1231} & \bar{E}_{1212}\end{bmatrix}. \tag{4.5}$$

For an isotropic material the stiffness matrix can be written in the form:

$$\mathbb{E} = \begin{bmatrix}2\mu+\lambda & \lambda & \lambda & 0 & 0 & 0\\ \lambda & 2\mu+\lambda & \lambda & 0 & 0 & 0\\ \lambda & \lambda & 2\mu+\lambda & 0 & 0 & 0\\ 0 & 0 & 0 & \mu & 0 & 0\\ 0 & 0 & 0 & 0 & \mu & 0\\ 0 & 0 & 0 & 0 & 0 & \mu\end{bmatrix}, \tag{4.6}$$

where λ and μ are the Lamé constants. The Young's modulus can be related to the Lamé constants [30]:

$$E = \frac{\mu(3\lambda+2\mu)}{\lambda+\mu}. \tag{4.7}$$

By assuming that the potentially anisotropic effective stiffness matrix in Equation 4.5 is approximately isotropic, the quasi-isotropic Lamé constants can be calculated as an average of the components which would in an isotropic case correspond to λ and μ:

$$\bar{\lambda} = \frac{1}{3}(E_{1122} + E_{1133} + E_{2233}) \tag{4.8}$$

$$\bar{\mu} = \frac{1}{3}(E_{2323} + E_{3131} + E_{1212}) \tag{4.9}$$

From which the quasi-isotropic Young's modulus can be calculated:

$$\bar{E} = \frac{\bar{\mu}(3\bar{\lambda}+2\bar{\mu})}{\bar{\mu}+\bar{\mu}}. \tag{4.10}$$

Similarly, the quasi-isotropic ionic conductivity can be calculated from the assumption that the conductivity matrix is approximately isotropic. The anisotropic effective conductivity matrix has the form:

$$\boldsymbol{D} = \begin{bmatrix}\bar{D}_{11} & \bar{D}_{12} & \bar{D}_{13}\\ \bar{D}_{21} & \bar{D}_{22} & \bar{D}_{23}\\ \bar{D}_{31} & \bar{D}_{32} & \bar{D}_{33}\end{bmatrix} \tag{4.11}$$

And the isotropic counterpart has the form:

$$\boldsymbol{D} = \begin{bmatrix}D & 0 & 0\\ 0 & D & 0\\ 0 & 0 & D\end{bmatrix} \tag{4.12}$$

The quasi-isotropic ionic diffusivity is thus calculated as:

$$\bar{D} = \frac{1}{3}(\bar{D}_{11} + \bar{D}_{22} + \bar{D}_{33}) \tag{4.13}$$

4.2 Periodic mesh

The numerical modeling presented in chapter 2 relies on SPBCs which require a strictly periodic mesh. The same dependency goes for the Cahn-Hilliard and damage phase field equations presented in chapter 3. Generating a periodic mesh for the latter examples is trivial as the computational domain is a simple cube. In COMSOL any non-specific mesh for such a domain will end up periodic as a result of the meshing routine. When solving the homogenization problem with the synthetic microstructures as computational domain, guaranteeing a periodic mesh becomes a non-trivial problem.

Because the analysis needs to be automated, the meshing routine cannot be performed manually. By creating a series of selection boxes in COMSOL that only include specific faces and edges, it is possible to create selection groups for all boundary faces and edges. The first step to the mesh generation is to mesh one of each boundary edge parallel to the coordinate axes, and to then copy these onto all other parallel boundary edges. All these source and destination edges are already detected through the previously mentioned selection groups. The next step is to perform the same operation for all boundary faces. Three orthogonal boundaries are meshed, after which they are copied onto the opposite face, see Figure 4.1. Once this is done the domain is fully meshed at the boundaries, and due to the exact copying the mesh will be periodic and thus allow for SPBCs. The rest of the domain can meshed with free tetrahedral elements.

COMSOL's meshing algorithm has been found to be very sensitive, which has both advantages and disadvantages. In particular, the mesh routine will throw an error during the copying operations if any destination geometry does not match its source. This means that if a structure is not perfectly periodic, the mesh routine will catch it. The downside is that the copying operations can still fail, even if the structure is periodic, due to other topological details that the meshing routine does not handle well, and still throw the same error, as already alluded to in subsection 3.4.1 for the cylinder seams. One factor that has been found to greatly influence the chance of the mesh routine succeeding are the geometry import settings. Which settings that break the meshing routine is not consistent. In one case, the automatic removal of redundant edges is required for the mesh to succeed, and for other cases, it is the single feature that prevents it. As a result each structure type ended up with a different set of import settings that were found to work often enough, which were chosen through trial error.

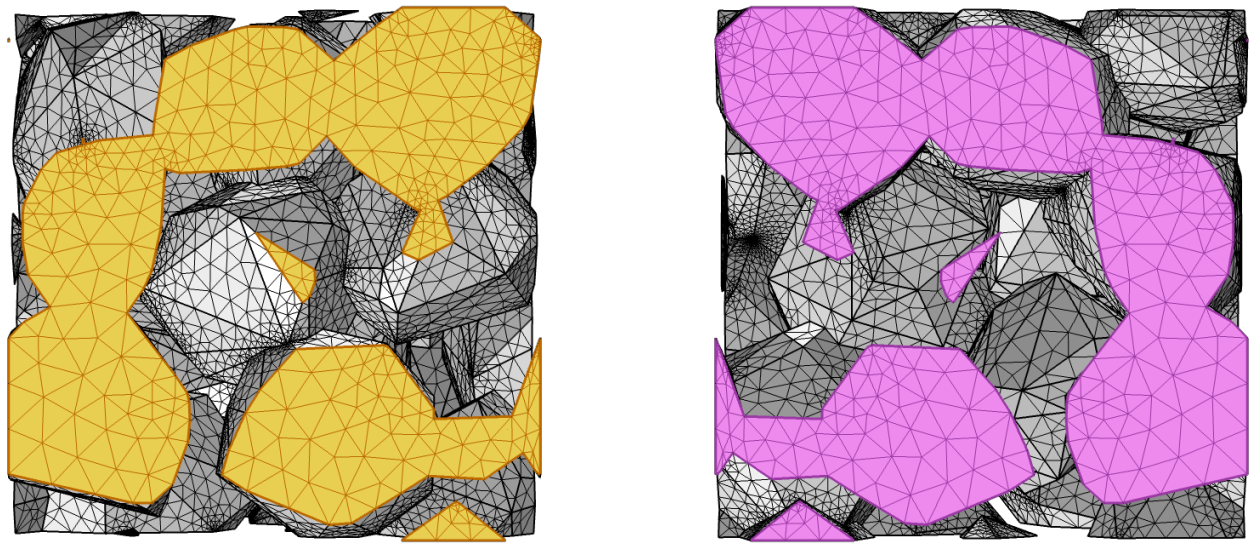

(a) Source boundary for periodic face mesh.

(b) Destination boundary for periodic face mesh.

Figure 4.1: Screenshots of the selection groups for the periodic mesh.

4.3 Convergence study

Since the finite element method is a numerical method dependent on a spatial discretization, it is crucial to investigate that the solution achieves sufficient convergence for a fine enough mesh. A mesh convergence study is necessary for each type of microstructure to get an indication of how high the resolution needs to be to obtain accurate results. The study is performed by repeatedly solving the stiffness and diffusion problems to obtain the effective properties of a given realization for an increasingly fine mesh. The study will assume that the convergence for one realization of a type of structure will be roughly the same for all realizations.

The chosen refinement scheme is to change the general mesh settings in `COMSOL` from its coarsest to finest setting, which automatically adjusts the program's mesh parameters such as minimum and maximum element sizes, maximum element growth rate, and others. The advantage of this method in this context is that it is applicable to all microstructures with minimal changes required. The varying complexity of the geometries would require a great deal of specific tuning for each type of structure, should their mesh settings be selected manually. A downside to this method is that the number of mesh resolutions is low, going up to only nine settings. Furthermore, the different structures cannot all necessarily be meshed for all settings and as a result will have fewer mesh generations. As such, the deviation from the finest value of each study will be referred to as an "error".

Table 4.1: `COMSOL` general mesh settings.

Description	Setting
Extremely fine	1
Very fine	2
Finer	3
Fine	4
Normal	5
Coarse	6
Coarser	7
Very coarse	8
Extremely coarse	9

Since there is a chosen quantity of interest (QOI) for the stiffness and diffusivity problems, those will be the quantities for which the convergence is studied. Since both of these quantities are essentially averages of already volume averaged quantities they are expected to convergence quickly, to the point of possibly showing negligible change for increasing degrees of freedom. The convergence figures all are normalized against the finest solution in each study to illustrate the convergence better. This assumes that the finest solvable mesh gives a converged solution. This is considered reasonable, as the contrary would imply that a fine enough mesh to achieve convergence is not possible.

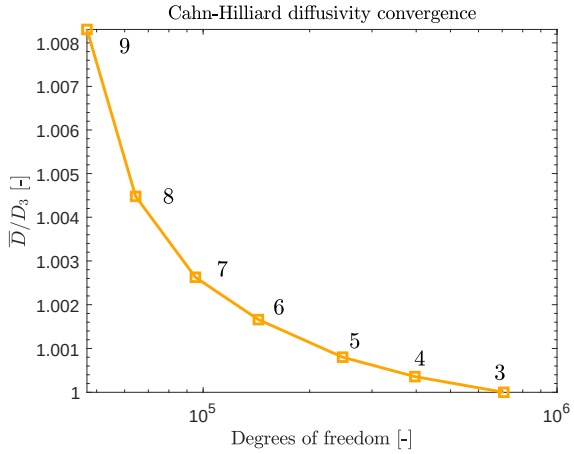

(a) Convergence for effective diffusivity in the Cahn-Hilliard structures.

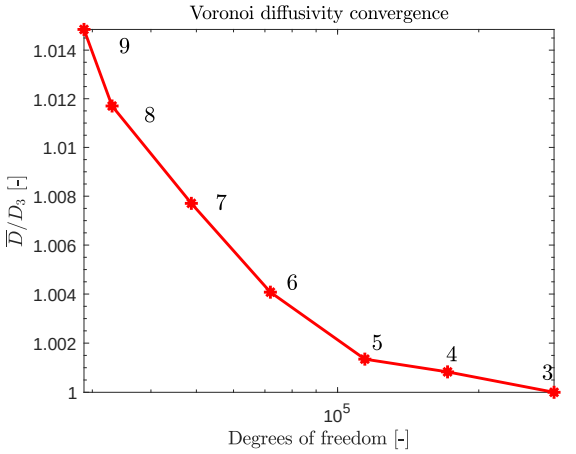

(b) Convergence for effective diffusivity in the Voronoi structures.

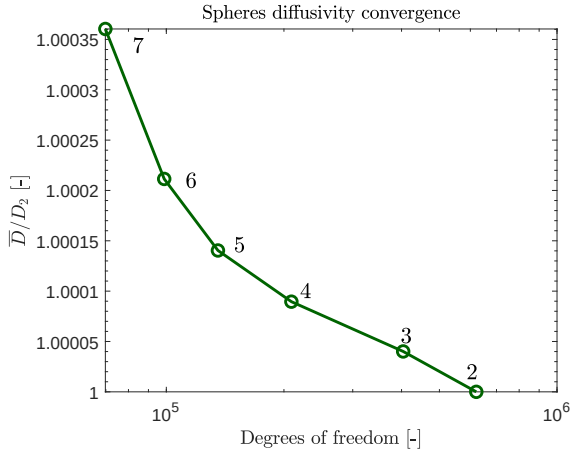

(c) Convergence for effective diffusivity in the sphere structures.

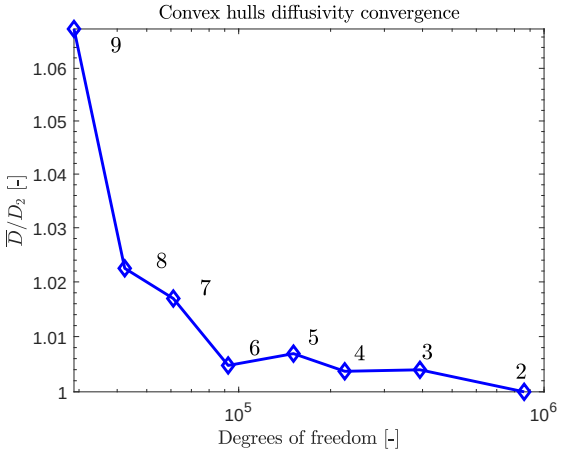

(d) Convergence for effective diffusivity in the convex hull structures.

Figure 4.2: Diffusion convergence.

The diffusion convergence is shown in Figure 4.2. The sphere structures show close to no change in effective diffusivity for increased fineness settings. Both the Cahn-Hilliard and Voronoi structures have very little change in diffusivity, only 0.08% error between coarsest and finest settings for the Cahn-Hilliard and 1.4% for the Voronoi structures. At around the fifth setting this error is less than 0.1%. For the convex hull structures the convergence curve clearly flattens around the fifth and sixth settings. This may however be due to the ninth setting resulting in a much higher diffusivity than the other settings. The error at the sixth and fifth is still less than 1% and considered within convergence.

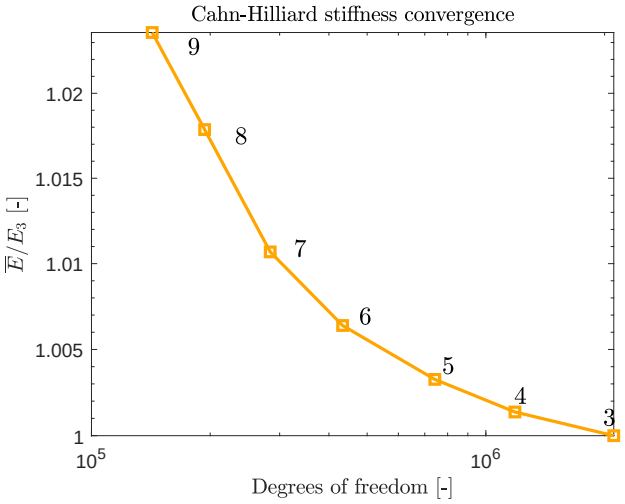

(a) Convergence for effective stiffness in the Cahn-Hilliard structures.

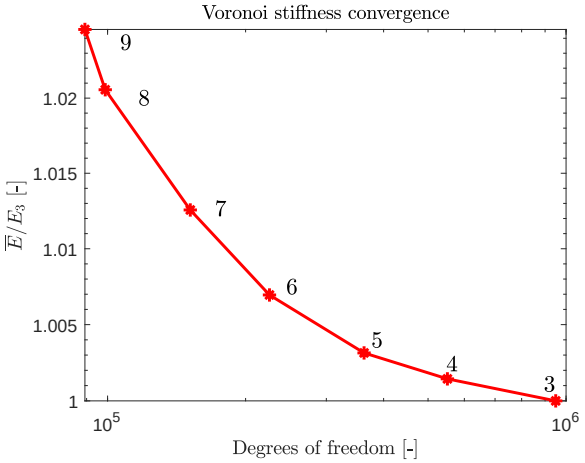

(b) Convergence for effective stiffness in the Voronoi structures.

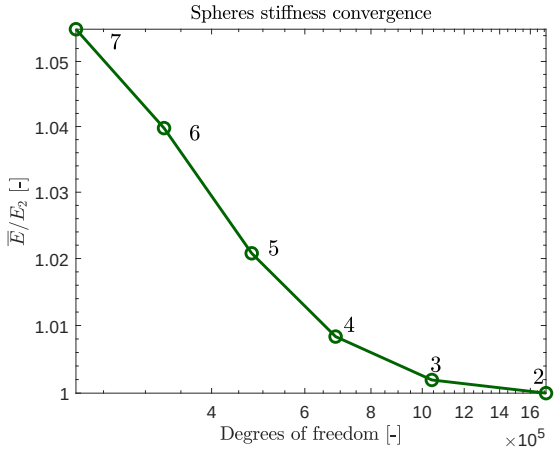

(c) Convergence for effective stiffness in the sphere structures.

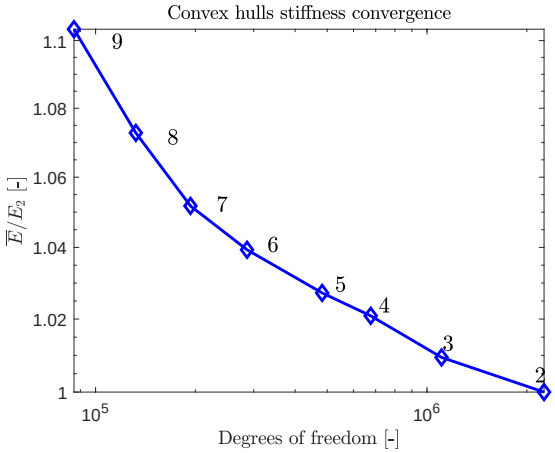

(d) Convergence for effective stiffness in the convex hull structures.

Figure 4.3: Stiffness convergence.

The vertical axis once again shows that the QOI has negligible change for increased degrees of freedom. The errors for the Cahn-Hilliard and Voronoi structures are not as low as for diffusivity, but still quite low at around 0.5% at the fifth setting. The sphere and convex hull structures have a bit higher errors. For the spheres this is in the magnitude of single percentages, while the convex hull has 10% error for the coarsest setting. At around the fifth setting the errors are still below 3% for both, and considered good enough. Therefore, the fifth mesh setting is considered sufficient for all structures. This would correspond to the "Normal" setting in `COMSOL`. In general however the convergence plots make it clear that indeed the volume averaged quasi-isotropic values converge very quickly as a result of it effectively being a double averaged quantity.

The binder structure is studied only for the stiffness problem and with the same properties for both particle and binder. In addition, the convergence is also studied for the passivation layer, where the area averaged vertical stress at 90% interface averaged damage is the chosen QOI.

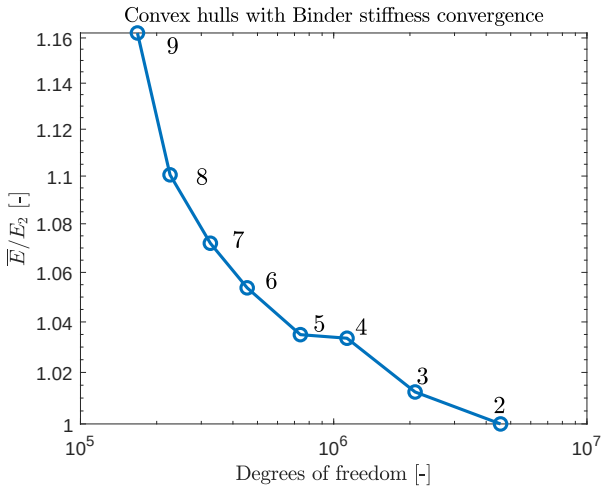

(a) Convergence for effective stiffness in the sphere structures.

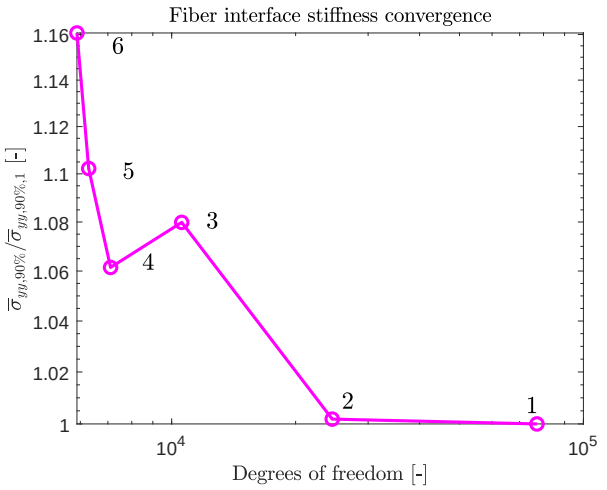

(b) Convergence for the area average vertical stress at 90% interface averaged damage.

Figure 4.4: Binder and passivation layer convergence.

For the binder structure, the coarsest setting reaches a higher error than the other structures but the fifth setting, normal mesh quality, is again considered sufficient. In the case of the passivation layer, settings coarser than the fifth setting resulted in overlapping values and all settings coarser than the sixth was omitted in the figure. Unlike the 3D microstructures the finest setting was solvable, which raises the error for the coarser somewhat. The fifth setting has roughly 10% error and is chosen as it is considered fine enough and computationally advantageous.

4.4 Electrolyte microstructure

The four microstructures presented in chapter 3 are simulated using `COMSOL` and their effective properties are computed using computational homogenization as explained in chapter 2. The stiffness and diffusion is computed with the methodology explained in chapter 4.1. The material properties choice for the electrolyte microstructures are chosen as $E = 1$ and $\nu = 0.25$, and $D = 1$. Since the quantities of interest are the normalized quasi-isotropic values the parameter values themselves are not considered to be significant.

The SVEs are generated in sample sizes of 100 per "ideal volume fraction" set. This meaning, that each type of structure is generated and solved for 100 times for different attempted final solid volume fractions. All structures have different degrees of accuracy in the ability to predetermine their volumes. For example, a Cahn-Hilliard structure filtered for a volume fraction of 0.5 can have actual values between 0.49 and 0.51. The convex hull structures, despite attempts to control the output volume, have a very wide volume spread. Both the sphere and Voronoi structures use a bisection method with a tolerance of 0.02 volume units to control the structure volume.

In the figures below, the effective stiffness, effective diffusivity, and the bifunctional performance of the microstructures are plotted in Figures 4.5, 4.5, and 4.7 respectively. In addition, some statistical properties are plotted in Figure 4.8 In the performance result plots, the effective properties are compared with the results of previous research [31]. All figures in the comparison are reproduced with the permission of the author Vinh Tu. The referenced paper generated similar microstructures, under different naming conventions. Beads are comparable to the sphere structures in this project. Imperfect trabecular also used the Cahn-Hilliard equation, and are comparable to the Cahn-Hilliard type structures. Just trabecular, refers to a Voronoi tessellation based structure which used a heat equation instead of a damage phase field. The author modeled the electrochemical process as an ion conductivity problem using Fickian diffusion, and as such the quantity relating to electrochemical performance is conductivity as opposed to diffusivity. However, the only difference between these two is the choice of units, the numerical values are comparable. Additionally the black markers with letters refer to experimental

values for certain polymers. Lastly, the Voigt-Taylor bound refers to a theoretical upper bound. This upper bound is characterized as the effective normalized stiffness being equal to the solid volume fraction, and the effective normalized diffusivity being equal to the porosity.

The cited study also chose to extend their porosity range by introducing the inverse for each of their structures as a new type of structure. To clarify, this means that the stiffness problem is solved for the solid phase, which is described by the legend. The diffusion problem is solved for the pore phase of the solid domain, effectively meaning the inverse of the entry in the legend. For example, the stiffness problem for the bead structures is solved on the bead structures solid domain, and the diffusion on the pore domain of that structure. So when the figure refers to the inverted bead structure, the solid domain is the bead structure pores, and the pore domain is the bead structure's solid domain.

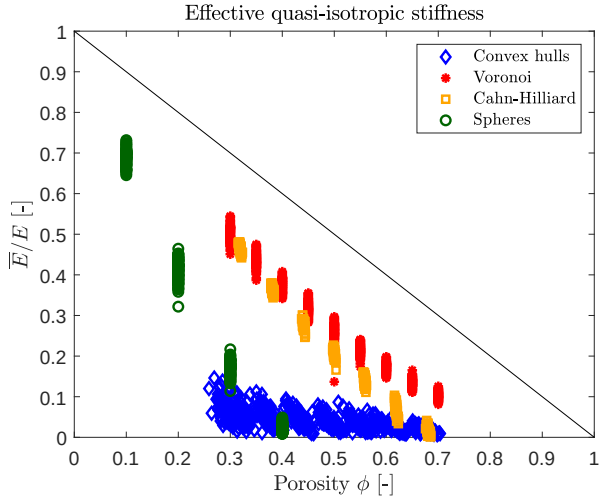

(a) Normalized effective stiffness.

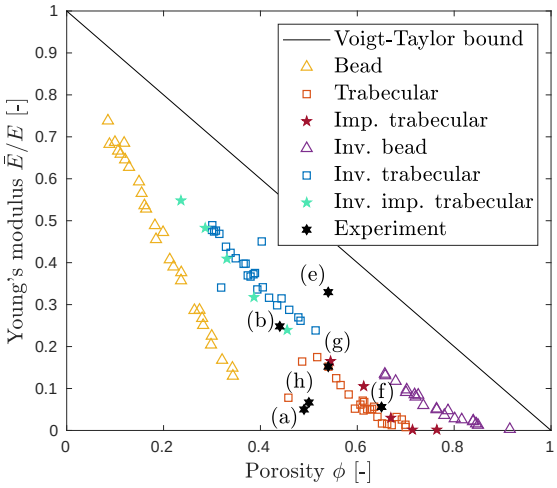

(b) Normalized effective stiffness, compared results.

Figure 4.5: Effective stiffness plotted for each realization. Figure a) plots the results produced in this project, b) is from a different paper.

The first observation in Figure 4.5a is the close to non-existent spread in porosity for all microstructures except the convex hull structures. This is as expected because the other methods have reliable and accurate ways of controlling the output volume whereas the convex hulls do not. All but the spheres structure roughly cover the 0.3-0.7 porosity range. This is an methodological limitation due to the swelling method being unable to consistently produce continuous structures at higher porosities. All structures display a certain degree of variance in their stiffness. The Cahn-Hilliard structures appear to have the least amount of spread in stiffness. There appears to be a trend in which all structures have a decreased variance in stiffness for higher porosities. The spread for all structures is fairly similar, but the relative deviation for the convex hull structures is much larger, owing to the lower range of stiffness values. The reason for the much lower stiffness of the convex hull structures is likely related to the connectivity. The minimum spanning tree algorithm after periodic mirroring results in approximately 2.5 connections per convex hull. A different network algorithm could be used to raise the stiffness. Furthermore, there is a very clear trend that each different type of structure has a linear relation between porosity and stiffness.

Compared to the results in Figure 4.5b, there is is a clear similarity between the Cahn-Hilliard and imperfect trabecular structures, and the Voronoi and inverted trabecular structures. As these structures are generated in similar ways this is the expected result. It should be noted that the damage phase Voronoi structures used a lower bound filter to extract the solid geometry phase. The trabecular structures used in Figure 4.5b used a different method which would be analogous to an upper bound filter. What this means is that that the inverted trabecular structures are geometrically more similar to the Voronoi structures, than the trabecular

structures. The trabecular structures, which are similar to the pore phase of the Voronoi structures, are closer to the Cahn-Hilliard structures in performance. The stiffness for the sphere and bead structures are also similar. This is an interesting result since the study in this project use bidisperse packings, while the previous study used monodisperse packings. A more thorough parametric study would be necessary, but this could indicate that the dispersity might not have as much of an influence on the stiffness as the porosity. Another interesting observation is that the convex hull structures manage to cover the lower stiffness values of experimental results (a) and (h), which none of the other structures in either study does.

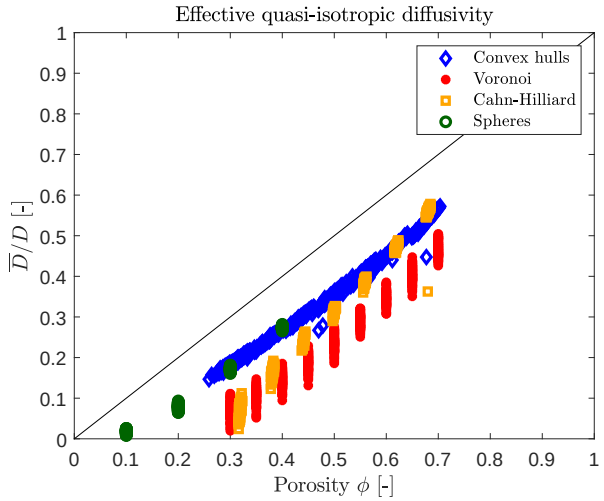

(a) Normalized effective diffusivity.

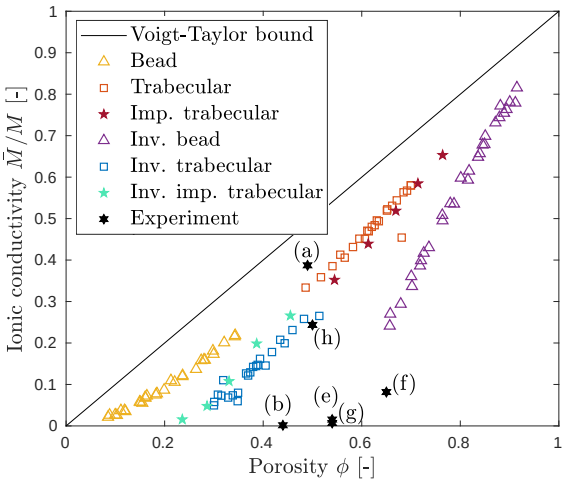

(b) Normalized effective conductivity, compared results.

Figure 4.6: Effective diffusivity/conductivity plotted for each realization. Figure a) plots the results produced in this project, b) is from a different paper.

What immediately stands out for the effective diffusivity in Figure 4.6a is the very narrow spread in diffusivity for the sphere and convex hull structures. Compared to the stiffness, there is close no variance for a given porosity. By contrast, the Cahn-Hilliard and Voronoi structures instead show a significant spread in diffusivity. The spread for both structures taper for increasing porosity, but the decrease is greater for the Cahn-Hilliard structures. The convex hull and sphere structures appear to have virtually identical values for the same porosities, and their slopes align. This seems to indicate that the pore phases for the sphere and convex hull structures are very similar, and that for neither case the specific configuration has much influence on the diffusivity compared to the porosity. For the higher porosity range of 0.6-0.7 the Cahn-Hilliard structures reach a diffusivity similar to the other two, while the Voronoi structures remain slightly lower.

Comparing Figures 4.6a and 4.6b, it is again seen that the Cahn-Hilliard structures produce similar values as the imperfect trabecular structures, and inverted imperfect trabecular structures. This is the expected result since both phases in the Cahn-Hilliard structure are similar in topology due to the unbiased phase separation equation they are based on. The Voronoi structures have comparable diffusivity to the inverted trabecular. The maximum values for each set are very close to the inverted trabecular, but the mean and minimum values deviate a fair bit. It is again seen that the Voronoi structures are much closer to the inverted trabecular than the trabecular structures, as is the expected result. The sphere structures produce the same values as the bead structures, strengthening the possibility that the dispersity may not be a significant factor.

One more interesting observation with both results in consideration is that the convex hull structures manage to match the experimental value (a) in both the diffusivity and stiffness cases, which none of the structures examined in the cited study managed. They are also fairly close to experimental value (h), but do not encompass

it for the diffusivity case.

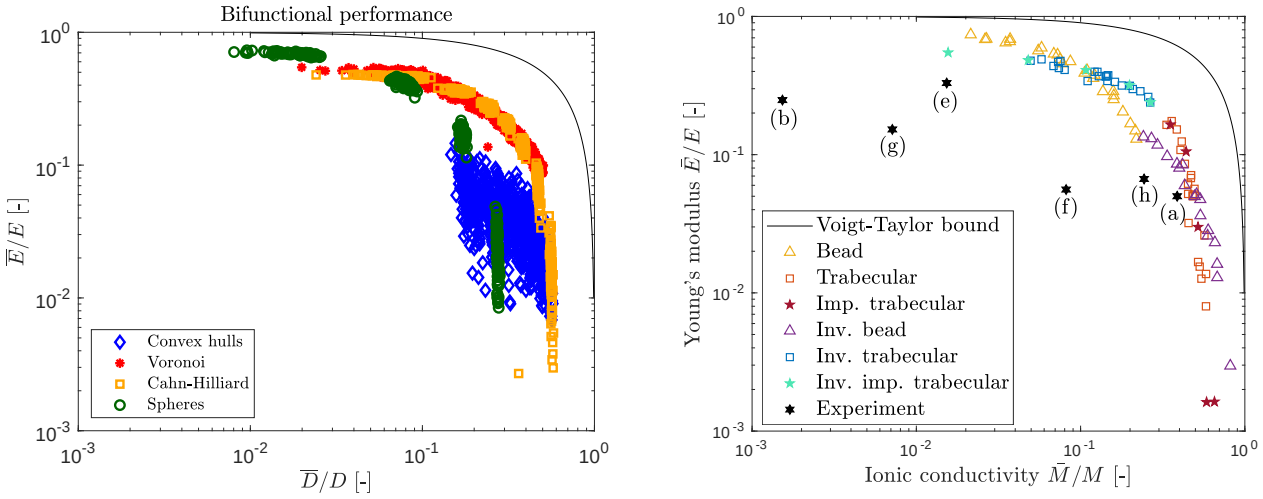

(a) Bifunctional performance.

(b) Bifunctional performance, compared results.

Figure 4.7: Bifunctional performance of each realization. Figure a) plots the results produced in this project, b) is from a different paper.

The bifunctional performance is evaluated by plotting the effective stiffness over the effective diffusivity for each realization. The Cahn-Hilliard and Voronoi structures show a large amount of overlap, however with the the Cahn-Hilliard structures extending into lower stiffness values for the higher diffusivity values. The sphere structures perform worse in diffusivity, but manage to reach higher stiffness values. This is likely a result of the sphere structure's much stronger and uniform connectivity. The convex hull structures, unlike all the other ones, do not follow the same curve. Instead they seem to form a cloud between the sphere and Cahn-Hilliard lines. Judging from the stiffness results in Figure 4.5a this is most likely caused by the large spread in stiffness. In terms of bifunctional performance the Cahn-Hilliard and Voronoi structures appear to have similar performance, which is also the best performance of the presented microstructures. The sphere structures reach a higher stiffness but this is due to the lower porosity, which is more clearly illustrated in previous figures. This seems to indicate that for maximizing both stiffness and diffusivity a microstructure like the Voronoi or Cahn-Hilliard structures would be optimal. The performance of the two structures is most likely a result of how their solid and pore phases are both very similar. Unlike the sphere and convex hull structures that have distinctively different topology between the two phases.

Compared to Figure 4.7b the results seem fairly similar, and the general shape is that they mirror the Voigt-Taylor bound curve with an offset. Most structures produce results similar to their counterparts in the previous study. The convex hull structures again stand out in this plot as they manage to cover the bifunctional performance of experimental values (h) and (a), which no other structure does. This seems to imply that the convex hull structures may be very useful as a synthetic SBE microstructure.

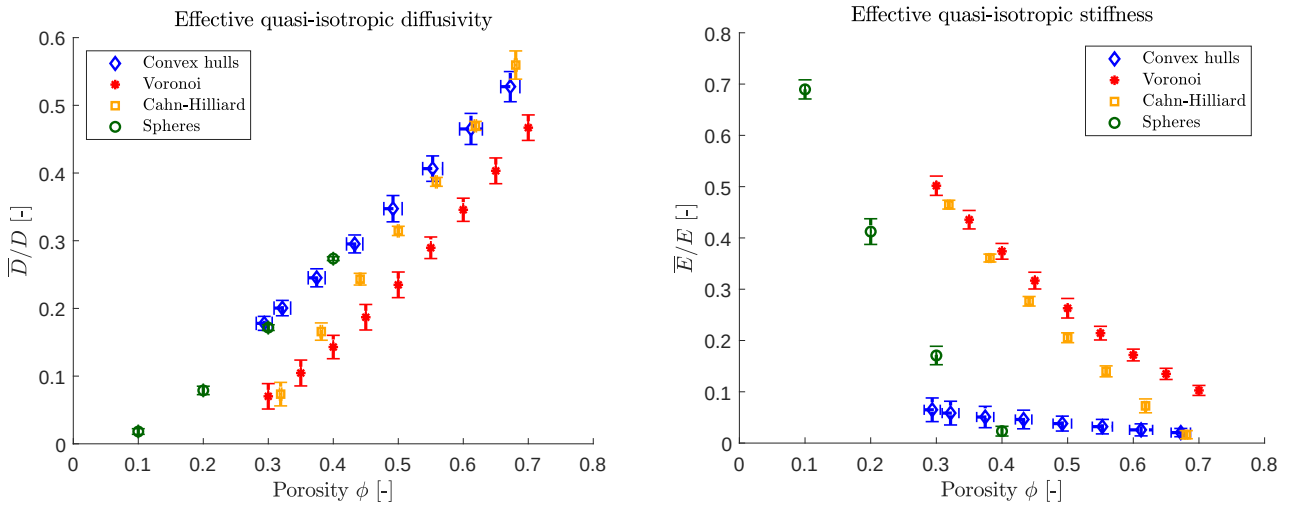

(a) Normalized effective diffusivity.

(b) Normalized effective stiffness.

Figure 4.8: Effective properties plotted for the mean value and porosity of each volume set. Vertical bars indicate the standard deviation for diffusivity/stiffness. Horizontal bars indicate the standard deviation in porosity.

Comparing the standard deviation for each volume set in Figure 4.8 to the spread seen in Figures 4.5 and 4.6, there are few interesting observations. Despite the apparent wide spread of stiffness for the convex hull, the standard deviation is fairly narrow. Generally of the same degree as the other structures. The standard deviation of porosity is close to nonexistent for all structures except the convex hulls, as is the expected result. For stiffness the sphere structures have the highest deviation of all sets at a porosity of 0.2. The deviation of stiffness for the spheres seem to decrease at the even lower porosity of 0.1, but the general trend is that the stiffness deviation increases for lower porosities. For diffusivity there is no apparent relation between deviation and porosity which applies for all structures.

4.5 Electrode microstructure

A key feature of the convex hull with binder microstructure, representing the positive electrode, is the ability to assign different material properties. Therefore the Young's modulus and Poisson's ratio are not chosen arbitrarily. The material properties are chosen as $E_{\text{particle}} = 140$ GPa, $E_{\text{binder}} = 0.5$ GPa and $\nu = 0.3$, where the particle stiffness is chosen from experiments [32] and binder stiffness is chosen as a typical polymer value. The structures are generated for the solid volume fractions 0.2, 0.3, 0.4, 0.5, 0.6, and 0.7 with 50 realizations for each set. The effective properties are calculated the same way as for the electrolyte structures. In addition, the effective quasi-isotropic shear and bulk moduli are computed through the relations:

$$G = \mu \tag{4.14}$$

$$K = \lambda + 2\mu/3 \tag{4.15}$$

The effective stiffness in relation to structure porosity is plotted in Figure 4.9. Then, the effective stiffness along with the effective shear and bulk moduli are plotted with respect to the specific particle and binder volume fractions respectively in Figure 4.10.

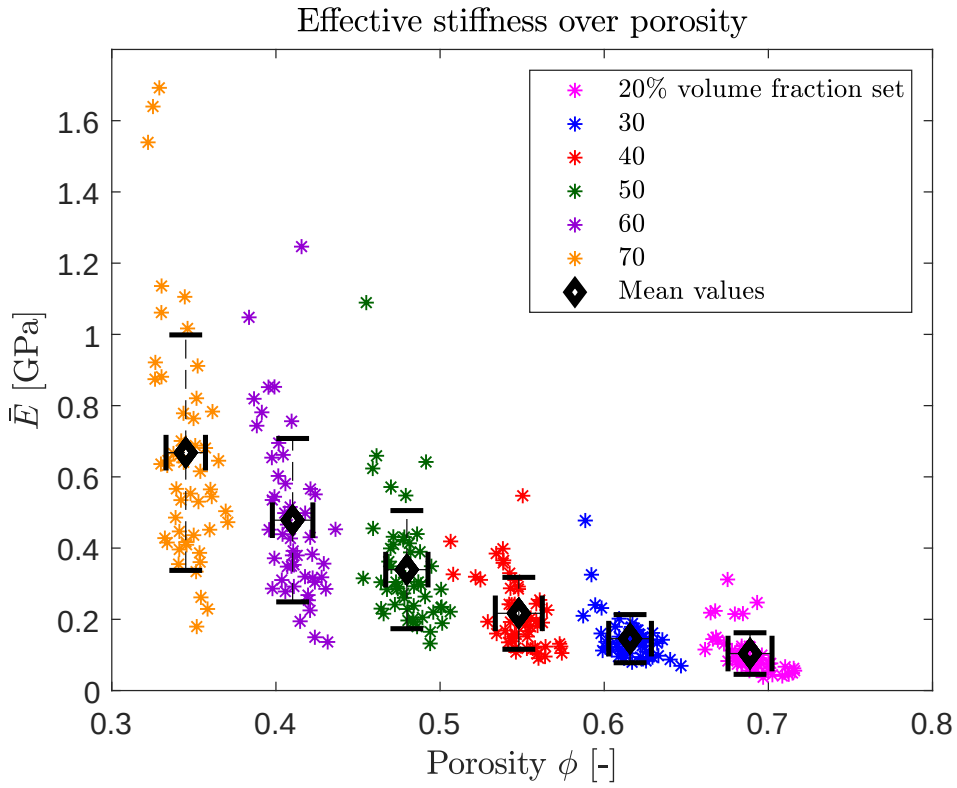

Figure 4.9: Effective stiffness over porosity for each realization. Horizontal bars indicate the standard deviation of porosity. Vertical bars indicate the standard deviation of stiffness.

A fairly high spread in stiffness is observed in Figure 4.9. For higher porosities the variance is lower. Compared to the isotropic stiffness of the binder, the SVEs effective quasi-isotropic stiffness is of a similar order of magnitude. This could mean that the effective stiffness of the SVE is heavily dependent on that of the binder material. The magnitude of the stiffness compared to the particle is around two orders of magnitude lower, which shows that the stiffness is significantly reduced compared to a pure particle structure. The relation between stiffness and porosity appears roughly linear in regards to the mean values, similar to the behavior observed for the electrolyte microstructures. The standard deviation in porosity is roughly the same for all volume sets. The deviation of stiffness increases for decreasing porosity, similar to what was observed for the electrolyte structures. In particular, some of the structures with the lowest porosity show some extreme outlier values.

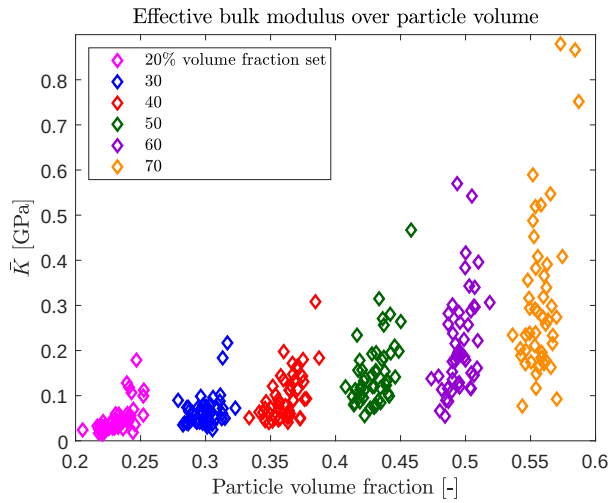

(a) Effective bulk modulus.

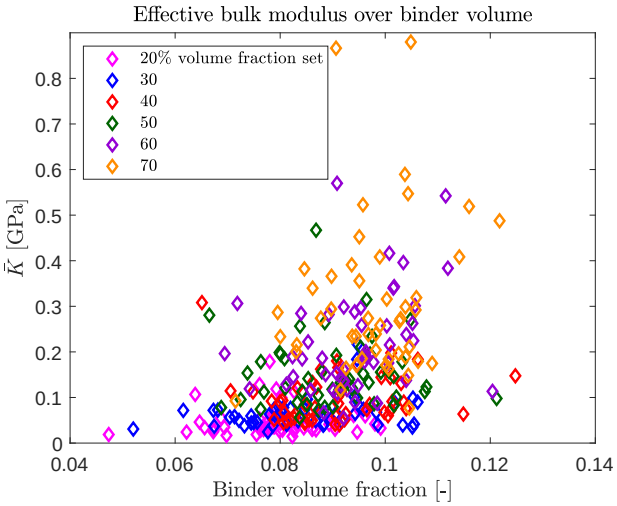

(b) Effective bulk modulus.

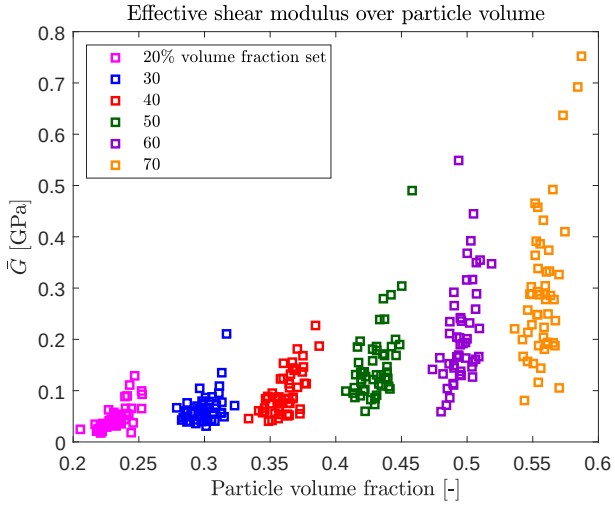

(c) Effective shear modulus.

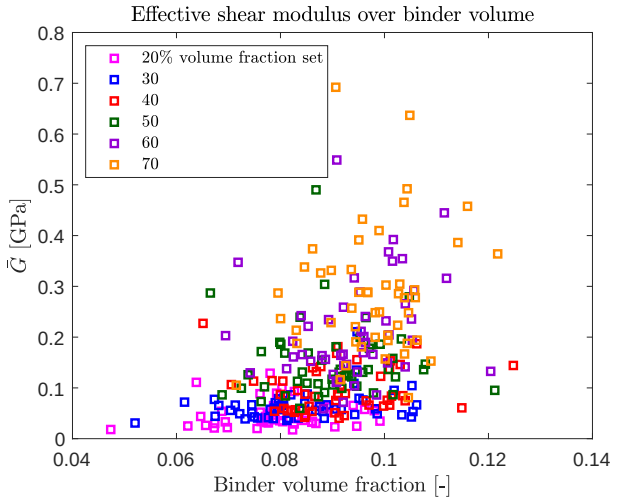

(d) Effective shear modulus

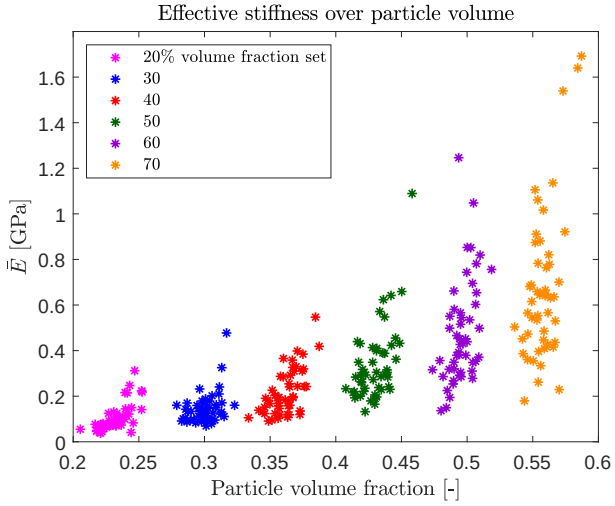

(e) Effective stiffness.

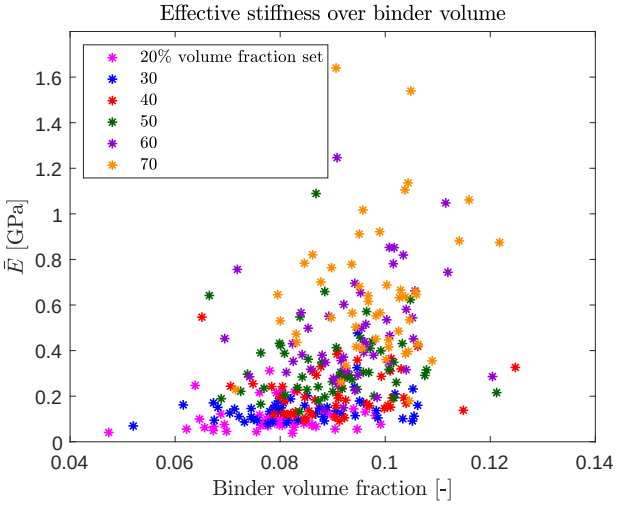

(f) Effective stiffness.

Figure 4.10: Effective properties plotted against particle and binder volume fraction.

Plotting the mechanical moduli over the particle volume fraction it is clear that the relation between stiffness and volume resembles the relation between effective stiffness and porosity in Figures 4.10a, 4.10c, and 4.10e. The moduli are plotted against particle volume fractions, since a porosity measure would not make sense when describing the particle's presence in the domain.

In contrast to the observation made from particle volume fraction plots, the binder volumes plots in Figures 4.10b, 4.10d, and 4.10f seem to indicate that the volume fraction of the binder has no effect on the effective stiffness. However these are not mutually exclusive properties, but the hypothesis could me made that the binder's stiffness has a bigger influence of the effective stiffness than the particles, and the particle's volume fraction has a bigger influence on the effective stiffness than the binder's. It is recognized that the effect of binder volume on the effective stiffness could be misleading due to the potentially narrow range of volumes, and that the only parametric change between volume sets is binder radius. Other properties such as binder length or number of binder connections contribute to the binder volume and could have a different effect on the effective stiffness.

4.6 Passivation layer interface interaction

Results for the passivation layer interface problem are presented for the parameters in Table 3.1. First, the stress and damage response for the sample in Figure 3.22 are presented. The macroscopic strain is applied until the average interface damage is at 90%.

Figure 4.11 shows the area averaged stress and damage when plotted against the different SEI layer stiffnesses. It is clear that the damage propagates faster when the stiffness is increased. The average interface damage increases exponentially with applied strain at first. However, as the delamination progresses, the behavior becomes more linear, and finally logarithmic. Similarly, the stress increases with the stiffness. The stress behaves linearly up until a certain strain level at which a kink is observed. At this point delamination is initiated and the slope decreases non-linearly until it is dominated by the solid domain's stiffness. Furthermore, it is observed that the failure strain is strictly increasing for increasing passivation layer stiffnesses.

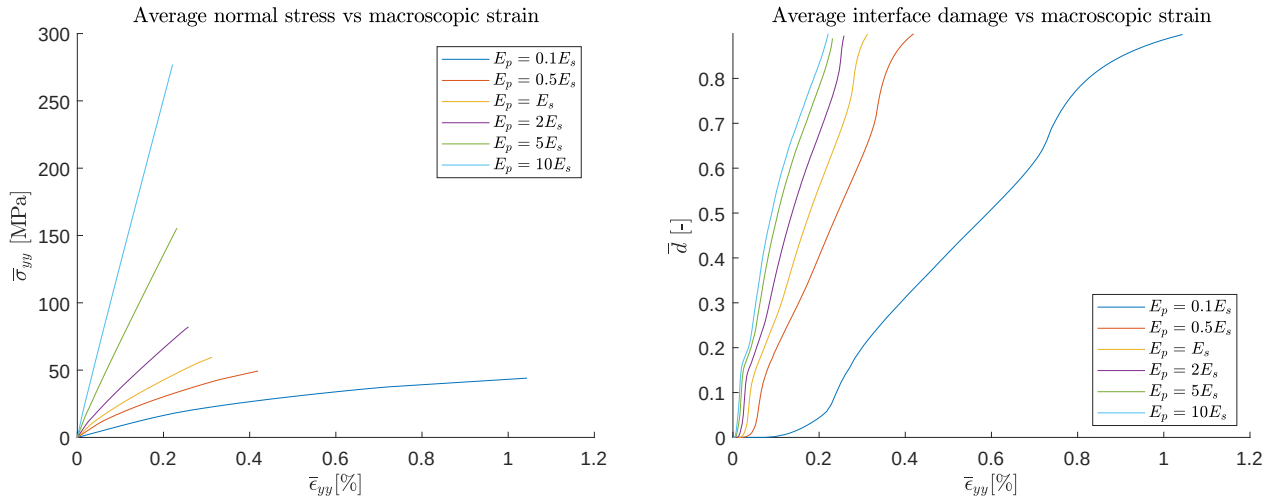

(a) Stress response over strain for different passivation layer stiffnesses

(b) Average interface damage over strain for different passivation layer stiffnesses

Figure 4.11: Stress and damage evolution for increasing macroscopic strain.

Figure 4.12 shows the damage evolution along the boundaries when the strain is ramped for a ratio of $k = 0.1$, which indicates the ratio between the solid domain's stiffness E_s and the passivation layer's stiffness E_p such that $E_p = k \cdot E_s$. The deformation in the surface plot is scaled with a factor of ten to better illustrate the delamination process.

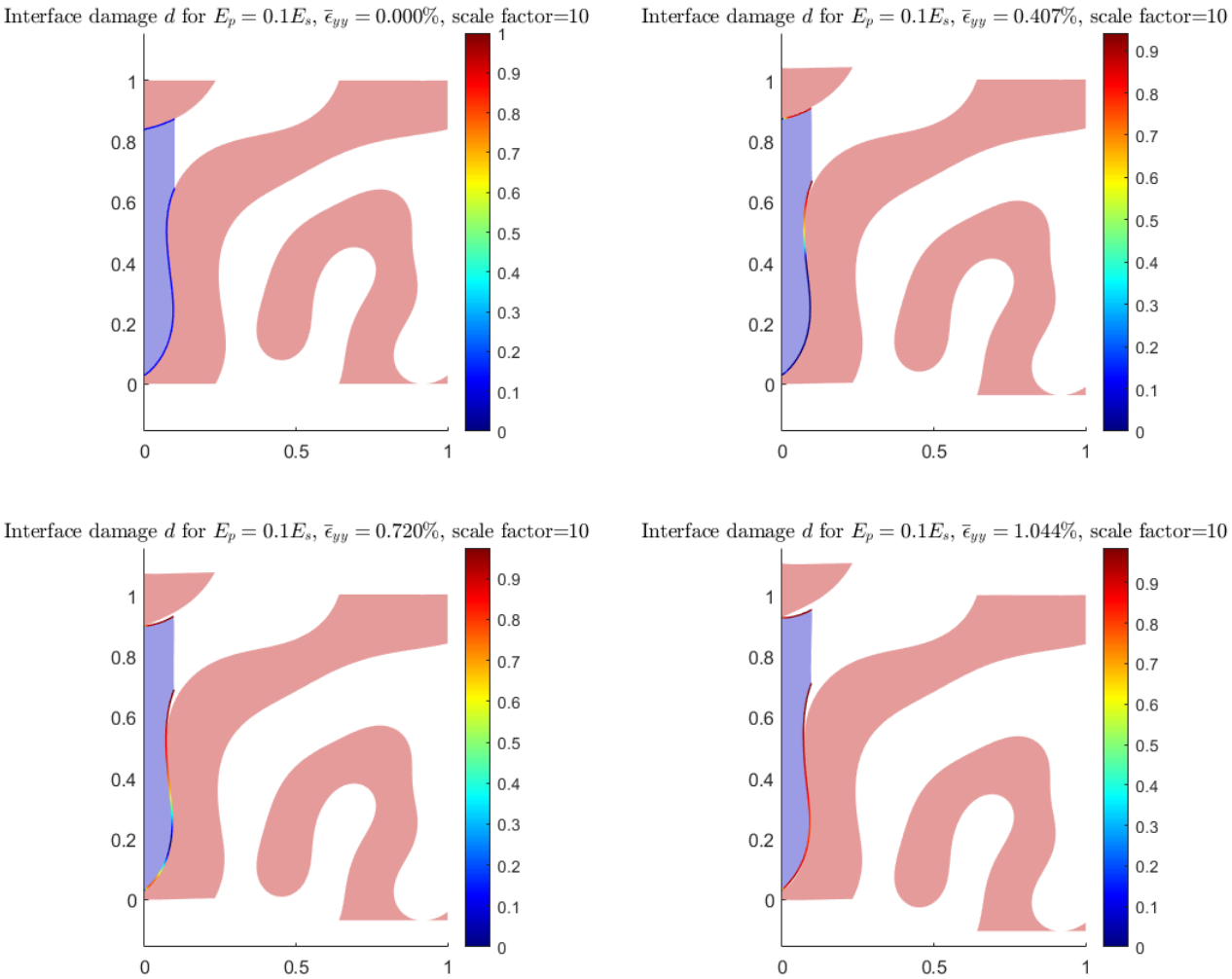

Figure 4.12: Illustration of delamination evolution for the passivation layer.

The area averaged stress and macroscopic strain are evaluated for 100 SAEs for different groups of ideal area fractions chosen between 0.3-0.7. For each sample the strain is applied until 90% of the interface is damaged. The macroscopic strain and homogenized stress are plotted against porosity. Figure 4.13 and Figure 4.14 show the results for the strain and stress for increasing ratios of passivation layer stiffnesses chosen as fractions of the solid phase's stiffness. Here, $\overline{\sigma}_{yy,90\%}$ and $\overline{\epsilon}_{yy,90\%}$ are used to denote the stress and strain values pertaining to a interface damage of 90%. Dashed lines illustrate the standard deviation from the mean values for stress and strain in the vertical direction and for porosity in the horizontal direction. The solid lines connecting the different porosity groups indicate the mean values of stress and strain.

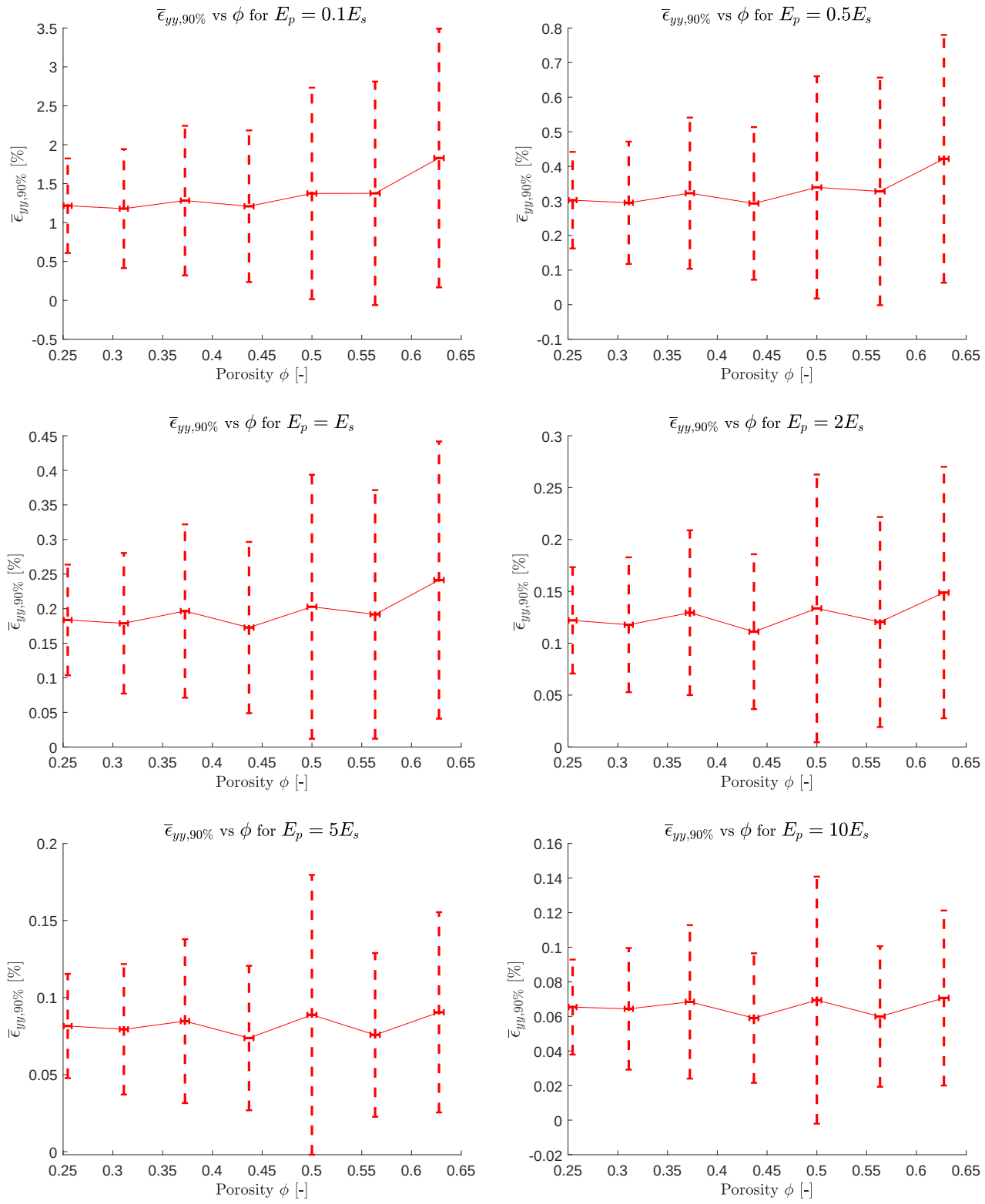

Figure 4.13: Prescribed macroscopic strain at 90% interface damage over porosity for different passivation layer stiffnesses.

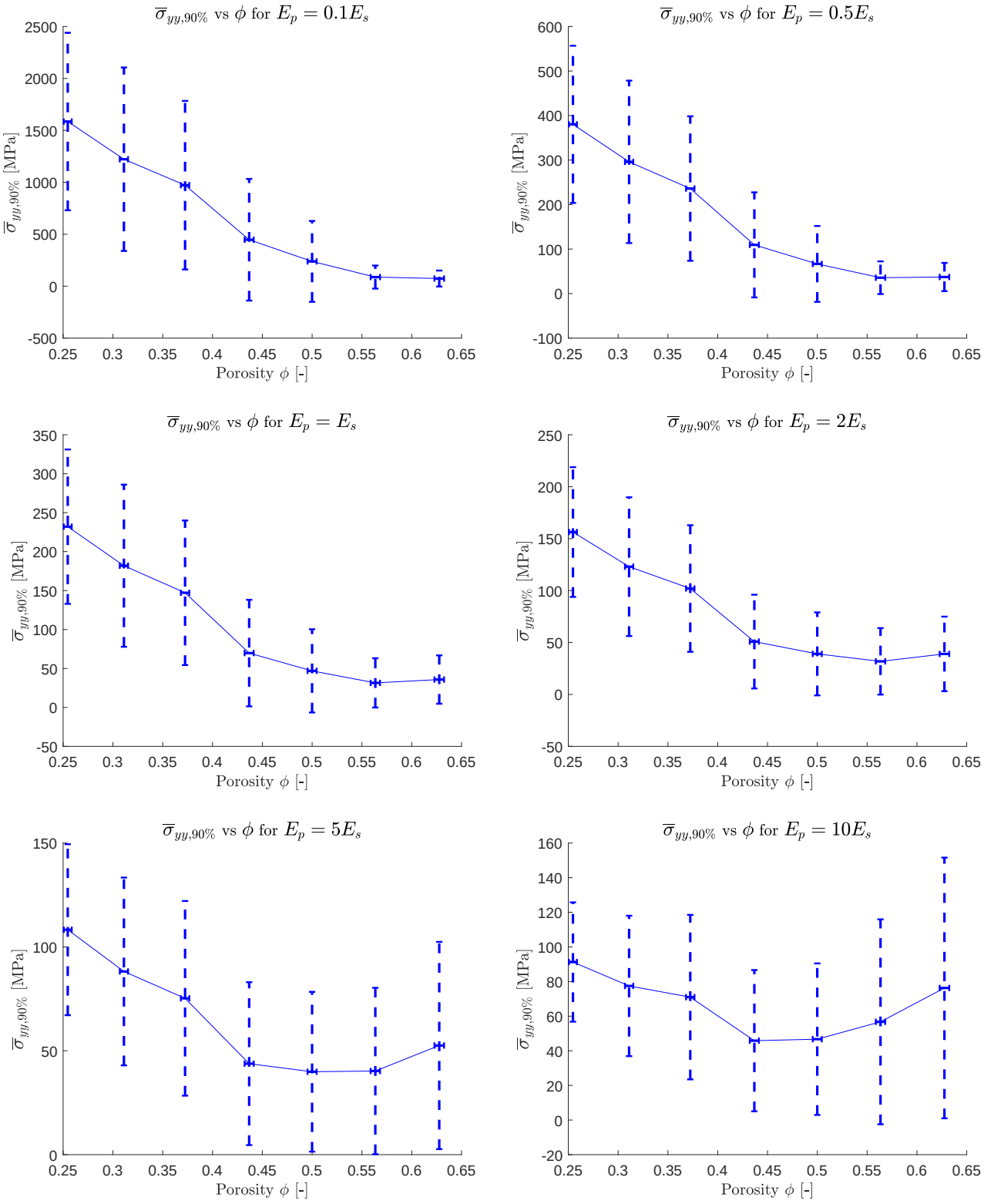

Figure 4.14: Average vertical stress at 90% interface damage over porosity for different passivation layer stiffnesses.

It is observed that the strain is oscillating between peaks and valleys for each stiffness ratio in Figure 4.13. It seems that the strain increases from lowest to highest porosity, especially when the stiffness of the SEI layer is lower than the solid phase's stiffness. However, as the stiffness of the passivation film grows higher the increase in strain is less apparent. This becomes clear when considering the passivation layer stiffness ten times larger than the solid phase's, which strain fluctuates along a fixed horizontal midline. It is concluded that applied strain, related to interface failure, is independent of porosity when the passivation layer stiffness is high. Even for low values of stiffness the strain only increases slightly. It becomes clear that the porosity has little impact on the failure strain for the used material parameters. When evaluating the mean value of strain against the stiffness of the passivation layer, or in this case against different values of k, for different groups of mean porosities $\overline{\phi}$, Figure 4.15 shows that the failure strain decreases exponentially with the passivation layer stiffness. Again, it is observed that the strain is relatively independent of porosity since the strain reaches a fixed level when the stiffness increases. Also, the strain is considered to be within the boundaries of the small strain theory which is seen from the linear behavior of the stress plot after delamination.

The graphs in Figure 4.14 show that the stress decreases with increasing values of porosity when the passivation layer stiffness is lower than that of the solid phase. This may seem obvious, since the strain level remains relatively constant and the increased porosity results in a larger passivation layer domain which reduces the structure's total stiffness. Furthermore, the solid domain's stiffness dominates the overall stress response which must increase for large solid domains, which is the same as a domain with low porosity. When the passivation layer stiffness equates or exceeds the stiffness of the solid domain, the lowest mean stress is shifted to lower porosity values. Clearly, the stiffness of the passivation layer has a major influence on stress response when porosity is high.

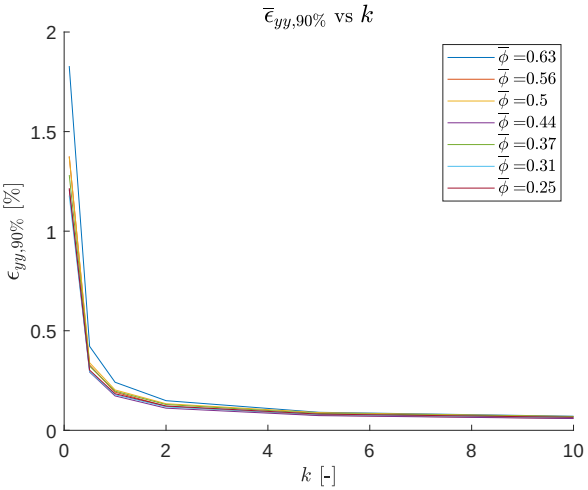

Figure 4.15: Mean value of final strain versus stiffness ratios for different porosity groups.

The stress is plotted over strain for the different porosity groups while varying the stiffness of the passivation layer. Since each porosity group contains different strain values, the data is interpolated and extrapolated to match strain evaluation points. To this purpose, 20 evaluation points are used between zero and an end strain value. This end point is chosen arbitrarily as the maximum applied strain found in an evaluation group. However, some groups include outliers far exceeding a fiber extension of one percent, for these groups the end point is instead chosen as two percent.

Figure 4.16 shows the results for some different porosity groups and stiffnesses. The vertical bars illustrate the standard deviation in stress while the midline is the mean value of stress. For high porosity values, the nonlinearity caused by delamination is clearly visible. However, as the porosity decreases the kink in stress response becomes less distinct. It is obvious, that the stress response is dominated by the solid domain's stiffness for low porosities since the plots indicate a linear stress-strain behavior for the entire load cycle. This is result is further motivated when considering the low standard deviation for the low porosity curves. For the 50% porosity curves, the standard deviation is high. The reason behind this is not completely clear. From this and the results

above, it seems that the mechanical influence of the passivation layer is significant for high porosities and that the layer influences the overall stress considerably.

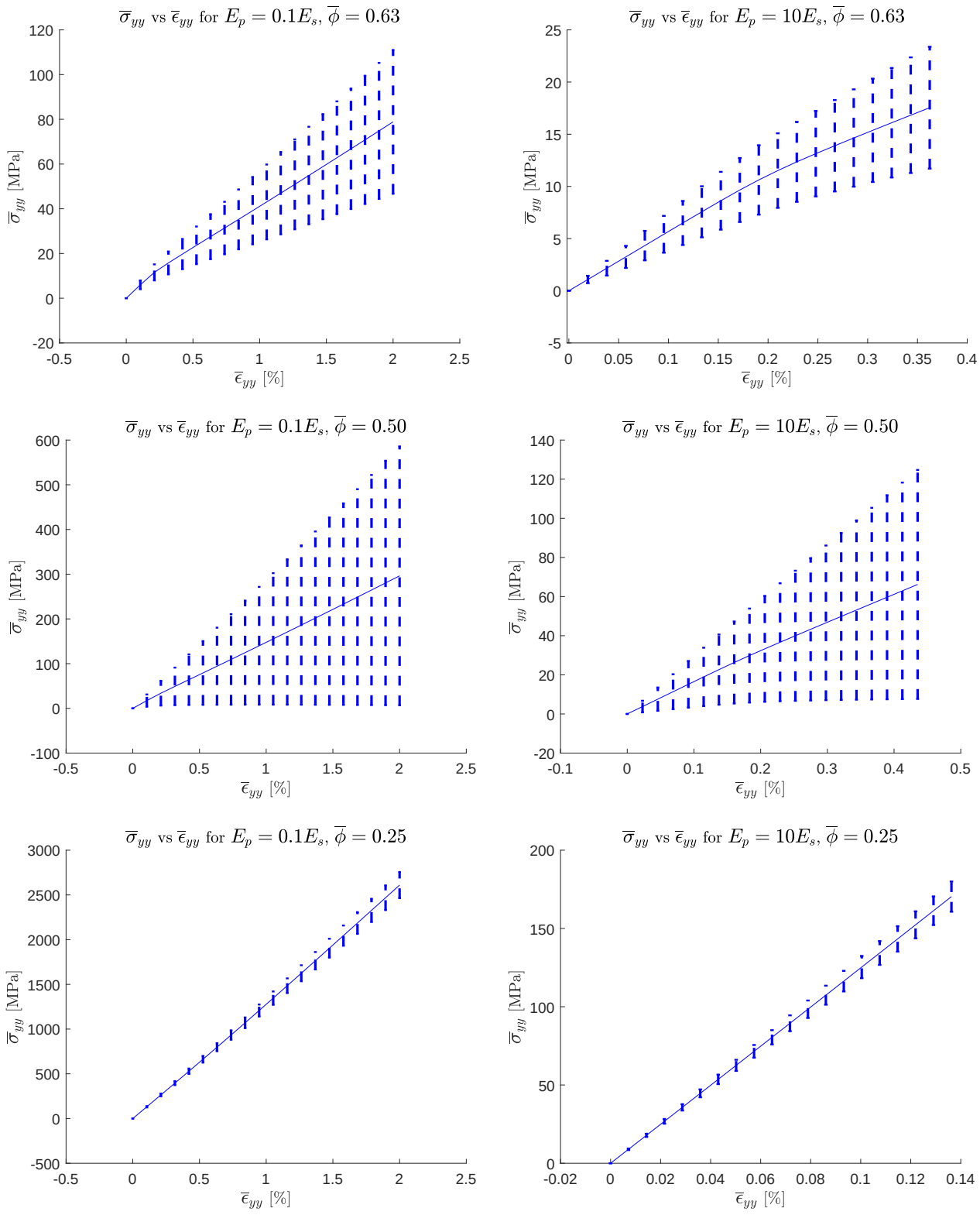

Figure 4.16: Stress over strain for different porosity groups and passivation layer stiffnesses.

One stiffness ratio is considered for the 3D sample in Figure 3.23 for the material parameters in Table 3.1. The considered sample has a porosity around 70%, implying that the passivation layer should impact the stress response when taking into account the results from 2D. The passivation layer stiffness was arbitrarily chosen as half of the solid's stiffness. It should be noted that the strain is not applied until 90% of the interface is separated but rather 80%. The `COMSOL` solver did not manage to find a solution for higher values of interface damage for the considered sample. Figure 4.17 shows the area averaged stress and damage evolution of the 3D structure. Just like for the 2D case, a kink is observed at the beginning of delamination. The damage response is exponential at first but becomes logarithmic when a large portion of the interface is damaged.

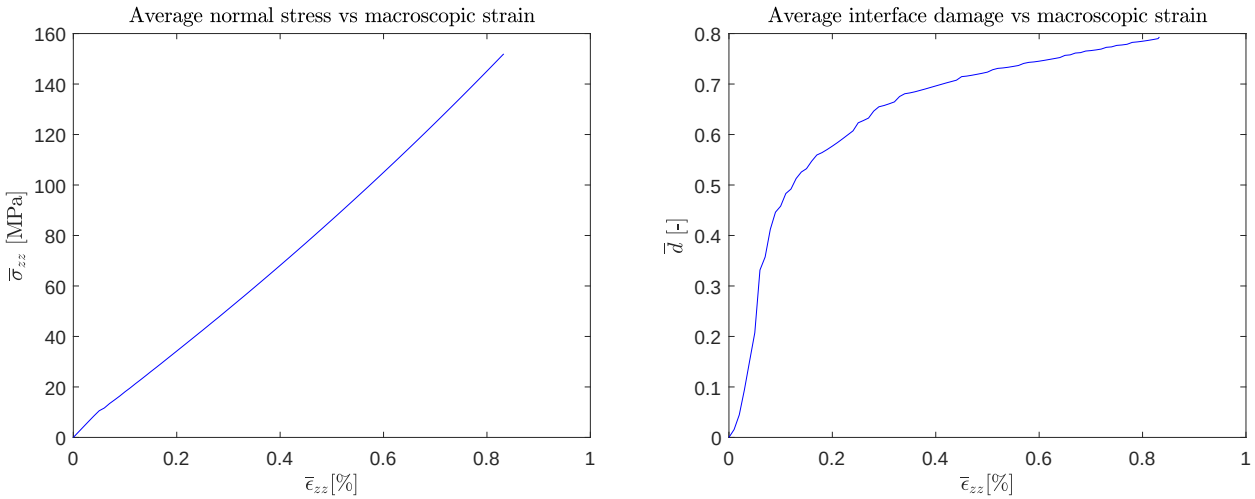

(a) Volume averaged stress over macroscopic strain. **(b)** Average interface damages over macroscopic strain.

Figure 4.17: Stress and damage response 3D SVE with passivation layer.

5 Concluding remarks

Through the use of external libraries, MATLAB scripts, Python scripts, and the MATLAB API in COMSOL, the process of generating and analyzing synthetic microstructures was successfully implemented as a fully automatic procedure.

This thesis project has investigated four distinct types of techniques for generating synthetic structural battery electrolyte microstructures. Their effective macroscopic properties pertaining to mechanical strength and ion conductivity were evaluated through use of computational homogenization. Two additional topics were investigated: a synthetic structural battery positive electrode microstructure, and the interaction between the carbon fiber and the electrolyte at their interface in respect to the passivation layer. For this purpose a fully automated framework has been developed in which 2D electrolyte microstructures are generated for suitable input parameters and imported to COMSOL for homogenization through the finite element method. The evaluation of the effective properties of the electrolyte reveal that the topology of the microstructure has a significant effect on the macroscopic performance. In the case of diffusivity the porosity is the most significant factor, but the specific type of structure has a degree of influence. In the case of stiffness it is found that for any structure the relation between effective stiffness and porosity is approximately linear, but the influence of the type of structure has a major effect. In regards to bifunctional performance the Cahn-Hilliard and Voronoi structures seem to be optimal, which is likely a result of their two phases having a similar morphology. When comparing the results to that of previous research, it was found that for the structures which were comparable, the results were similar. This is a major result as it proves the validity of the methodology of both studies since they were conducted independent of each other and no code or files were shared. The convex hull structures presented in this project manage to emulate some of the experimental values better than the structures presented in the cited paper, indicating their potential usefulness.

This project developed a novel microstructure based on convex hulls. The development of this structure is considered a major result due to both its ability to emulate the previously mentioned experimental values and its low computational level, meaning that it is easy for the user to make changes at the fundamental steps in the routine. The two physics based microstructures suffer from the disadvantage that the morphology is dependent on the equations and cannot be conveniently modified or tuned. Similarly, the sphere packing structure are also difficult to customize much other than changing the dispersity parameters. The convex hull structures as presented here do rely on a Voronoi tessellation and a sphere packing to form the basis. But the end result can be modified quite heavily since the entire process is written in MATLAB code, in addition to its large number of generation parameters. It was observed that the convex hulls had much lower effective stiffness than the other structures. Analysis of the connectivity of the structures reveal that each convex hull had on average 2.5 connections as a result of the chosen network algorithm. By changing this algorithm a higher connectivity can be achieved. Raising the connectivity however will indirectly lead to higher volume fractions as a result of the connections. This is difficult to control with just the cell scaling method. A supplemental method to control the structure's volume and morphology is to implement pore cells, which do not contain a convex hull and are excluded from the connectivity network. This method was successfully implemented, but only briefly examined, and not used in the project. Despite the addition of pores seeming like an intuitive method to control the output structure volume, it was instead found to be very difficult to characterize the influence of these pore cells on the volume. Ultimately, examining the uses of this generation technique could be worthwhile for further work.

The ease of modification of the convex hull structures was demonstrated with the ability to redefine some of the connections as binders which enabled the generation of a synthetic electrode microstructure. Simulation and homogenization of the binder structures seemed to indicate that the effective stiffness is primarily dependent on the binder stiffness, but that the volume fraction of the binder did not seem to have much of an influence. However, it was recognized that a more extensive parametric study would be necessary to draw more confident conclusions.

It was shown that the passivation layer may have significant influence on the stress response depending on the used modeling parameters of the microstructure for the generated 2D samples. It was also observed that the failure strain is relatively independent of porosity but highly dependent on the passivation layer stiffness. However, the parameters were chosen arbitrarily and no test data was available for comparison, so the results

have to be confirmed against actual experiments before final conclusions can be made. Investigating passivation layer parameters and considering different loading conditions like radial expansion becomes of interest. But since the toolbox is fully automated, and changing settings is trivial, the passivation layer toolbox acts as a solid basis for future work. A single 3D passivation layer sample was implemented manually as a proof of concept. Finding solver settings and step sizes for the strain control proved to be problematic for the 3D case. These were tuned manually and a method to enable automation still needs to be identified for the 3D case. However, due to the computational cost of the model it might be challenging to feasibly automate this process.

One of the greatest challenges with this work was the practical implementation of the automation between structure generation, structure import, and structure meshing. Different realizations required different settings to work, but since automation was a requirement it was not feasible to manually adjust the settings each time. A lot of work went into finding settings that resulted in acceptable success rates at around 20%-40%. For the sphere and convex hull structures the methodological choice to generate STEP files was obvious due to its relative simplicity and the versatile advantages of a CAD format. The strategy used for the field solution based Cahn-Hilliard and Voronoi structures took a long time to develop. `COMSOL` offers many options for exporting a solution, but none of them perfectly matched the desired purpose. Ultimately the most consistent method was to export the solution mesh and rebuild the it as shells in a `FreeCAD Python script` which could then be converted into a solid. As a product of this method, the structure's resolution is dependent on the mesh resolution in the original solution. Attempting to use smoothening operations to get a nicer looking structure turned out to be very problematic and would often interfere with the strict periodicity of the SPBCs.

Bibliography

[1] Leif E. Asp and Emile S. Greenhalgh. "Structural power composites". In: *Composites Science and Technology* 101 (2014), pp. 41–61. ISSN: 0266-3538. DOI: https://doi.org/10.1016/j.compscitech.2014.06.020. URL: http://www.sciencedirect.com/science/article/pii/S0266353814002218.

[2] Giulia Fredi et al. "Graphitic microstructure and performance of carbon fibre Li-ion structural battery electrodes". In: *Multifunctional Materials* 1.1 (Sept. 2018), p. 015003. DOI: 10.1088/2399-7532/aab707. URL: https://doi.org/10.1088%2F2399-7532%2Faab707.

[3] Leif Asp et al. "Structural Battery Composites: A Review". In: *Functional Composites and Structures* (Nov. 2019). DOI: 10.1088/2631-6331/ab5571.

[4] David Carlstedt. "On the multifunctional performance of structural batteries". PhD thesis. Chalmers University of Technology, 2019.

[5] N. Ihrner et al. "Structural lithium ion battery electrolytes via reaction induced phase-separation". In: *J. Mater. Chem. A* 5 (48 2017), pp. 25652–25659. DOI: 10.1039/C7TA04684G. URL: http://dx.doi.org/10.1039/C7TA04684G.

[6] Jurica Sorić, Peter Wriggers, and O. Allix. *Multiscale Modeling of Heterogeneous Structures*. Jan. 2018. ISBN: 978-3-319-65462-1. DOI: 10.1007/978-3-319-65463-8.

[7] Ming Huang and Yue-ming Li. "X-ray tomography image-based reconstruction of microstructural finite element mesh models for heterogeneous materials". In: *Computational Materials Science* 67 (2013), pp. 63–72. ISSN: 0927-0256. DOI: https://doi.org/10.1016/j.commatsci.2012.08.032. URL: http://www.sciencedirect.com/science/article/pii/S0927025612005241.

[8] Jochen Joos et al. "Reconstruction of porous electrodes by FIB/SEM for detailed microstructure modeling". In: *Journal of Power Sources* 196.17 (2011). Proceedings of 2010 European Solid Oxide Fuel Cell Forum, pp. 7302–7307. ISSN: 0378-7753. DOI: https://doi.org/10.1016/j.jpowsour.2010.10.006. URL: http://www.sciencedirect.com/science/article/pii/S0378775310017337.

[9] Marc Geers et al. "Computational homogenization of structures and materials". In: *Modelling and Simulation in Materials Science and Engineering - MODEL SIMUL MATER SCI ENG* (Jan. 2009).

[10] Ralf Jänicke, Fredrik Larsson, and Kenneth Runesson. *Computational Homogenization in Material Mechanics*. Gothenburg, May 2020.

[11] Katherine A. Acton and Sarah C. Baxter. "Characterization of Random Composite Properties Based on Statistical Volume Element Partitioning". In: *Journal of Engineering Mechanics* 144.2 (2018), p. 04017168. DOI: 10.1061/(ASCE)EM.1943-7889.0001396.

[12] Ralf Jänicke, Fredrik Larsson, and Kenneth Runesson. *The Finite Element Method – Solid Mechanics*. Gothenburg, Dec. 2018.

[13] Niels Saabye Ottosen and Hans Petersson. *Introduction to the Finite Element Method*. eng. Prentice-Hall, 1992. ISBN: 0-13-473877-2.

[14] D. Carolan et al. "Co-continuous polymer systems: A numerical investigation". In: *Computational Materials Science* 98 (2015), pp. 24–33. ISSN: 0927-0256. DOI: https://doi.org/10.1016/j.commatsci.2014.10.039. URL: http://www.sciencedirect.com/science/article/pii/S0927025614007137.

[15] Long-Qing Chen. "Phase-Field Models for Microstructure Evolution". In: *Annual Review of Materials Research* 32.1 (2002), pp. 113–140. DOI: 10.1146/annurev.matsci.32.112001.132041. eprint: https://doi.org/10.1146/annurev.matsci.32.112001.132041. URL: https://doi.org/10.1146/annurev.matsci.32.112001.132041.

[16] Boris D. Lubachevsky and Frank H. Stillinger. "Geometric Properties of Random Disk Packing". In: *Journal of Statistical Physics* 60.5/6 (Mar. 1990), pp. 561–583.

[17] Monica Skoge et al. "Packing hyperspheres in high-dimensional Euclidean spaces". In: *Physical Review E* 74.4 (Oct. 2006). ISSN: 1550-2376. DOI: 10.1103/physreve.74.041127. URL: http://dx.doi.org/10.1103/PhysRevE.74.041127.

[18] Franz Aurenhammer. "Voronoi Diagrams—a Survey of a Fundamental Geometric Data Structure". In: *ACM Comput. Surv.* 23.3 (Sept. 1991), pp. 345–405. ISSN: 0360-0300. DOI: 10.1145/116873.116880. URL: https://doi.org/10.1145/116873.116880.

[19] Felix Fritzen, Thomas Böhlke, and Eckart Schnack. "Periodic three-dimensional mesh generation for crystalline aggregates based on Voronoi tessellations". In: *Computational Mechanics* 43 (Apr. 2009), pp. 701–713. DOI: 10.1007/s00466-008-0339-2.

[20] Vinh Tu. "Modeling and finite element simulation of the bifunctional performance of a microporous structural battery electrolyte". MA thesis. Chalmers University of Technology, 2019.

[21] Nele Pollman. "Multi-scale modeling and finite element simulation of diffusion in porous media". PhD thesis. Chalmers University of Technology, 2019, p. 23. ISBN: 978-91-7905-170-9.

[22] Chris H. Rycroft. "VORO++: A three-dimensional Voronoi cell library in C++". In: *Chaos: An Interdisciplinary Journal of Nonlinear Science* 19.4 (2009), p. 041111. DOI: 10.1063/1.3215722. eprint: https://doi.org/10.1063/1.3215722. URL: https://doi.org/10.1063/1.3215722.

[23] Mark de Berg et al. *Computational Geometry: Algorithms and Applications*. 3rd ed. Santa Clara, CA, USA: Springer-Verlag TELOS, 2008. ISBN: 3540779736.

[24] Daniel Westhoff, Ingo Manke, and Volker Schmidt. "Generation of virtual lithium-ion battery electrode microstructures based on spatial stochastic modeling". In: *Computational Materials Science* 151 (2018), pp. 53–64. ISSN: 0927-0256. DOI: https://doi.org/10.1016/j.commatsci.2018.04.060. URL: http://www.sciencedirect.com/science/article/pii/S092702561830301X.

[25] John D'Errico. *Inhull (MATLAB Central File Exchange)*. [Online; accessed March-2020]. 2020. URL: https://www.mathworks.com/matlabcentral/fileexchange/10226-inhull.

[26] R. C. Prim. "Shortest connection networks and some generalizations". In: *The Bell System Technical Journal* 36.6 (1957), pp. 1389–1401.

[27] Johan Hagberg et al. "Lithium iron phosphate coated carbon fiber electrodes for structural lithium ion batteries". In: *Composites Science and Technology* 162 (2018), pp. 235–243. ISSN: 0266-3538. DOI: https://doi.org/10.1016/j.compscitech.2018.04.041. URL: http://www.sciencedirect.com/science/article/pii/S0266353818302082.

[28] Eric Jacques. "Lithium-intercalated Carbon Fibres : Towards the Realisation of Multifunctional Composite Energy Storage Materials". QC 20140423. PhD thesis. KTH, Lightweight Structures, 2014, pp. xi, 61. ISBN: 978-91-7595-072-3.

[29] COMSOL Multiphysics 5.5 ©. *Structural Mechanics Module - User's Guide*. 2019. Chap. Structural Mechanics Theory - Contact Analysis Theory.

[30] Jacob Lubliner and Panayiotis Papadopoulos. *Introduction to Solid Mechanics*. Jan. 2017. DOI: 10.1007/978-3-319-18878-2.

[31] Vinh Tu et al. "Performance of Bicontinuous Structural Electrolytes". In: *Multifunctional Materials* (2020). URL: http://iopscience.iop.org/10.1088/2399-7532/ab8d9b.

[32] Luize Scalco de Vasconcelos et al. "Grid indentation analysis of mechanical properties of composite electrodes in Li-ion batteries". In: *Extreme Mechanics Letters* 9 (2016). Mechanics of Energy Materials, pp. 495–502. ISSN: 2352-4316. DOI: https://doi.org/10.1016/j.eml.2016.03.002. URL: http://www.sciencedirect.com/science/article/pii/S2352431616300190.

A Examples of synthetic microstructures

Cahn-Hilliard

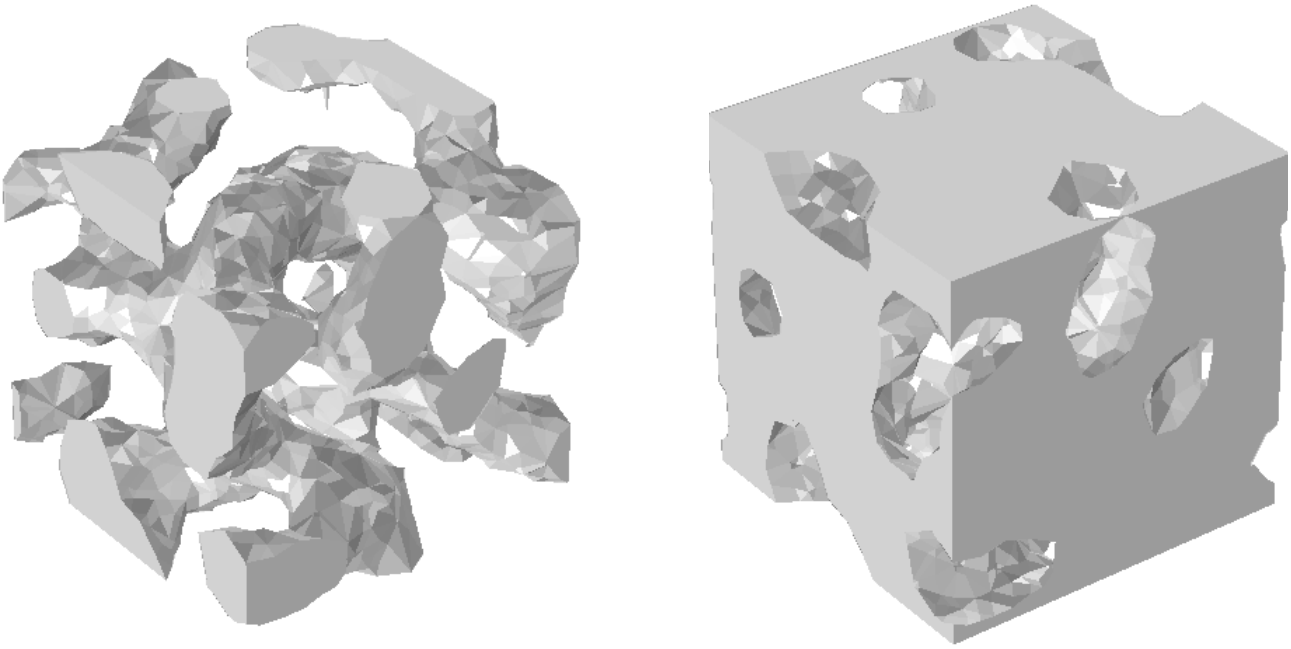

(a) Solid phase.

(b) Inverted phase.

Figure A.1: 30% solid volume fraction.

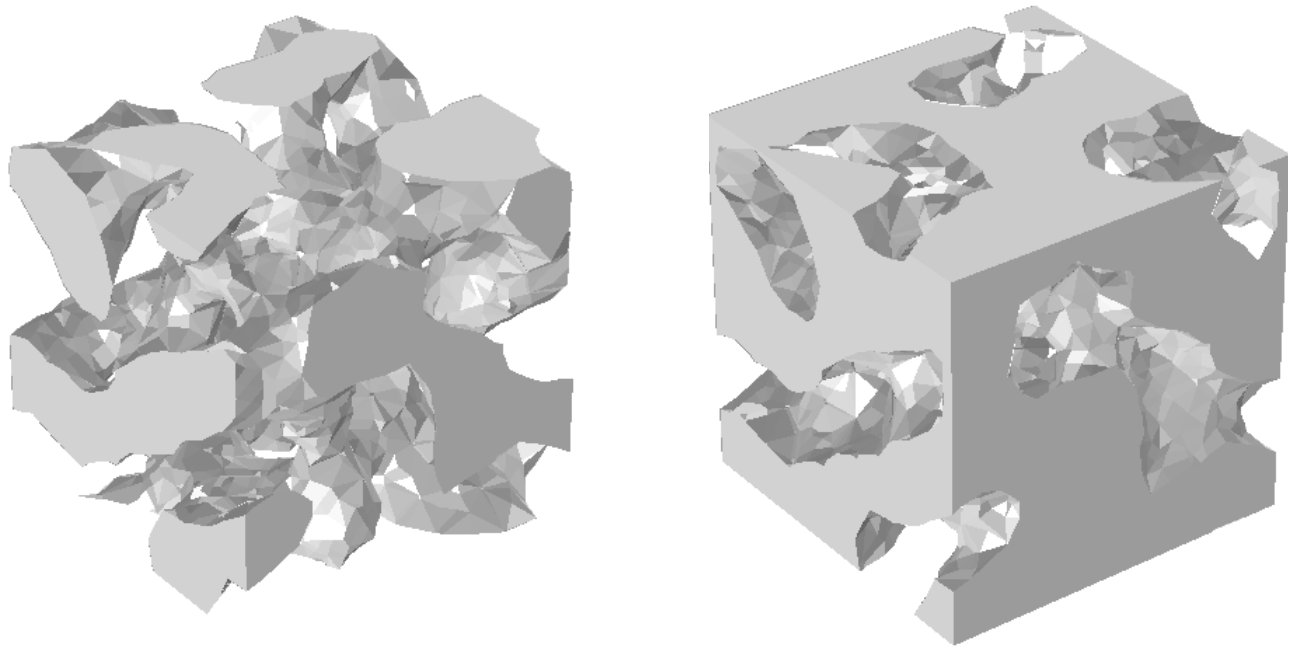

(a) Solid phase.

(b) Inverted phase.

Figure A.2: 40% solid volume fraction.

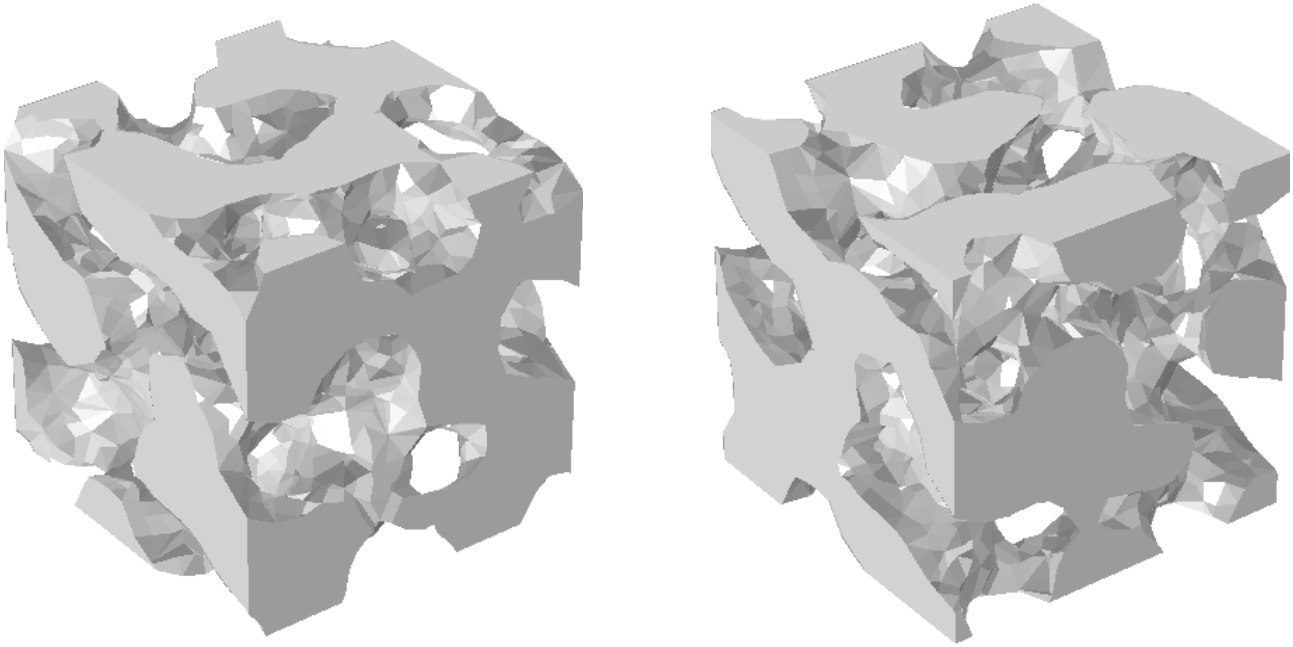

(a) Solid phase.

(b) Inverted phase.

Figure A.3: 50% solid volume fraction.

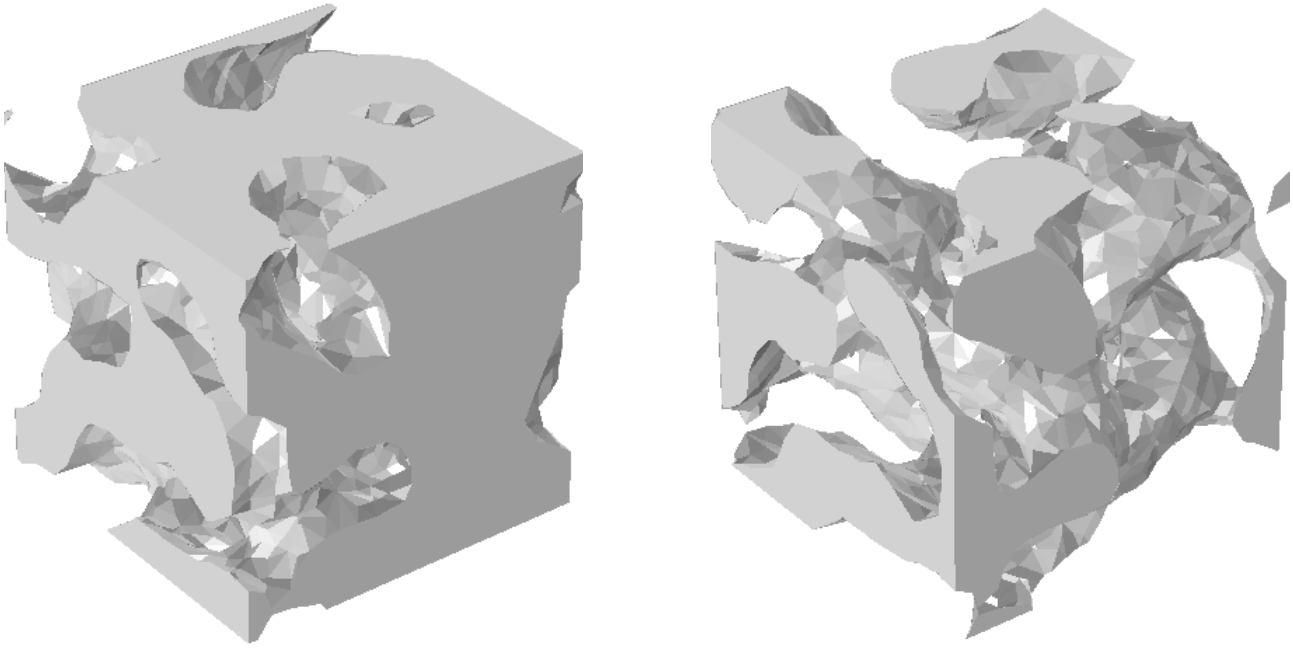

(a) Solid phase.

(b) Inverted phase.

Figure A.4: 60% solid volume fraction.

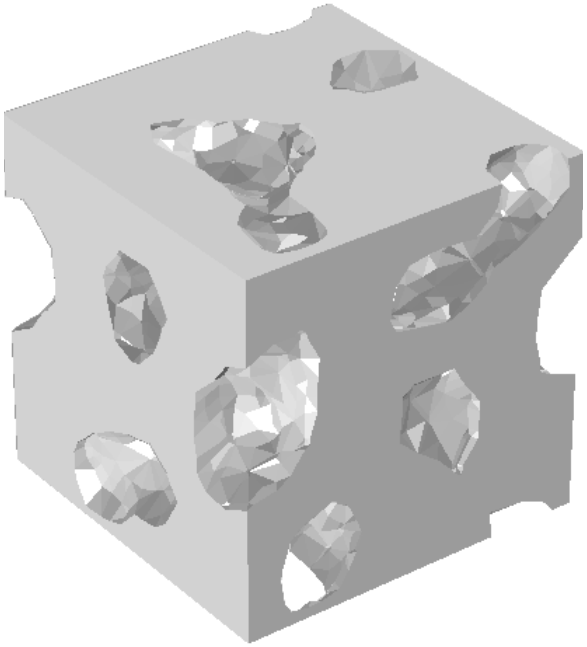

(a) Solid phase.

(b) Inverted phase.

Figure A.5: 70% solid volume fraction.

Voronoi

(a) Solid phase.

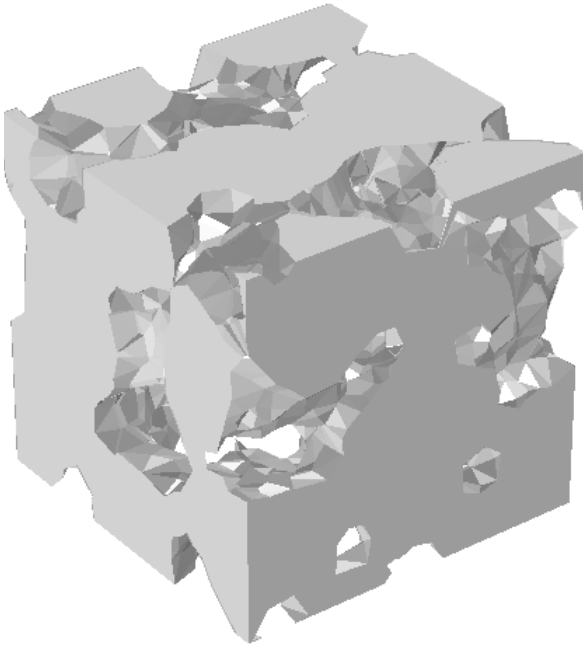

(b) Inverted phase.

Figure A.6: 30% solid volume fraction.

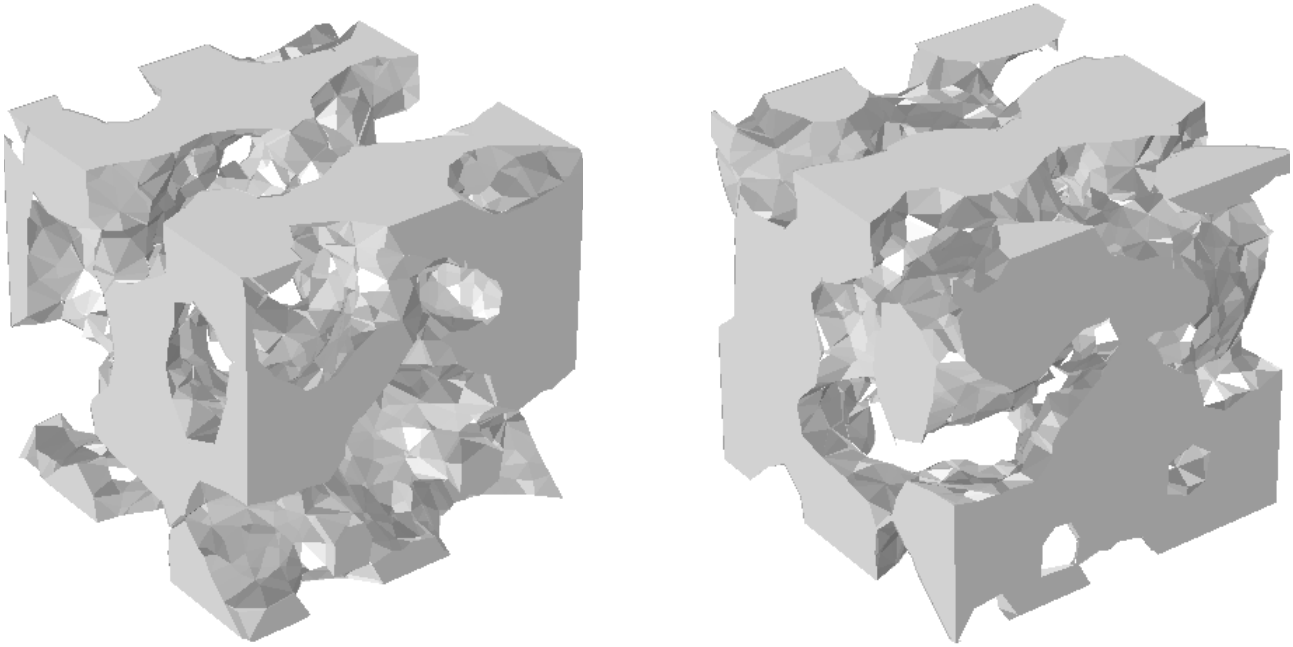

(a) Solid phase.

(b) Inverted phase.

Figure A.7: 40% solid volume fraction.

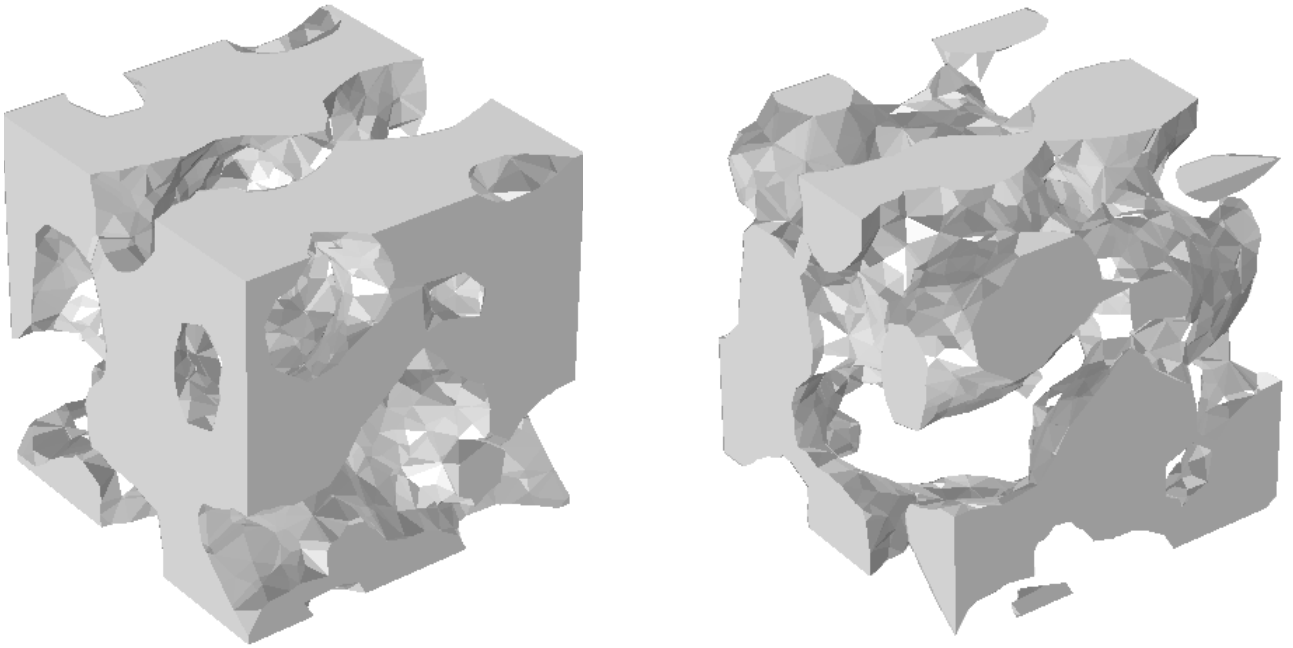

(a) Solid phase.

(b) Inverted phase.

Figure A.8: 50% solid volume fraction.

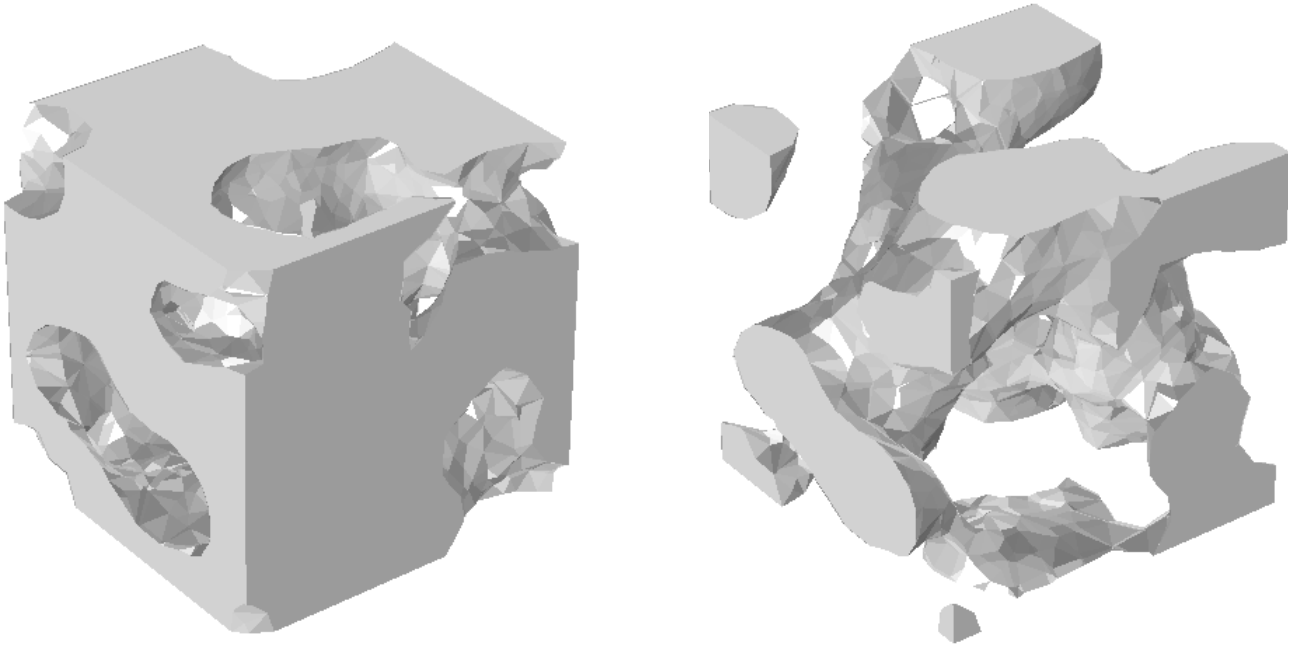

(a) Solid phase.

(b) Inverted phase.

Figure A.9: 60% solid volume fraction.

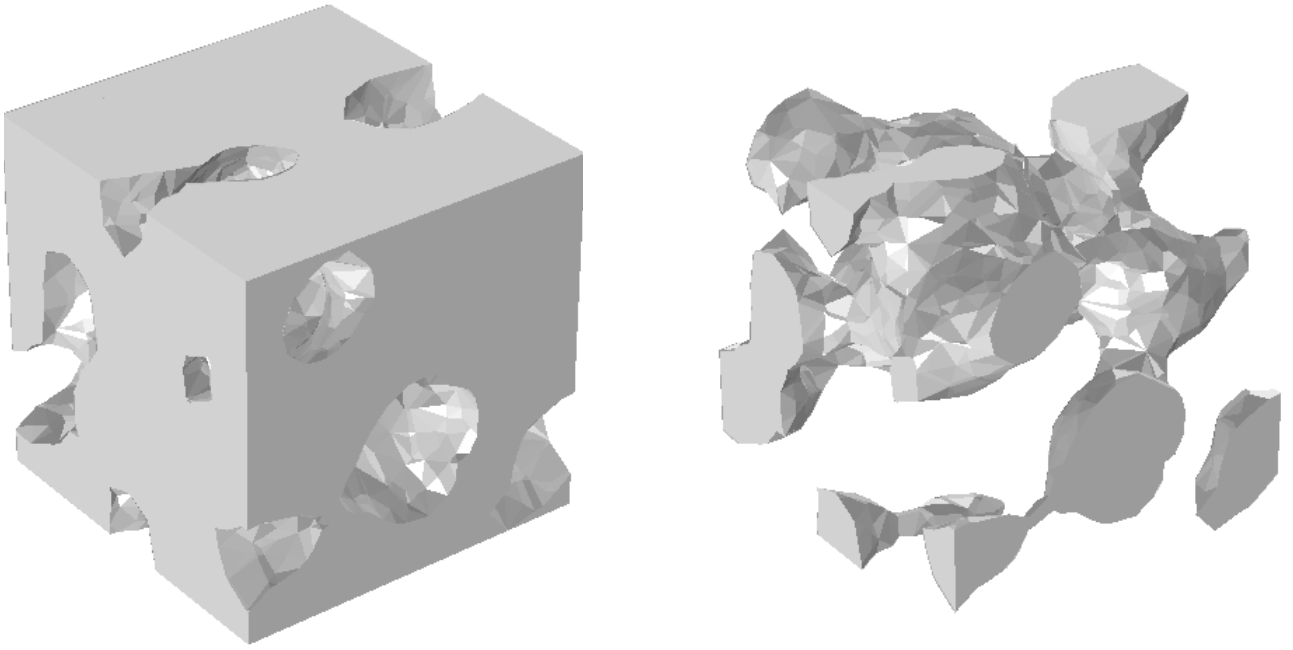

(a) Solid phase.

(b) Inverted phase.

Figure A.10: 70% solid volume fraction.

Spheres

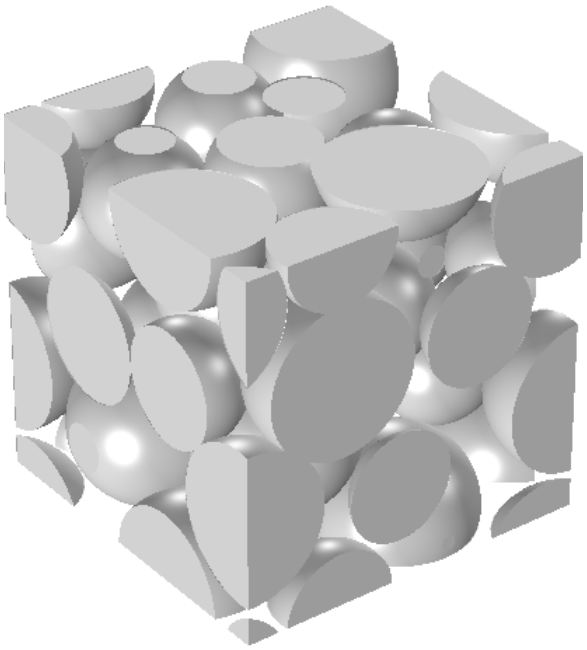

(a) Solid phase.

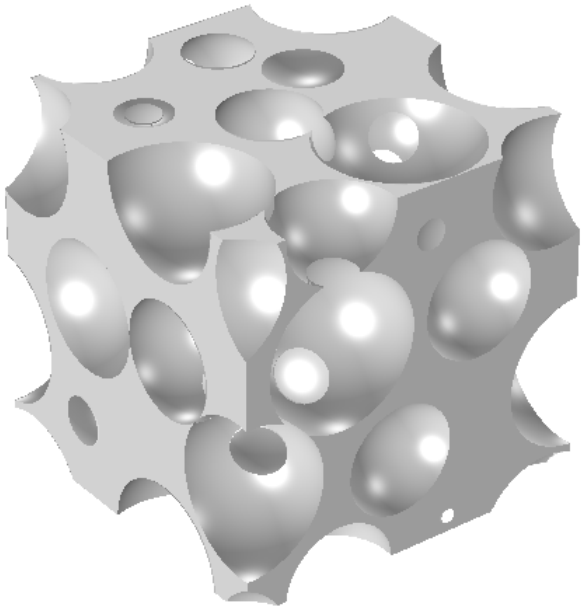

(b) Inverted phase.

Figure A.11: 60% solid volume fraction.

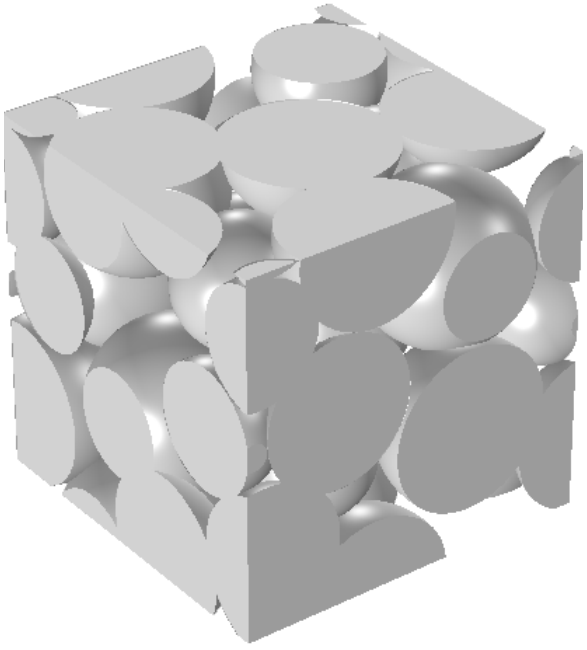

(a) Solid phase.

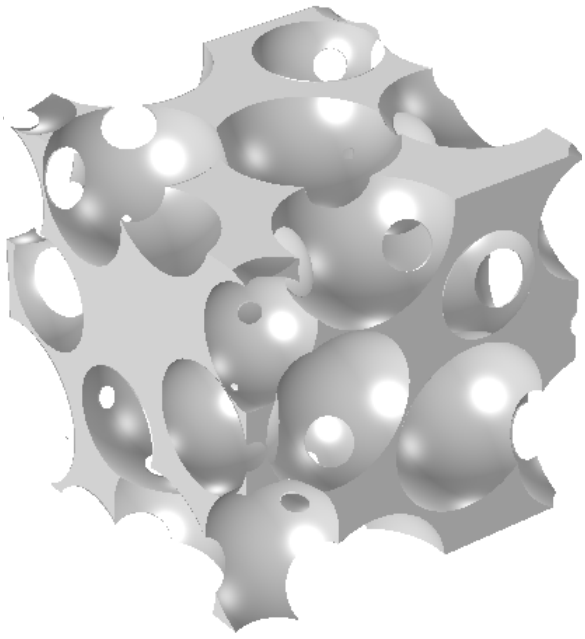

(b) Inverted phase.

Figure A.12: 70% solid volume fraction.

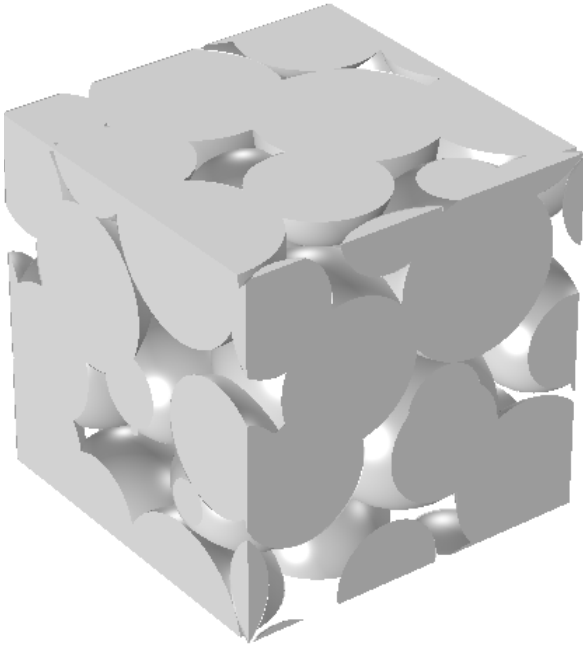

(a) Solid phase.

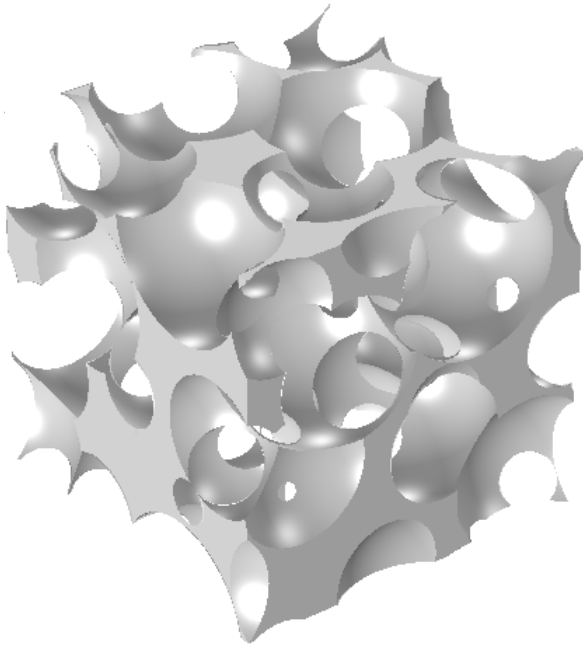

(b) Inverted phase.

Figure A.13: 80% solid volume fraction.

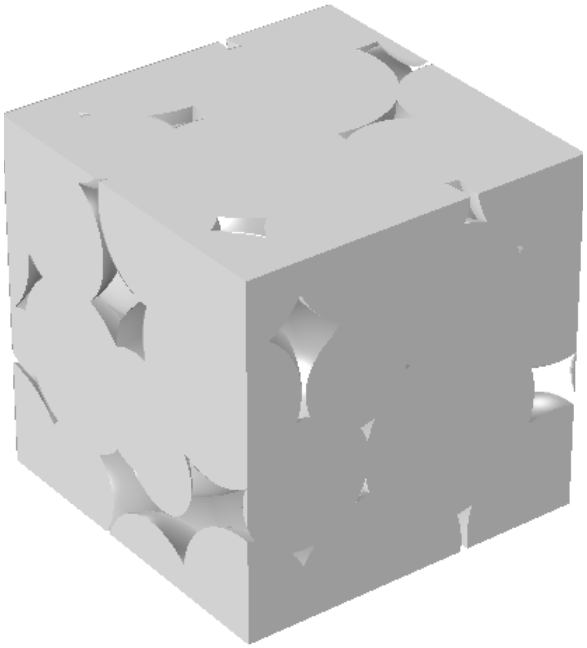

(a) Solid phase.

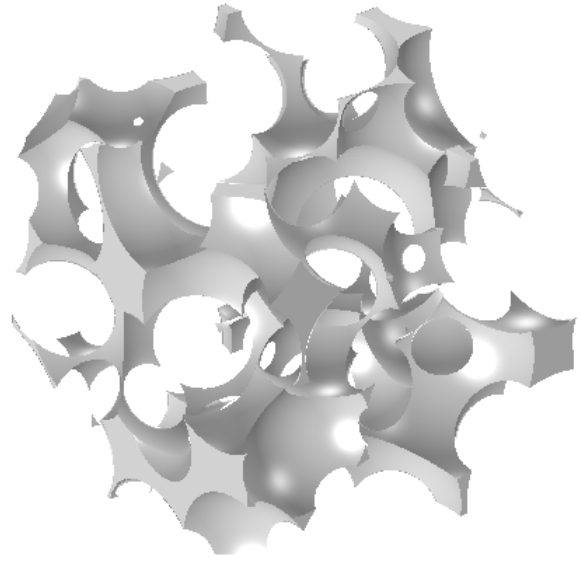

(b) Inverted phase.

Figure A.14: 90% solid volume fraction.

Convex hulls

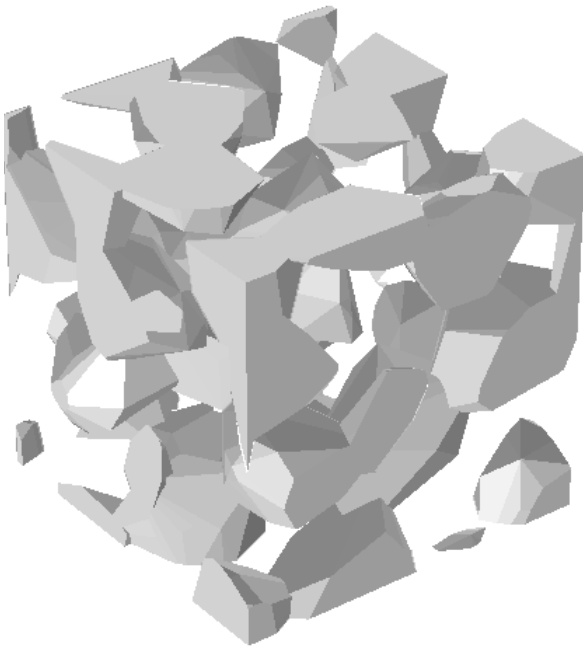

(a) Solid phase.

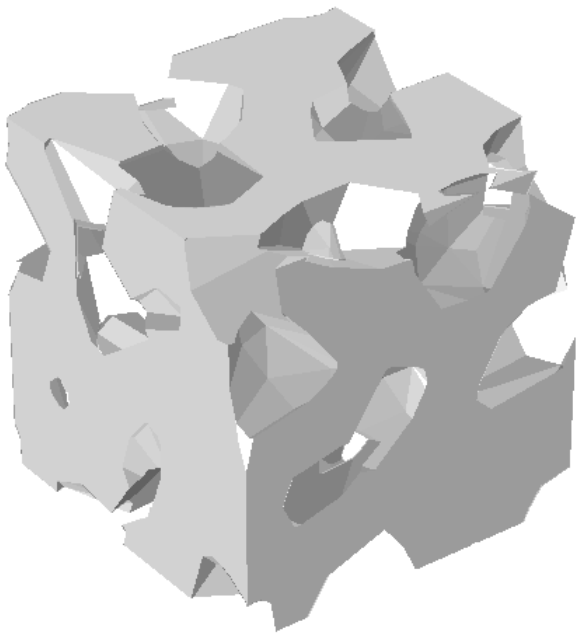

(b) Inverted phase.

Figure A.15: 30% solid volume fraction.

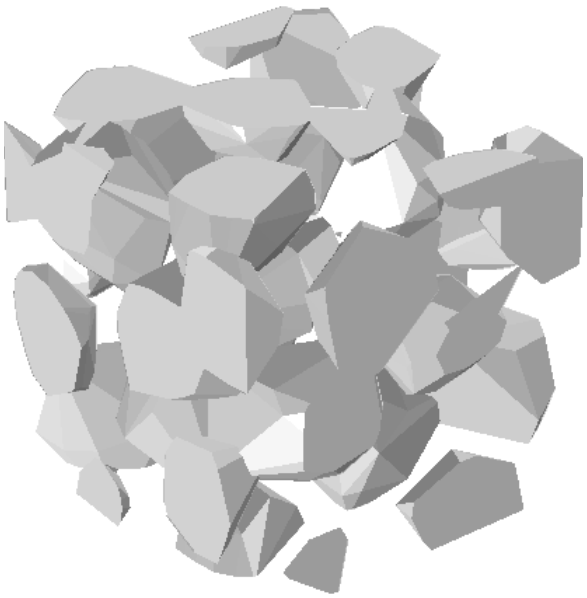

(a) Solid phase.

(b) Inverted phase.

Figure A.16: 40% solid volume fraction.

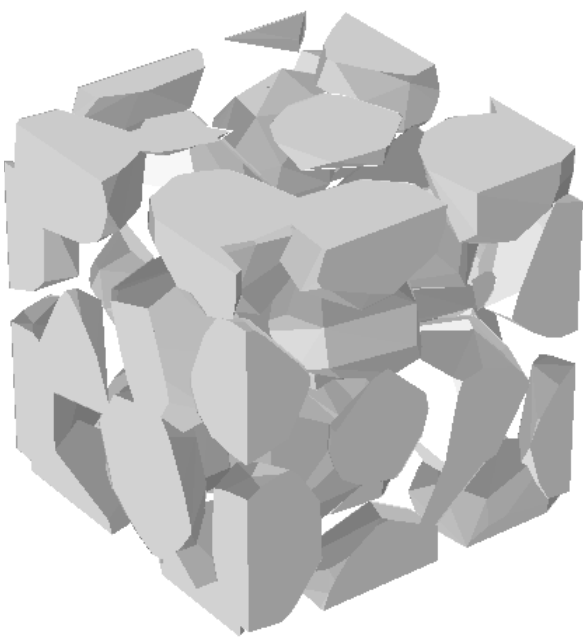

(a) Solid phase.

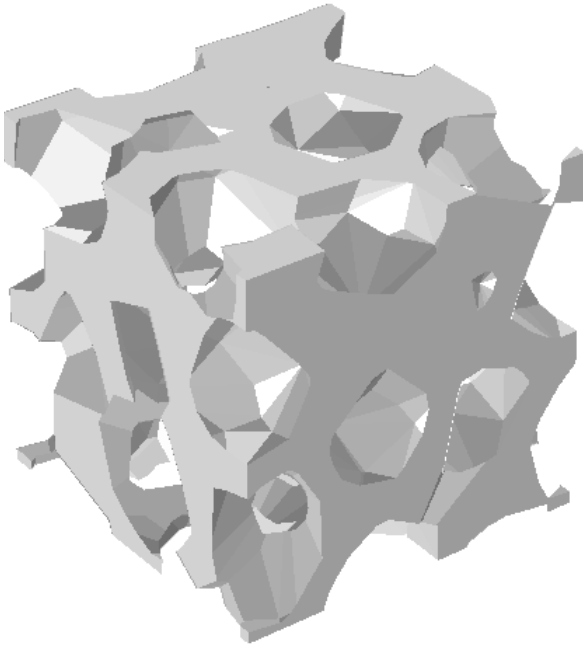

(b) Inverted phase.

Figure A.17: 50% solid volume fraction.

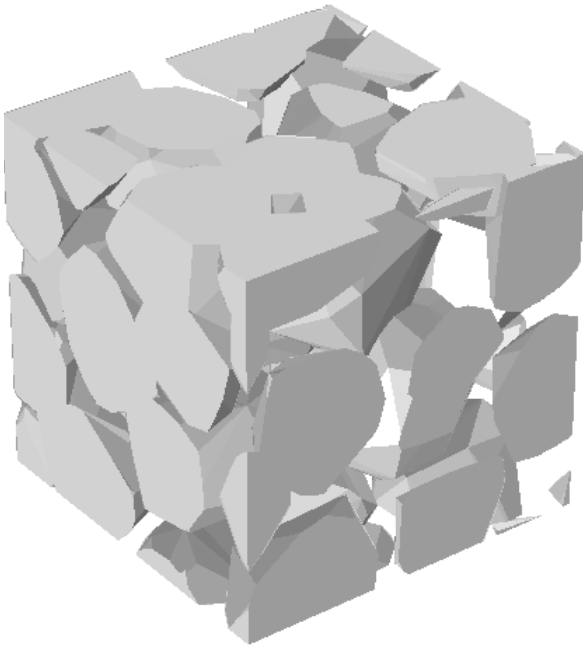

(a) Solid phase.

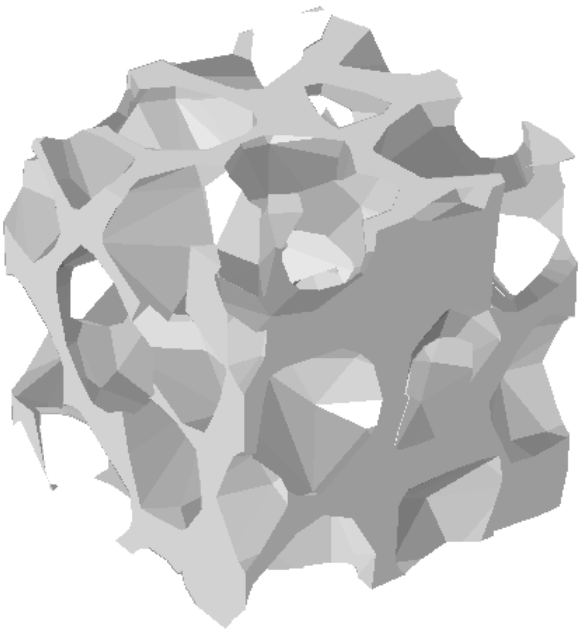

(b) Inverted phase.

Figure A.18: 60% solid volume fraction.

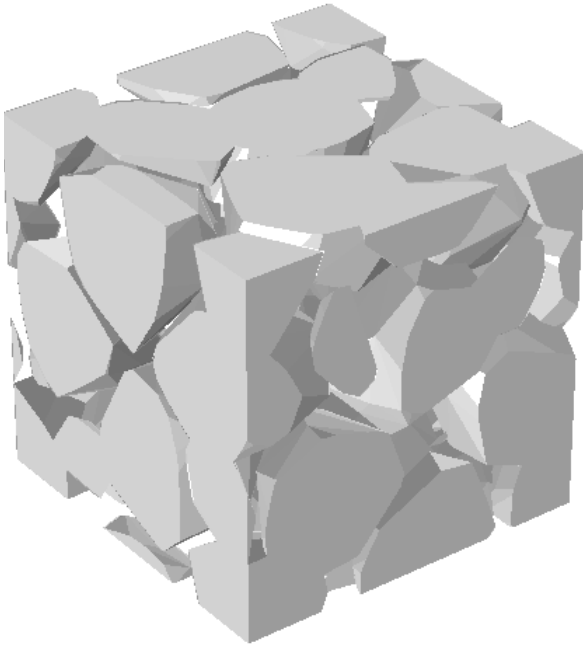

(a) Solid phase.

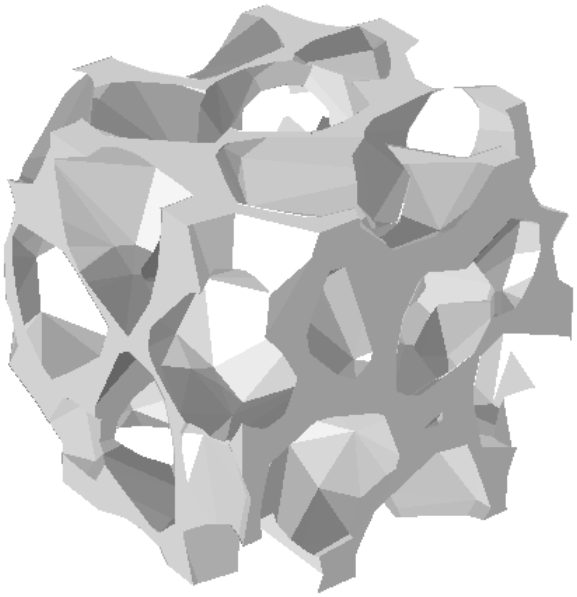

(b) Inverted phase.

Figure A.19: 70% solid volume fraction.